2018-07-17

Development of Turn-On Fluorescent Kinase Inhibitors

Heajin Lee
University of Miami, h.lee.chemistry@gmail.com

UNIVERSITY OF MIAMI

DEVELOPMENT OF TURN-ON FLUORESCENT KINASE INHIBITORS

By

Heajin Lee

A DISSERTATION

Submitted to the Faculty
of the University of Miami
in partial fulfillment of the requirements for
the degree of Doctor of Philosophy

Coral Gables, Florida

August 2018

UNIVERSITY OF MIAMI

A dissertation submitted in partial fulfillment of
the requirements for the degree of
Doctor of Philosophy

DEVELOPMENT OF TURN-ON FLUORESCENT KINASE INHIBITORS

Heajin Lee

Approved:

_____ James Wilson, Ph.D. Associate Professor of Chemistry	_____ Francisco Raymo, Ph.D. Professor of Chemistry
_____ Rajeev Prabhakar, Ph.D. Professor of Chemistry	_____ Guillermo Prado, Ph.D. Dean of the Graduate School
_____ James Baker, Ph.D. Professor of Biology	

LEE, HEAJIN (Ph.D., Chemistry)
Development of Turn-On Fluorescent Kinase Inhibitors. (August 2018)

Abstract of a dissertation at the University of Miami.

Dissertation supervised by Professor James Wilson.
No. of pages in text. (120)

The EGFR/ERBB family of tyrosine kinase receptors (ERBB1-4) are involved in regulation of intracellular communications such as cell proliferation, metabolism, and numerous biological responses. The dysregulation of their signaling pathways contributes to development of cancer malignancies. This receptor family is a conventional chemotherapeutic target and serves as diagnostic modality. ERBB2, also known as HER2, is a prognostic biomarker implicated in about 20 % of invasive breast cancer incidence. Hence, the status of ERBB2 is a crucial factor in deciding treatment type for breast cancer patients.

Common immunohistochemistry assays analyzing the ERBB2 receptor tyrosine kinase rely on use of antibodies. These assays often require multi-step specimen preparation such as cell fixation or cell lysis, resulting in observation of a biologically stopped system. In this context, we aimed to develop small molecular fluorescent probes for ERBB2 to explore the dynamic information related to the signaling activation at the live single cell level.

Hence, we generated turn-on fluorescent kinase inhibitors targeting the ATP binding pocket of the ERBB2 by structurally modifying clinically relevant EGFR/ERBB inhibitors. The fluorescent kinase inhibitors are capable of acquiring dynamic information in live cell with minimized specimen preparation comparing to immunohistochemistry assays.

The turn-on fluorescent kinase inhibitors that we have developed are capable of identifying the ERBB2 (+) breast cancer cells from ERBB2 (-) cells as well as tracking rapid responses to perturbation factors at the level of individual breast cancer cells including ERBB2 activation and internalization. Our live cell compatible kinase probes serve as a novel analytic tool providing complimentary information to immunohistochemical analysis in ERBB2 (+) breast cancer biology.

ACKNOWLEDGEMENT

I would like to thank Dr. James Wilson for providing me the opportunity to construct my graduate research with multidisciplinary characteristics. I genuinely appreciate his guidance and advice throughout my graduate education at the University of Miami. I would like to express my respect to his excellence and brilliance as a scientist and educator. I am sincerely grateful to him for being a great graduate advisor.

I would like to thank the members of my committee, Dr. Françisco Raymo, Dr. Rajeev Prabhakar and Dr. James Baker for sharing their knowledge and advice. I would like to express my gratitude and admiration for them as eminent educators. I am very fortunate to have them as my graduate committee and for having great learning experiences from their graduate courses.

I would like to thank Dr. Ralf Landgraf at the Miler School of Medicine for giving me the chance to develop biochemical research skills. I would like to thank Dr. Adrienne Brown, Dr. Jyothi Dhuguru and Dr. Wenjun Liu for their contributions to the turn-on fluorescent kinase inhibitor research project. I would also like to express my appreciation to Dr. Orlando Acevedo for providing training. I would like to thank Dr. Burjor Captain for being a wonderful graduate program director as well as for being an excellent educator.

I would like to express my appreciation to Dr. Tegan Eve for providing me excellent teaching assistantship training and guidance. I am genuinely grateful to him for sharing his knowledge and advice for chemistry laboratory education.

I am thankful to Mr. Edward Torres and Dr. David Hudson for sharing their guidance and knowledge on instrumentations. I would like to thank Dr. Demar Pitter, Dr. Manuela Petaccia for being great senior lab-mates and mentors sharing passion for chemistry. I

would like to thank Anthony Cauley, Wesley Cunningham and Irene Manning for being awesome research group members.

I would like to thank the Department of Chemistry and the University of Miami for my graduate education.

Finally, I would like to thank my family for their support and best wishes.

TABLE OF CONTENTS

LIST OF FIGURES

LIST OF TABLES

LIST OF SCHEMES

Chapter 1

FLUORESCENT KINASE PROBES ENABLE IDENTIFICATION AND DYNAMIC IMAGING OF HER2(+) CELLS

1.1 Introduction

1.1.1 EGFR/ERBB family of receptor tyrosine kinase

The epithermal growth factor family of receptor tyrosine kinase (RTKs), also known as ERBB or HER family of receptors, consist of four homologous members (ERBB1, also EGFR, and ERBB2-4). ERBB receptor tyrosine kinases are crucial regulators for intercellular communications relating cell proliferation, cell survival, cell differentiation, cell maintenance and epithelial organization.[1,2] The various cellular impacts of ERBB family are attributed to complex regulation steps of ERBB signaling through multiple mechanisms including ligand binding, oligomerization, phosphorylation, clustering, phosphatase activity, and so on.[3,4,5]

The activation of ERBB receptor tyrosine kinases requires ligand binding, conformational change, and dimerization. Six mammalian ligands for EGFR have been characterized such as epidermal growth factor (EGF), transforming growth factor-α (TGFα), amphiregulin, heparin-binding EGF-like growth factor, betacellulin and epiregulin. In addition, the ligand for ERBB3 and ERBB4 are neuregulin family (NRG).[6,7] On the other hand, the ligand for ERBB2 has not been found nor characterized. Those ligands have different binding affinity toward the targeted receptor as well as different recruitment ability on dimerization. The ligand binding on the targeted ERBB family of receptor tyrosine kinases induces conformational change and leads to dimerization.

The dimerization of ERBB receptors can be achieved in homodimerization as well as heterodimerization. However, since ERBB2 has no ligand available to initiate the conformational change, ERBB2 homodimerization is not achievable.

Hence, ERBB2 is observed in heterodimerization formats with other ERBB family members on extracellular domain in the aspect of ligand activated dimerization mechanism. Along with the diversity of ligands and dimerization formats of ERBB receptors, their various cytoplasmic processes and multiple phosphorylation sites attribute to construct the complexity of ERBB signaling. In the case of homodimerization of ERBB family members, EGFR-EGFR homodimer signaling influences on its potential effector proteins such as Src, ras-GAP, PLCγ, Shc, Grb-2, GRb-7, Nck, Crk, c-CbI,c-AbI and Eps-8. ERBB3-ERBB3 homodimer is known as defective and it has no potential effector proteins nor the biological responses. The ERBB4-ERBB4 homodimer affects the potential effector proteins such as PI3K and Shc. In the case of heterodimer, the effect of activation ligand appears more vividly. Firstly, EGFR-ERBB3 heterodimer has two sets of potential effector proteins grouped by activation ligand: 1) EGF ligand bound EGFR-ERBB3 are in effect on Src, ras-Gap, PLCγ, Shc, Grb-2, GRb-7, Nck, Crk, c-CbI,c-AbI and Eps-8. 2) NRG ligand bound EGFR-ERBB3 are in effect on PI3K, Src, ras-Gap, PLCγ, Shc, Grb-2, GRb-7, Nck, Crk, and Eps-8.

Secondly, EGFR-ERBB4 heterodimer has two sets of potential effector proteins by activation ligand. 1) EGF ligand bound EGFR-ERBB3 are in effect on Src, ras-Gap, PLCγ, Shc, Grb-2, GRb-7, Nck, Crk, c-CbI,c-AbI and Eps-8. 2) NRG ligand bound EGFR-ERBB3 are in effect on PI3K, Src, ras-Gap, PLCγ, Shc, Grb-2, GRb-7, Nck,

Crk, and Eps-8. In addition, the biological responses from categorized of potential effector proteins are in different levels by heterodimer groups. The ERBB3-ERBB4 heterodimer under NRG ligand are in effect on PI3K and Shc. The heterodimerization of ERBB family with ERBB2 presents pronounced dimerization pair effect as ERBB2 does not possess the activation ligands. The ERBB2 heterodimer with ligand bound EGFR are in effect on Src, c-Yes, ras-Gap, PLCγ, Shc, Grb-2, GRb-7, Nck, Crk, c-CbI,c-AbI, Eps-8. PTP1D. The ERBB2 heterodimer with ligand bound ERBB3 are in effect on PI3K, Src, c-Yes, PLCγ, Shc, Grb-2, GRb-7, Crk, and PTP1D.[6,8]

Moreover, the dynamic equilibrium of ERBB receptor tyrosine kinases affects the signaling pathways such as activation rates of transmembrane population as well as internalized population, and recycling rates.[9]

The dysregulation of those ERBB signaling results in carcinogenesis observed in head, neck, ovarian and breast cancers by affecting cellular physiologies such as proliferation, differentiation and apoptosis.[8,10] In many types of mammalian cancer cells, overexpression of the ERBB2 receptor has been observed alongside a preference toward ERBB2 by ligand bounded EGFR/ERBB receptors as their heterodimeric partner in signaling network.[6] The heterodimers containing ERBB2 possess high signaling potency as ERBB2's effect on lowering the ligand dissociation rate resulting in prolonged signaling contributing to tumorigenesis in dysregulated system.[11,12,13] Thus, the ERBB receptor tyrosine kinases have been a major target of the modern chemotherapy regime.

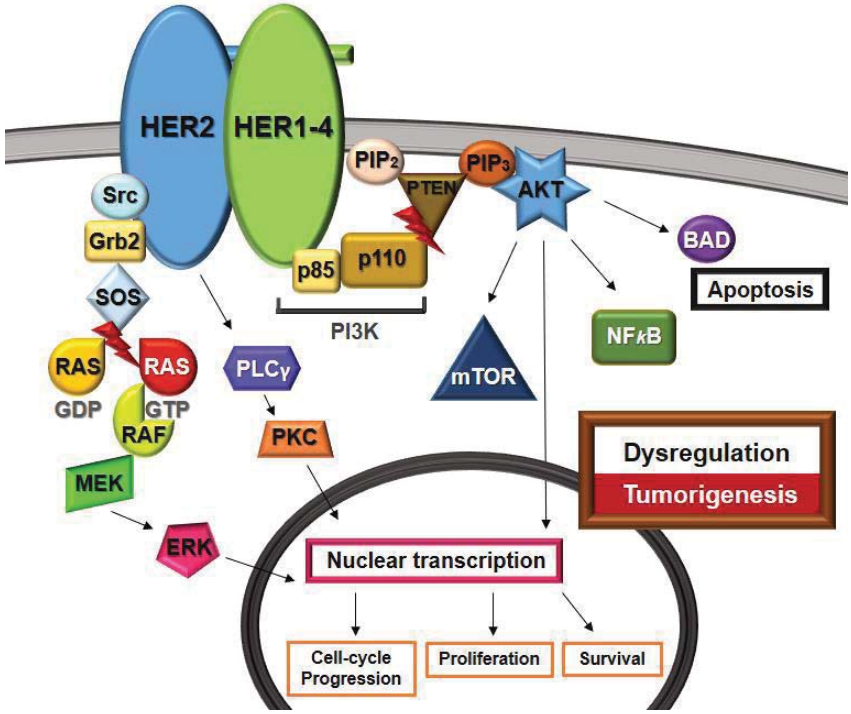

Figure 1.1. Representative HER2 mediated signaling system.

In breast cancer, the status of epithermal growth factor 2, HER2, is a crucial factor for diagnosis and decision of clinical treatment for patients. The HER2 status is classified in four categories from 0, +1, +2, +3 by HER2 expression level.[14-17] In addition, the HER2 over-expression is implicated in 20-25 % of breast cancer patients with more aggressive phenotype and less survival.[18,19] The HER2(+) breast cancer is treated with HER2 receptor oriented chemotherapy to block the dysregulated HER2 signaling pathways, while the HER2(-) breast cancer is treated through adjuvant therapy according to the subtype of malignancy.[20,21]

The degree of HER2 expression can be analyzed in DNA, mRNA, and protein levels through various biochemical techniques including PCR, RT-PCR, and immunoblotting

from cell lysate.[22] However, the averaged outcomes from the lysed cells has limitation for representing heterogeneity of individual cancer cells nor the live dynamics. Conventionally, two categories of HER2 analysis methods not requiring cell lysis have been utilized in clinical laboratory: in situ hybridization (ISH) for HER2 gene amplification testing and immunohistochemistry analysis (IHC) for measuring HER2 protein expression level.[23,24] These two methods reflect overall HER2 expression level in complementary manner from DNA level to protein expression. The HER2 protein analysis demands attention in breast cancer research to expand understanding on the aspects of tumorous HER2 kinase signaling.

1.1.2. Fluorescent inhibitors for dynamic imaging of HER2 kinase activation

In this research, small molecular fluorescent probes targeting HER2 kinase receptor have been developed as an effort to approach the dynamic information on location, expression level but also conformation change in a context of the HER2 pathway activation.[25]

Firstly, small molecular turn-on fluorescent probe can permeate the cell membrane by diffusion, and report the target information within minute units of incubation without washing step. Secondly, modulation of probe affinity on binding compared to antibody allows it to report dynamic information of HER2 receptor in real time scale. Thirdly, binding specificity of HER2 probes on activation states makes it possible to detect active and inactive conformations of HER2 receptors and responses from each state. Lastly, fluorescent inhibitors targeting intracellular ATIP binding pocket of HER2

receptor can afford co-staining with antibody-based probe binding of extracellular domain by the purpose of research.

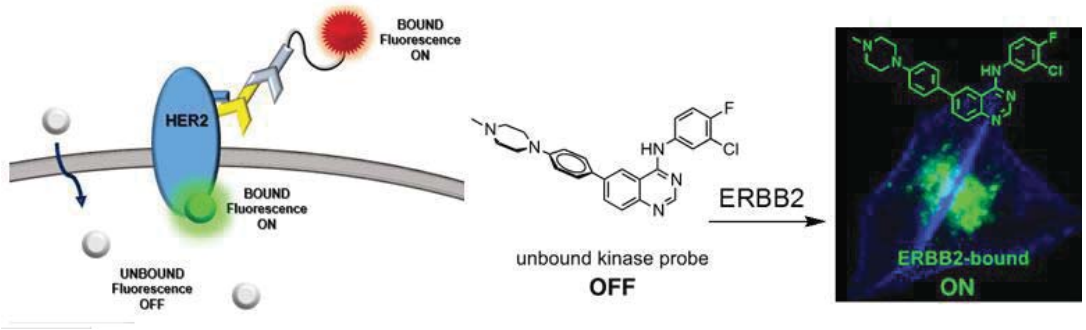

Figure 1.2. Small molecular Turn-On probe for imaging HER2 receptor tyrosine kinase. The antibody coupling probe (Red) binds to extracellular domain of HER2, while the fluorescent kinase inhibitor (Green) targets intracellular ATP-binding pocket of HER2. Structural modification of small molecular probe can modulate binding affinity as well as binding specificity by activation states.

1.2 Results and discussion

1.2.1 Design and synthesis

The tyrosine kinase fluorescent inhibitors are aimed at targeting ATP binding pocket of intercellular domain of ERBB2 tyrosine receptor kinase. The well-established pharmacophore of EGFR/ERBB, N-phenyl-4-aminoquinazoline scaffold was taken as foundation motif to generate fluorescent probes for ERBB2. Its small molecular structure can allow cell permeability via diffusion to access intracellular binding pocket. The structural similarity between 4-aminoquinazoline and adenine of ATP

provides high potential binding affinity to nucleotide position in ATP binding pocket of receptor tyrosine kinases.[26]

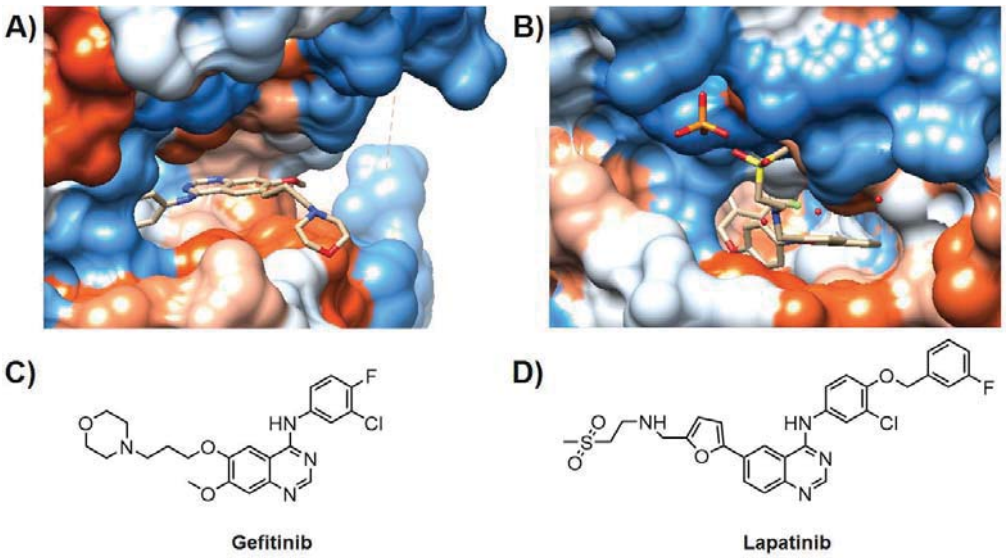

Figure 1.3. Crystal structures and chemical structures of EGFR/ERBB inhibitors. Crystal structures of the EGFR ATP-binding pocket with (A) gefitinib (PDB ID: 2ITY)[27] and (B) lapatinib (PDB ID: 1XKK)[28] reveal the inhibitor binding modes.

In aspect of binding specificity for activation states of receptor tyrosine kinase, pharmacophore aryl arm structures of clinical inhibitors for each state can be utilized in molecular designing. For Instance, taking aryl arm structure of gefitinib (Figure 1.3, A and C) Type I inhibitor for active conformation, and the Type II inhibitor lapatinib (Figure 1.3, B and D) for inactive state detection. More specifically, the quinazoline core structure is maintained for both states as the core is for universal nucleotide spot in ATP binding pocket. The activation state recognition is depending on substituent in

N-position of 4-aminoquinazoline, relatively longer substitution shown in lapatinib favors binding to inactive monomer state of ERBB ATP binding pocket, and shorter substitution in Type I class N-substituent fits perfectly to active receptor tyrosine kinase. The 6-position of N-phenyl-4-aminoquinazoline scaffold can be modified to obtain turn-on fluorescent property while remaining all important properties such as cell permeability, binding affinity and specificity.[29]

Introducing turn-on fluorescence to this inhibitor scaffold is critical to obtain valuable signals only from ERBB2 bound probes, instead of non-specific fluorescence from the specimen. By considering the environmental condition of desired probe signaling, the polarity was chosen as the best turn-on trigger for N-phenyl-4-aminoquinazoline scaffold.

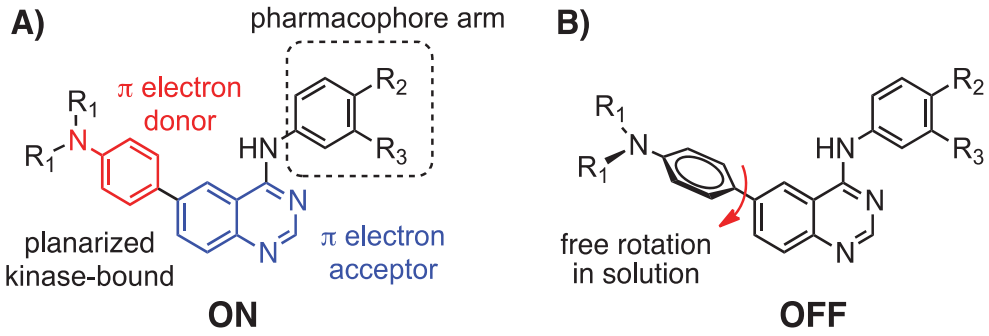

Figure 1.4. Design of an Turn-On fluorescent kinase inhibitor.

In ideal, the fluorescent signal collected are all from probes bound to ATP binding pocket of ERBB2 tyrosine kinase receptor, the transmembrane protein. The micro-environment of binding pocket of protein is hydrophobic and rigid, whereas cytoplasm is very polar and no restriction of free rotation.[30] The strategy to achieve binding

induced turn-on fluorescence is introduction of charge transfer character on molecular structure. The twisted intramolecular charge transfer (TICT) is an electron transfer process of a molecule having donor and acceptor components triggered from photoexcitation. The electron transfer process accompanies conformation change of a fluorophore in polar and low viscos environment through donor-acceptor twisting motion around single bond.[31,32] The locally excited (LE) coplanar conformer can go onto the fast relaxation pathway polar surrounding by producing perpendicular conformer which induces lower HOMO-LUMO gap significantly. The best scenario of utilizing this charge transfer character in quinazoline scaffold would be that the probe is emissive when it bound to a geometrically confined and solvent-excluding binding pocket, the π-system is being planar and emissive, while the polarized excited state is stabilized in aquatic cytosol through twisted intramolecular charge transfer (TICT) state and largely quenched. To actualize this concept, amino group is introduced on the 6-position of N-phenyl-4-aminoquinazoline scaffold which is amendable for fluorescence tuning by substituent modification as well as conjugation length.[34,35] Having N-dimethyl phenyl fragment as a π-electron donor and the quinazoline core as π-electron acceptor introduces TICT character in molecular structure upon photoexcitation (Figure 1.6). The 6-(4-(dimethylaminophenyl)-N-phenylquinazoline-4-amine is a fluorescent kinase inhibitor having K_i around 10 uM and exhibiting bright fluorescence (quantum yield: 0.37, $\lambda_{max,\ em}$: 485 nm).[29] Although the compound possessed the turn-on fluorescence property, it is not applicable for live-cell imaging because of aggregation in bio-medium. In this context, the designing of new generation

fluorescent probes was focused on improvement of solubility for live-imaging in cellular environment, and acquiring binding specificity by activation states.

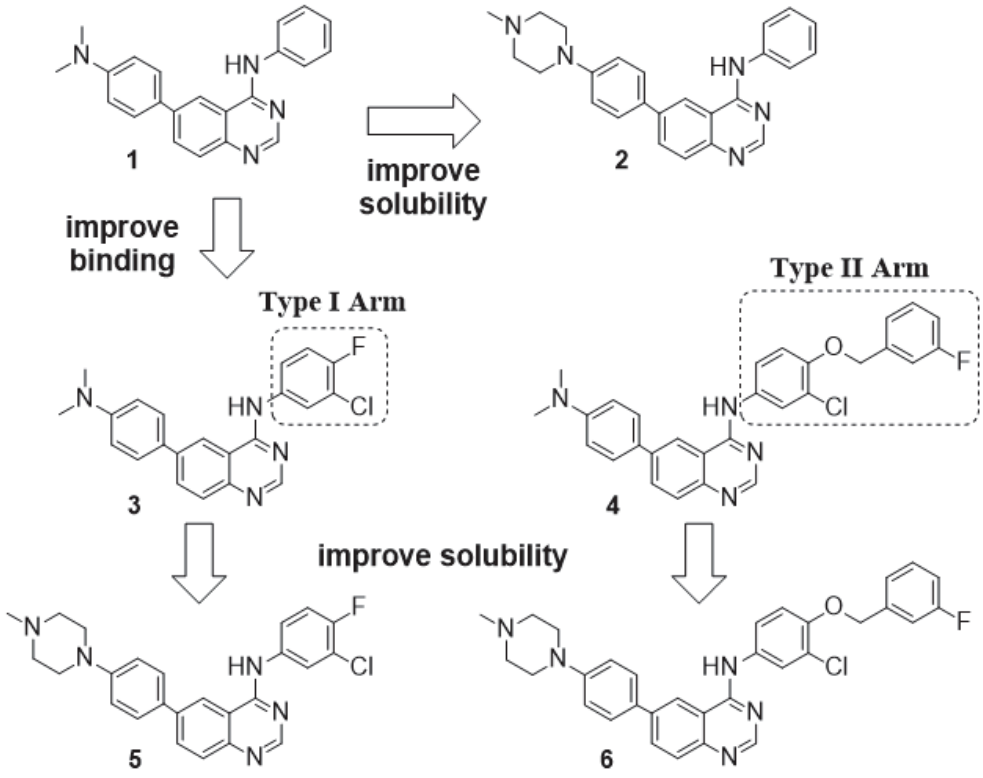

Figure 1.5. Chemical structures of fluorescent kinase inhibitors.

Firstly, replacing the N-dimethyl substituent to N-methyl piperazine leads to improvement of solubility along with maintaining fluorescence of the molecule as the further away nitrogen from phenyl ring can easily be protonated in biological environment meanwhile the closed nitrogen's lone pair electron can still participate on molecular π system as donor for optical property. Secondly, the pharmacophore arms of Type I and Type II drugs were taken to achieve binding specificity by activation

states (e.g. gefitinib structure for active conformation binder, and lapatinib structure for inactive conformation). By following the design strategies, total five compounds (**2**-**6**) were proposed as synthesis targets for potent fluorescent kinase inhibitors (Figure 1.5).

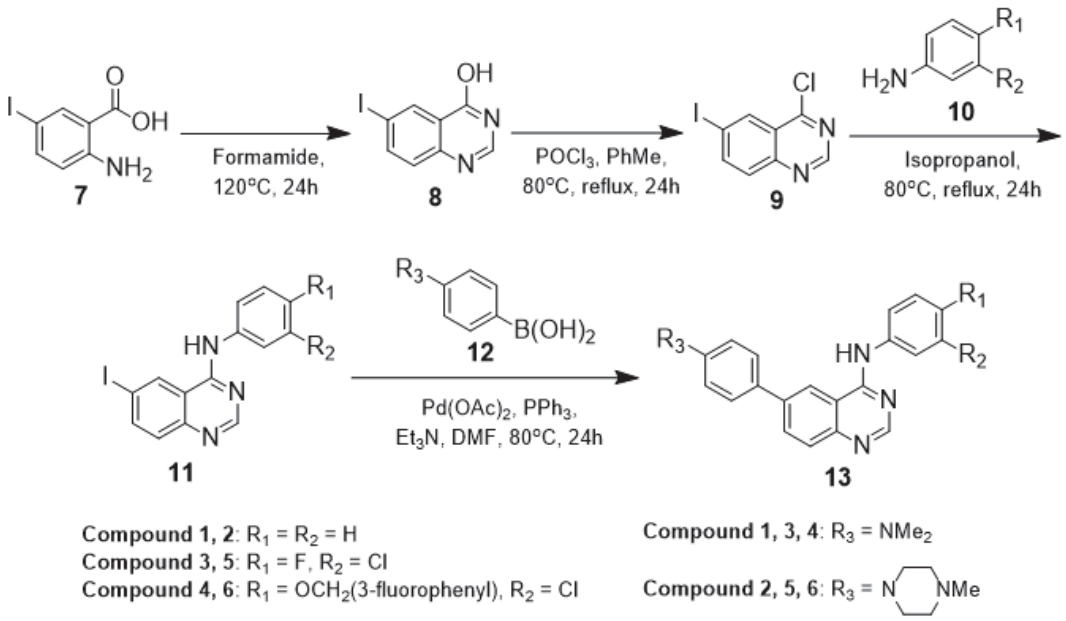

Scheme 1.1. Synthesis scheme of fluorescent kinase inhibitors.

The synthesis of targets was started from cyclization of 4-iodo-anthranilic acid to form the quinazoline core, and it followed by chlorination. The halogenated quinazoline utilized for both of active and inactive pharmacophore synthesis. For instance, substitution on chlorinated position of quinazoline core with 4-chloro-3-fluoro-aniline produces N-(3-choloro-4-fluorophenyl)-6-iodo-4-quinazolin-amine, the Type I pharmacophore based on the gefitinib. Secondly, the substitution with 3-chloro-4-((3-fluorophenyl)methoxy)-aniline on chlorinated position of quinazoline core generates

N-(3-chloro-4-((3-fluorophenyl)methoxy)phenyl)-6-iodo-4-quinazolin-amine, the Type II pharmacophore based on structure of lapatinib. The 3-chloro-4-((3-fluorophenyl)methoxy)-aniline was prepared separately through two steps, Willamson ether synthesis, and reduction of nitro group to amine. Each of 6-Iodo-quinazoline pharmacophores were used to generate complete fluorophore by Suzuki coupling with auxochromic aryl boronic acids in anaerobic condition (Scheme 1.1).[29,35-38]

Each step of reactions went through appropriate work-up processes, along with the purification through silica column chromatography, recrystallization and/or distillation. All of synthesized compounds were obtained as powder colored in white or yellow. The physicochemical characterizations of compounds were achieved through melting point measurement, IR spectra, high resolution mass spectra, ^{1}H NMR and ^{13}C NMR spectra recorded on 500 MHz spectrometer.

Synthesis of 6-(4-(4-Methylpiperazin-1-yl)phenyl)-N-phenylquinazolin-4-amine (2):

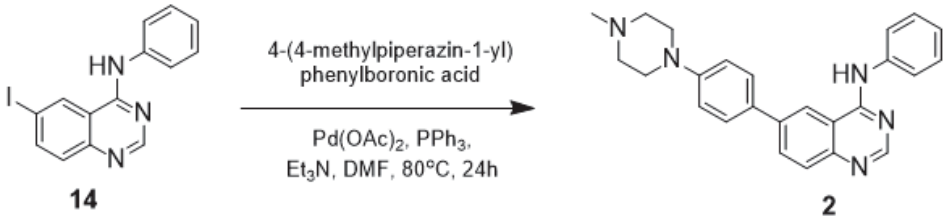

Scheme 1.2. Synthesis of compound **2**.

1.5 grams (4.3 mmol) of N-phenyl-6-iodo-4-quinazolinamine (7), 1.3 g (6.0 mmol) of 4-(4-methylpiperazin-1-yl)phenylboronic acid, 250 mg of PPh_3, 1.5 mL of Et_3N, and 5.0 mL of DMF were placed in a 50 mL Schlenk flask with a stirrer bar under nitrogen purge. The reaction mixture was degassed for a further 30 min under a slow stream of

nitrogen, at which point 220 mg of $Pd(OAc)_2$ was added. The reaction mixture was heated at 80 ºC for 24 h, cooled, poured into 300 mL of H_2O, and extracted with EtOAc (4 × 200 mL). The organic layer was dried with $MgSO_4$, filtered, and concentrated under reduced pressure. It was purified over silica (100% EtOAc to 100% MeOH) followed by crystallization from 2-propanol and then methanol to afford the white powder of 6-(4-(4-Methylpiperazin-1-yl)phenyl)-N-phenylquinazolin-4-amine.

(100 mg, 4.2%); mp: 300-302 ℃ (dec); IR $\nu_{max}(cm^{-1})$: 3032.0, 2932.5, 2837.08, 2793.95, 1937.1, 1598.6, 1567.65, 1520.8, 1498.42, 1444.8, 1422.4, 1404.5, 1360.0, 1327,.1, 1294.4, 1140.3, 846.7, 691.1; ^{1}H NMR(500 MHz, DMSO-d_6): δ: 2.23 (s, 3H), 2.47 (broad s, 4H), 3.23 (broad s, 4H), 7.08 (d, 2H, J = 7.5 Hz), 7.14 (t, 1H, J = 6.5 Hz), 7.15 (d, 2H, J = 6.0 Hz), 7.78-7.79 (m, 3H), 7.85 (d, 2H, J = 7.5 Hz), 8.13 (d, 1H, J = 8.5 Hz), 8.55 (s, 1H), 8.76 (s, 1H), 9.92 (s, 1H); ^{13}C NMR (125 MHz, DMSO-d_6), δ: 46.28, 48.14, 54.98, 115.83, 116.01, 119.17, 123.11, 124.21, 128.08, 128.69, 128.92, 129.40, 131.56, 138.37, 139.73, 148.95, 151.17, 154.46, 158.17; HR-ESI (Q-TOF) m/z: calculated for $C_{25}H_{26}N_5^+$ ($M+H^+$): 396.2188, found: 396.2192.

*6-(4-(Dimethyl-amino)phenyl)-N-(3-chloro-4-fluorophenyl)-quinazolin-4-amine (**3**).*

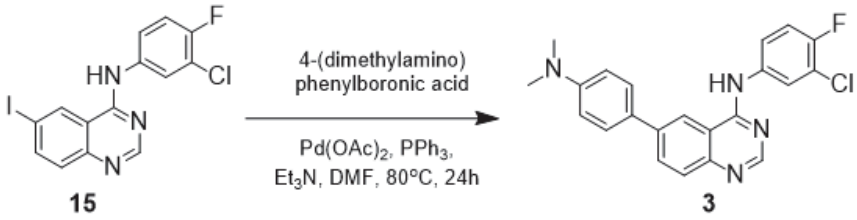

Scheme 1.3. Synthesis of compound **3**.

(75 mg, 3.8 %); mp: 261℃ (dec); IR $\nu_{max}(cm^{-1})$: 3081.2, 2938.1, 2798.0, 1935.7, 1593.3, 1563.8, 1515.4, 1499.1, 1451.8, 1419.7, 1375.5, 1355.9, 1332.9, 1286.3,

1137.9, 1332.9, 1286.3, 1137.9, 857.3, 844.3, 699.4; ^{1}H NMR(500 MHz, DMSO-d_6): δ: 2.98 (s, 6H), 6.87 (d, 2H, J = 9.0 Hz), 7.46 (t, 1H, J = 9.0 Hz), 7.75 (d, 2H, J = 9.0 Hz), 7.80 (d, 1H, J = 9.0 Hz), 7.86-7.88 (m, 1H), 8.15 (dd, 1H, J = 8.5, 1.5 Hz), 8.20 (dd, 1H, J = 7.0, 2.5 Hz), 8.59 (s, 1H), 8.69 (d, 1H, J = 1Hz), 9.96 (s, 1H); ^{13}C NMR (125 MHz, DMSO-d_6), δ: 40.47, 112.97, 115.83, 116.94-117.11 (d, J_{C-F} = 21.25 Hz), 118.44, 119.19-119.34 (d, J_{C-F} = 18.75 Hz), 122.98-123.03 (d, J_{C-F} = 6.25Hz), 124.18, 126.69, 128.09, 128.72, 131.68, 136.98-137.01 (d, J_{C-F} = 3.75 Hz), 138.97, 148.67, 150.62, 152.83-154.77 (d, J_{C-F} = 242.50 Hz), 153.95, 157.81; HR-ESI (Q-TOF) m/z: calculated for $C_{22}H_{19}ClFN_4^+$ ($M+H^+$): 393.1282, found: 393.1274.

*6-(4-(Dimethyl-amino)phenyl)-N-(3-chloro-4-((3-fluorophenyl)methoxy)phenyl)-quinazolin-4-amine (**4**)*.

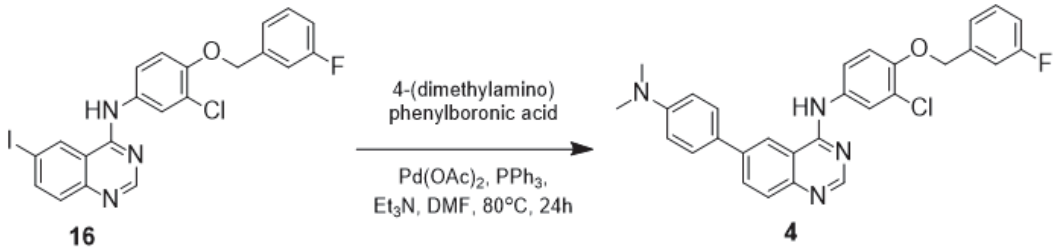

Scheme 1.4. Synthesis of compound **4**.

(131 mg, 10.2%); mp: 250℃ (dec); IR ν_{max}(cm^{-1}): 3054.7, 2908.2, 2809.3, 1926.6, 1604.6, 1572.0, 1522.7, 1498.7, 1444.7, 1420.8, 1391.0, 1359.3, 1324.8, 1293.8, 1207.7, 1127.5, 1074.5, 863.0, 685.0; ^{1}H NMR(500 MHz, DMSO-d_6): δ: 2.98 (s, 6H), 5.27 (s, 2H), 6.86 (d, 2H, J = 8.5 Hz), 7.17 (t, 1H, J = 9.0 Hz), 7.28-7.35 (m, 3H), 7.46 (dd, 1H, J = 14.0, 8.0 Hz), 7.75-7.79 (m, 4H), 8.03 (d, 1H, J = 2.5 Hz), 8.13 (dd, 1H, J = 8.5, 1.5 Hz), 8.54 (s, 1H), 8.68 (s, 1H), 9.86 (s, 1H); ^{13}C NMR (125 MHz, DMSO-d_6), δ: 40.46, 69.80, 112.98, 114.42-114.60 (d, J_{C-F} = 21.25 Hz), 114.70, 115.08-115.25

(d, $J_{C\text{-}F}$ = 21.25 Hz), 115.84, 118.45, 121.46, 122.77, 123.79-123.81 (d, $J_{C\text{-}F}$ = 2.50 Hz), 124.60, 126.75, 128.06, 128.65, 130.99-131.06 (d, $J_{C\text{-}F}$ = 8.75 Hz), 131.48, 133.70, 138.77, 140.09-140.15 (d, $J_{C\text{-}F}$ = 7.50 Hz), 148.62, 150.07, 150.59, 154.16, 157.91, 161.69-163.62 (d, $J_{C\text{-}F}$ = 241.25 Hz); HR-ESI (Q-TOF) m/z: calculated for $C_{29}H_{25}ClFN_4O^+$ ($M+H^+$): 499.1701, found: 499.1727.

*6-(4-(4-Methylpiperazin-1-yl)phenyl)-N-(3-chloro-4-fluorophenyl)-quinazolin-4-amine (**5**).*

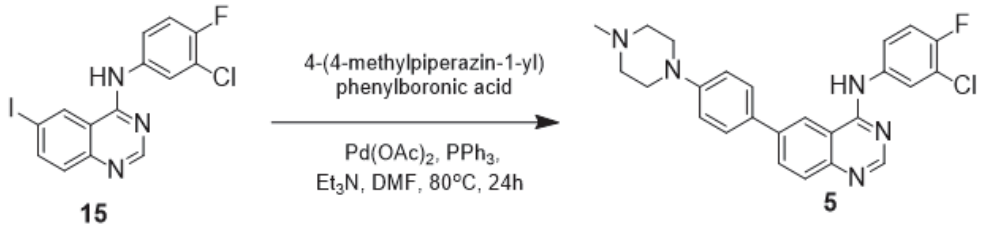

Scheme 1.5. Synthesis of compound **5**.

(79 mg, 8.8 %); mp: 280℃ (dec); IR ν_{max}(cm^{-1}): 3058.0, 2938.81, 2811.02, 1928.5, 1631.4, 1602.3, 1572.1, 1537.7, 1522.8, 1499.0, 1450.4, 1424.4, 1413.3, 1379.5, 1344.3, 1331.5, 1296.2, 1159.8, 1141.6, 864.1, 699.5; ^{1}H NMR(500 MHz, DMSO-d_6): δ: 2.22 (s, 3H), 2.45 (t, 4H, J = 4.5 Hz), 3.20 (t, 4H, J = 4.5 Hz), 7.06 (d, 2H, J = 8.5 Hz), 7.44 (t, 1H, , J = 9.0 Hz), 7.74 (d, 2H, J = 8.5 Hz), 7.80 (d, 1H, J = 8.5 Hz), 7.87-7.84(m, 1H), 8.12(d, 1H, J = 8.5 Hz), 8.18(dd, 1H, , J = 7, 2.5 Hz), 8.60 (s, 1H), 8.70 (s, 1H), 9.96 (s, 1H); ^{13}C NMR (125 MHz, DMSO-d_6), δ: 46.26, 48.10, 54.96, 115.78, 115.80, 116.94-117.12 (d, $J_{C\text{-}F}$ = 22.50 Hz), 118.98, 119.20-119.35 (d, $J_{C\text{-}F}$ = 18.75 Hz), 122.99-123.04 (d, $J_{C\text{-}F}$ = 6.25Hz), 124.20, 128.08, 128.78, 129.26, 131.78, 136.95-136.97 (d, $J_{C\text{-}F}$ = 2.5 Hz), 138.61, 148.89, 151.20, 152.85-154.79 (d, $J_{C\text{-}F}$ = 242.50 Hz),

154.15, 157.87; HR-ESI (Q-TOF) m/z: calculated for $C_{25}H_{24}ClFN_5^+$ ($M+H^+$): 448.1704, found: 448.1703.

*6-(4-(4-Methylpiperazin-1-yl)phenyl)-N-(3-chloro-4-((3-fluorophenyl)methoxy)-phenyl)-quinazolin-4-amine (**6**).*

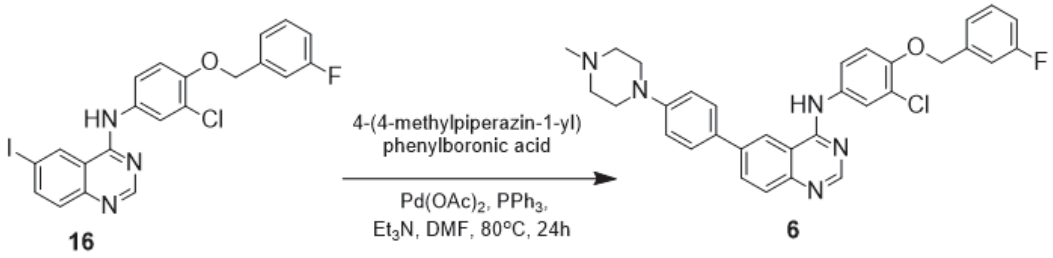

Scheme 1.6. Synthesis of compound **6**.

(91.0 mg, 8.2%); mp: 257-258℃ (dec); IR ν_{max}(cm^{-1}): 3076.9, 2939.1, 2799.7, 1935.2, 1593.7, 1564.0, 1515.9, 1497.8, 1451.6, 1416.4, 1375.5, 1356.7, 1333.6, 1286.4, 1211.6, 1137.6, 1063.7, 866.8, 699.3; ^{1}H NMR(500 MHz, DMSO-d_6): δ: 2.23 (s, 3H) 2.46 (t, 4H, J = 5.0 Hz), 3.22 (t, 4H, J = 5.0 Hz), 5.26 (s, 2H), 7.08 (d, 2H, J = 9.0 Hz), 7.17 (t, 1H, , J = 8.5 Hz), 7.28-7.34 (m, 3H), 7.45 (q, 1H, J = 8.0 Hz), 7.77-7.78(m, 3H), 7.78 (d, 1H, J = 9.0 Hz), 8.02(d, 1H, J = 2.5 Hz), 8.13(dd, 1H, J = 8.5, 1.5 Hz), 8.55 (s, 1H), 8.70 (d, 1H, J = 1.5 Hz), 9.87 (s, 1H); ^{13}C NMR (125 MHz, DMSO-d_6, TFA), δ: 42.55, 45.50, 52.56, 69.83, 114.43-114.65 (d, J_{C-F} = 22.50 Hz), 114.47, 114.67, 115.20-115.37 (d, J_{C-F} = 21.25 Hz), 116.49, 120.34, 121.16, 121.71, 123.85-123.86 (d, J_{C-F} = 1.25Hz), 125.09, 126.88, 128.30, 129.11, 130.77, 131.07-131.14 (d, J_{C-F} = 8.75 Hz), 134.48, 138.08, 139.79-139.85 (d, J_{C-F} = 7.5 Hz), 140.38, 150.24, 151.16, 152.26, 160.02, 161.70-163.63 (d, J_{C-F} = 241.25 Hz); HR-ESI (Q-TOF) m/z: calculated for $C_{26}H_{33}N_6O^+$ ($M+H^+$): 554.2156, found: 554. 2128.

1.2.2 Optical spectroscopy

Probes **2**-**6** were designed as turn-on fluorescent inhibitors and thus were expected to be non-emissive in solvents of high polarity (e.g. water, methanol) and emissive in less polar solvents.

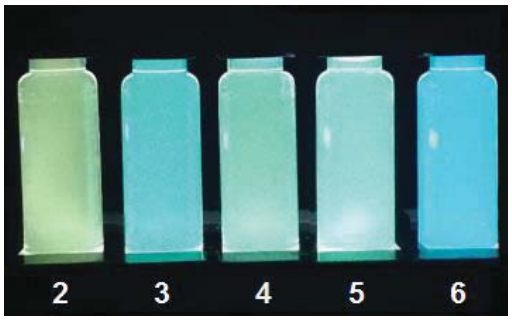

Figure 1.6. Chloroform solutions of compounds **2**-**6** in 5 μM under UV illumination at 354 nm.

This behavior can be qualitatively observed by sight as in chloroform ($E_T(30)$ = 39.1 kcal/mol)[39] solutions, most of the probes appear bright with emissions ranging from greenish blue (**2** to **6**) in Figure 1.7, while in aqueous solutions, weak or no emission was observed. To investigate their optical properties quantitatively, UV-Vis and fluorescence spectra of compounds were measured in chloroform (Figure 1.10). UV-Vis absorption spectra were obtained on a Perkin-Elmer Lamda 35 UV-Vis spectrometer using chromophore solutions of 10 μM with 1 cm path length. Fluorescence spectra were measured on a Perkin-Elmer LS55 Fluorometer using probe concentrations of 1 μM. For determination of the Φ_{em}, solutions were prepared to an optical density of less than 0.05 in order to minimized inner filter effects. Perylene in cyclohexane was used as a reference for quantum yields.[40]

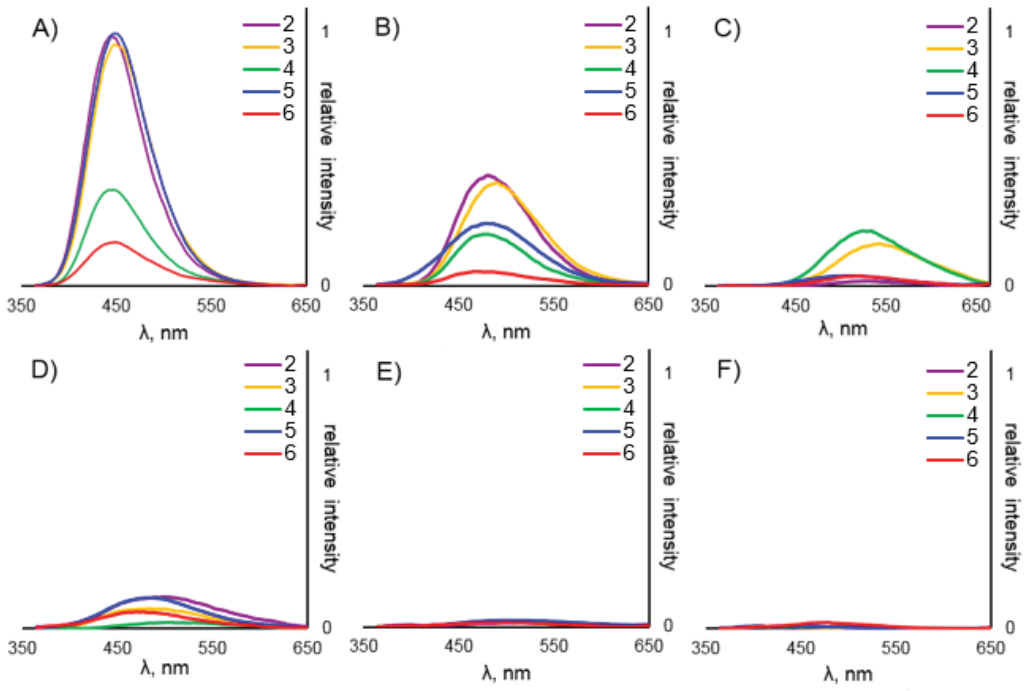

Figure 1.7. Emission spectra of **2-6** in various solvents by polarity. A) toluene, B) chloroform, C) acetonitrile, D) octanol, E) isopropanol, F) PBS.

All synthesized probes are compatible with DAPI, Hoechst 33342 or blue fluorescent protein filter sets for epifluorescence microscopy. The emission spectra of **2-6** in various solvent system are shown in Figure 1.8. All probes exhibit sensitivity on polarity of environment, which makes them as turn-on probes by turning on at the binding event at hydrophobic binding pocket, and turning off in aqueous surrounding outside of binding fold. Their absorption, emission maxima, extinction coefficient, quantum yield are presented in Table 1.1.

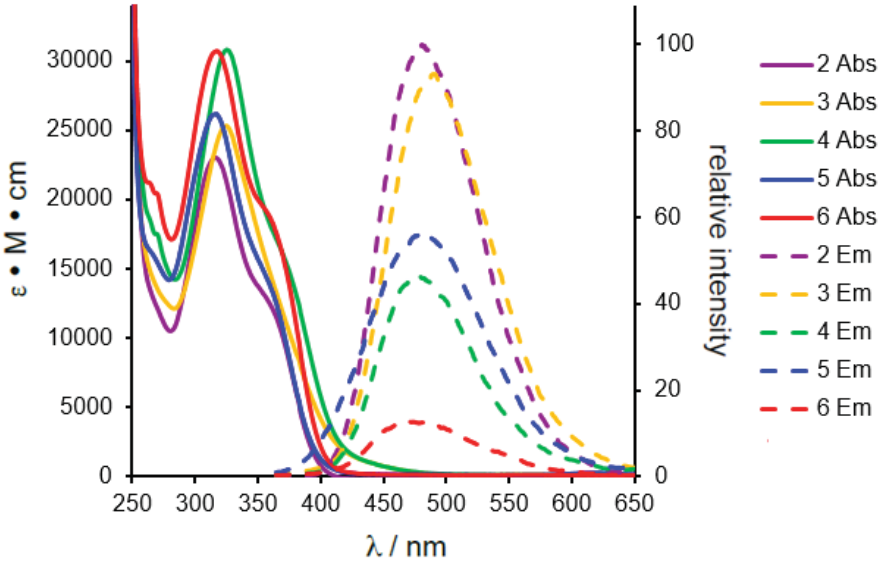

Figure 1.8. Absorption (solid lines) and emission (dashed lines) spectra of **2-6** in $CHCl_3$. Emission intensities are given relative to **2**, which has the highest quantum yield.

Table 1.1. Photophysical parameters of **2-6** in solution.

Solvent 2	PhMe	$CHCl_3$	MeCN	MeOH	IPA	BuOH	OcOH	PBS
$\lambda_{max, abs}$ (nm)	316	316	317	316	316	316	317	310
ε (M^{-1} cm^{-1})	27100	32600	37700	30500	32500	36200	31500	29900
$\lambda_{max, FL}$ (nm)	443	493	539	391	549	516	494	470
Φ_{FL}[a]	0.45	0.27	0.01	0.003	0.02	0.03	0.07	0.005
Solvent 3	PhMe	$CHCl_3$	MeCN	MeOH	IPA	BuOH	OcOH	PBS
$\lambda_{max, abs}$ (nm)	321	325	322	322	321	322	323	327
ε (M^{-1} cm^{-1})	26400	26300	28200	28200	27100	27500	26300	18700

$\lambda_{max, FL}$ (nm)	447	504	539	470	535	519	497	400
Φ_{FL}[a]	0.61	0.27	0.13	0.02	0.03	0.02	0.09	0.008
Solvent 4	PhMe	$CHCl_3$	MeCN	MeOH	IPA	BuOH	OcOH	PBS
$\lambda_{max, abs}$ (nm)	322	325	323	325	324	324	325	333
ε ($M^{-1}cm^{-1}$)	29900	30800	34000	30900	31200	30700	29900	24100
$\lambda_{max, FL}$ (nm)	440	477	530	610	493	512	494	396
Φ_{FL}[a]	0.21	0.12	0.13	0.01	0.02	0.02	0.07	0.008
Solvent 5	PhMe	$CHCl_3$	MeCN	MeOH	IPA	BuOH	OcOH	PBS
$\lambda_{max, abs}$ (nm)	317	317	316	314	315	316	317	315
ε ($M^{-1}cm^{-1}$)	26300	26200	30700	27200	27300	27700	28000	27300
$\lambda_{max, FL}$ (nm)	456	488	522	505	496	450	505	440
Φ_{FL}[a]	0.64	0.23	0.03	0.05	0.03	0.03	0.11	0.01
Solvent 6	PhMe	$CHCl_3$	MeCN	MeOH	IPA	BuOH	OcOH	PBS
$\lambda_{max, abs}$ (nm)	317	317	317	317	317	318	319	325
ε ($M^{-1}cm^{-1}$)	28400	30700	34400	30200	30000	29800	28200	24900
$\lambda_{max, FL}$ (nm)	442	475	512	502	475	535	490	477
Φ_{FL}[a]	0.10	0.04	0.02	0.02	0.02	0.02	0.06	0.02

[a]± 10%

Water ($E_T(30)$ = 63.1 kcal/mol, η = 0.89 mPa•s) and octanol ($E_T(30)$ = 48.3 kcal/mol, η = 7.24 mPa•s) represent two distinct environments that can be used to assess the physical properties and distribution of organic molecules.[40,41] The partition coefficient

of drug-like molecule represents an insight of its potential distribution and pharmacokinetics in cellular environment. The chemico-physical properties of **1-6** were calculated through SwissADME (Table 1.2). The log $P_{o/w}$ is a partition coefficient calculated by following topological method, and log K_p is representing the degree of skin permeation according to QSPR model.[42-44]

Table 1.2. Chemico-physical properties of **1-6**.

Compounds / Properties	1	2	3	4	5	6
Molar refractivity	108.72	130.78	113.69	144.67	135.75	166.72
Topological polar surface area	41.05 Å	44.29 Å	41.05 Å	50.28 Å	44.29 Å	53.52 Å
log $P_{o/w}$	3.91	3.72	4.77	5.40	4.56	5.15
log K_p	-4.71 cm/s	-5.18 cm/s	-4.51 cm/s	-4.12 cm/s	-4.99 cm/s	-4.59 cm/s
BBB Permeant	Yes	Yes	No	No	Yes	No
GI absorption	High	High	High	Low	High	High

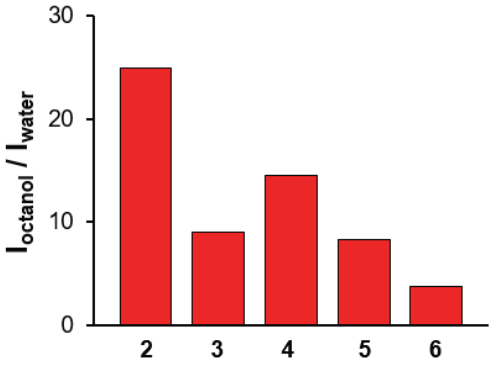

Figure 1.9. Emission intensities of **2-6** obtained in octanol and water present fluorescence turn ON/OFF ratios.

The turn-on ratio is also considered as a measure for responsiveness of probes towarding the changes of chemical microenvironment.[45] The ratios of **2**-**6** emission intensities obtained in octanol and water are shown in Figure 1.9, and the turn-on ratio of **1** was reported as 57.[29]

1.2.3 Inhibition study

Initially we evaluated all of 5 probes as inhibitors of ERBB2 phosphorylation in MCF7 cells using 6 probe concentrations, 0, 39, 156, 625, 2500 and 10000 nM.

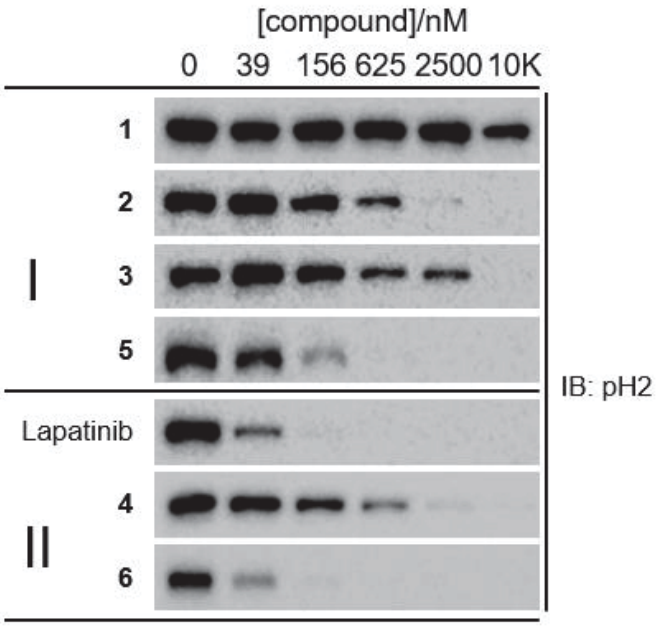

Figure 1.10. Inhibition of NRGβ1-induced ERBB2 tyrosine phosphorylation in MCF7 cells at 6 concentrations by compounds.

MCF7 cells are a well-established model system for the ligand induced activation of ERBB2-ERBB3 hetero-complexes by ligand of the neuregulin family (NRGβ1 in this case). In evaluation, MCF cells were seeded with equal quantity (200 thousand/well)

in six-well plates. After 48 hours, cells were pre-treated with small molecule inhibitors of various concentrations for 30 minutes before induction by neuregulin (NRGβ1, 30 nM, 30 minutes). Cell lysates were generated immediately by SDS lysis. Equal aliquots were subjected to SDS-PAGE and Western blot analysis. ERBB2 phosphorylation was evaluated for Tyr1139 located close to the extreme cytoplasmic C-terminus of the receptor (validated by pan-TyrP detection (4G10)). The signal obtained for pTyr1139 relative to the ERBB2 receptor levels was determined as the relative receptor phosphorylation.[46]

These results of western blot analysis suggest that substituting N-dimethyl-phenyl to N-methyl-piperazinyl-phenyl at 6-position of the quinazoline-core enhances binding affinity toward ATP binding pocket of ERBB2 dramatically regardless of pharmacophore arm types. It resulted from increment of solubility by having additional nitrogen in N-dimethyl-piperazinyl functional group, readily protonated in biological medium.

The western blot results demonstrate several features of these fluorescent quinazoline probes: First, despite of chemical modification, the probes remain membrane permeability and are able to access the intracellular kinase binding domain of ERBB2. Secondly, solubility increment with 6-position position dramatically improves inhibition capability. Thirdly, regardless of 6-position modification, having the Type I and II pharmacophore arm at 4-position of the quinazoline enhances inhibition of ERBB2 phosphorylation than simple having simple phenyl group. More precisely, the addition of the N-methyl piperazine arm at 6-position of the quinazoline core effectively lowers the Ki from approximately 10 μM for **1** to 360 nM for **2**. The addition

of the Type I pharmacophore arm at 4-position lowers the K_i to about 3 μM, for **3**, on the other hand the Type II arm has more pronounced effect with a K_i of 500 nM for **4**. The fully optimized Type I and Type II fluorescent inhibitors **5** and **6** have K_i values of 71 nM and 27 nM, compatible to both of experimentally measured and reported value (20 nM and 13 nM, respectively) for lapatinib.[28] This allows partial target occupancy at low probe concentrations, thus minimizing limitations imposed by solubility, and unspecific binding.

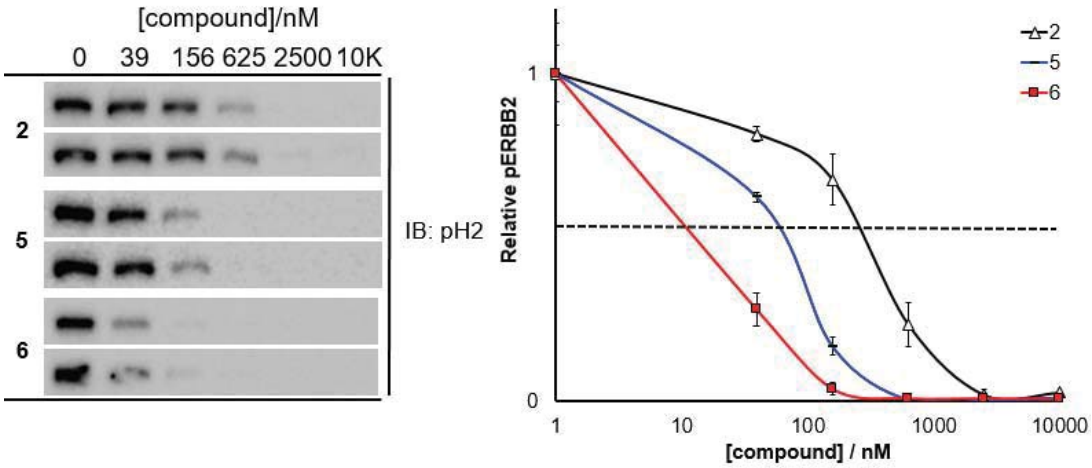

Figure 1.11. Relative inhibition of NRG β1-induced ERBB2 phosphorylation in MCF7 cells by compounds **2**, **5**, and **6**.

1.2.4 Binding induced fluorescence study

Emission spectroscopy identified the probe **5** and **6** that they exhibited appropriate turn-on ratios, and the phosphorylation inhibition studies demonstrated that those probes were capable of accessing the ATP-binding pocket of ERBB2. To determine if turn-on emission is observed upon binding event to ERBB2, the fluorescence spectra of **5** and

6 in PBS were measured with the presence and absence of the soluble ERBB2 kinase domain. In PBS alone, the emission of the probes is largely quenched in PBS alone, whereas the addition of the ERBB2 kinase domain produced substantial turn-on emission enhancements for both probes: turn-on ratios of 11 and 4 were calculated for **5** and **6**, respectively. Emission lifetimes are shown next to their associated spectrum, however **5** in PBS is precluded from lifetime measurements due to its weak fluorescence in PBS. The higher hydrophobicity of **6** may contribute to aggregation in solution, leading to some fluorescent aggregates which are distinguishable by their unique emission lifetime.

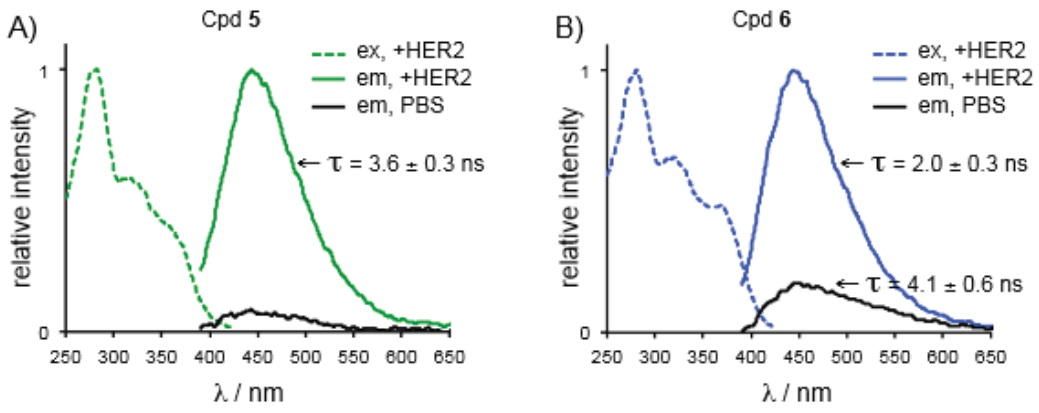

Figure 1.12. Excitation and emission spectra of probes **5** (A) and **6** (B) in PBS +/- purified HER2 kinase domain.

In addition, the emission maxima are moderately blue-shifted by approximately 40 nm, relative to $CHCl_3$ solutions. Additional confirmation of the binding-induced emission

response comes from the excited spectra, which present pronounced peaks at 280 nm, which are absent in the absorption spectra and are most likely due to energy transfer from tyrosine and tryptophan residues around ATP binding pocket.

1.2.5 Confocal microscopy

To evaluate their ability to target the receptor tyrosine kinases in a live cell setting, confocal microscopy experiments were conducted. For imaging experiment, cells were seeded at a density of 10^5 cell/cm^2 in 96 micro-well plates. Cells maintained a normal morphology during the course of the experiments in maximum 90 minutes, and remained adhered to the imaging plate. Single photon imaging was performed on a Leica SP5 confocal microscope. For imaging of **5** and **6** in 2 μM, a 405 nm laser line was utilized and the emission window was set between 450 and 550 nm, with the aperture opened to 200 μm to minimize the effects of z-drift. Cells were labeled an anti-ERBB2 antibody directed towards the extracellular domain of ERBB2 (Ab-5, Millipore) followed by Alexafluor 546 secondary antibody. Excitation of Alexafluor 546 was achieved with the 561 nm laser line and emission was collected between 575 and 625 nm. Images were processed in Fiji.[47] Quantitative analysis of single cells was performed by circumscribing individual cells, which were identified in the phase contrast image. All clearly demarcated and in-focus cells in a single field of view were included in each analysis followed by excluding cell debris, out of focus and overlapping cells.

Specific detection of ERBB2 by activation states

The ability of these fluorescent probes detecting active state of ERBB2 was evaluated by confocal imaging experiment. BT474 cells (10^6 receptors/cell) classified as HER2(+) were utilized in dual labeling experiments to compare the fluorescent kinase probes against monoclonal antibody. In the first row of Figure 1.13, the BT474 stained with ERBB2 antibody, then treated with fluorescent kinase probe **5** detecting ERBB2 in active conformation.

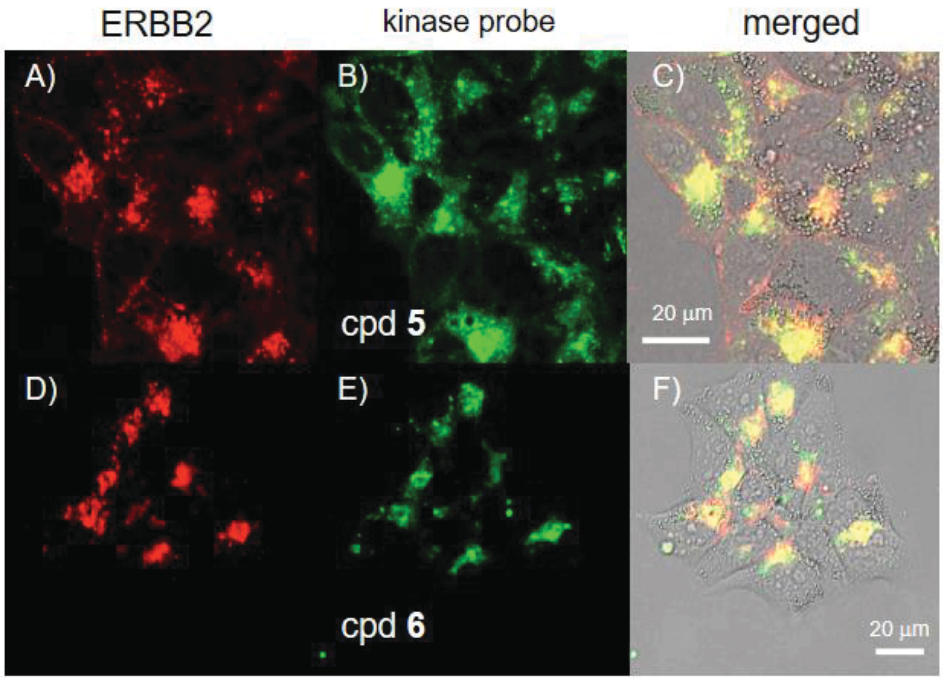

Figure 1.13. Confocal microscopy of **5** detecting active conformation of ERBB2. Co-staining of BT474 cells with ERBB2-directed antibody (A) and probe, **5** (B), overlay (C). Confocal microscopy of **6** detecting inactive conformation of ERBB2: co-staining of BT474 cells with ERBB2-directed antibody (D) and probe, **6** (E), overlay (F). Probe concentration = 2 µM, λ_{em} = 450-550 nm

The overlay of the two imaging channels presents significant overlap between the anti-ERBB2, shown in red, and **5**, in green, with co-localization in yellow. In addition, the second row of Figure 1.13, presents the experiment with **6** for detecting ERBB2 with inactive conformation. These results demonstrate that binding affinity of probes is maintained even in the complex intracellular environment with high degree of selectivity for ERBB2 preserved. Time course measurements in Figure 1.14 revealed that the binding of **5** is more rapid than that for **6** with is in good agreement with models of Type I and Type II binding kinetics.[48]

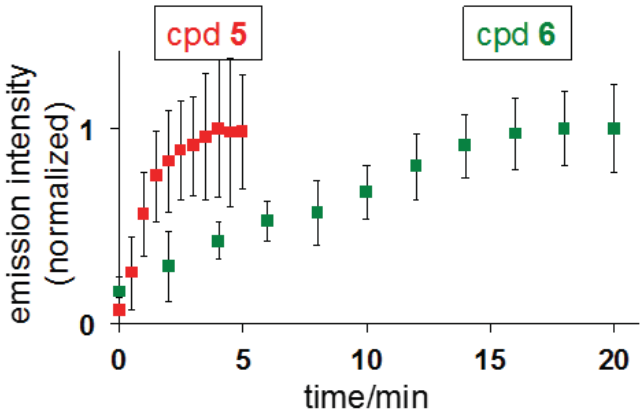

Figure 1.14. Time dependent emission intensities of BT474 cells treated with **5** and **6** (both 2 μM). Error bars show standard deviation.

Her2(+) cell recognition between co-seeded breast cancer cell lines

The probe ability of differentiating HER2(+) from HER2(-) cells was evaluated through confocal microscopy experiments. The ERBB2 overexpressing BT474 cells are well-researched representation for HER2(+) specimen and another breast cancer cell line, MCF7, carrying ERBB2 at low levels (10^4 copies/cell), are classified clinically as HER2(-). These two breast cancer cell lines were chosen for this confocal

microscopy experiment and co-seeded. As probe **5** exhibited more rapid uptake and higher brightness than probe **6**, it was selected for experiment. Figure 1.18 shows co-seeded MCF7 and BT474 cells were treated with anti-ERBB2 and labeled secondary antibody (red, first row) and fluorescent probe **5** (green, second row).

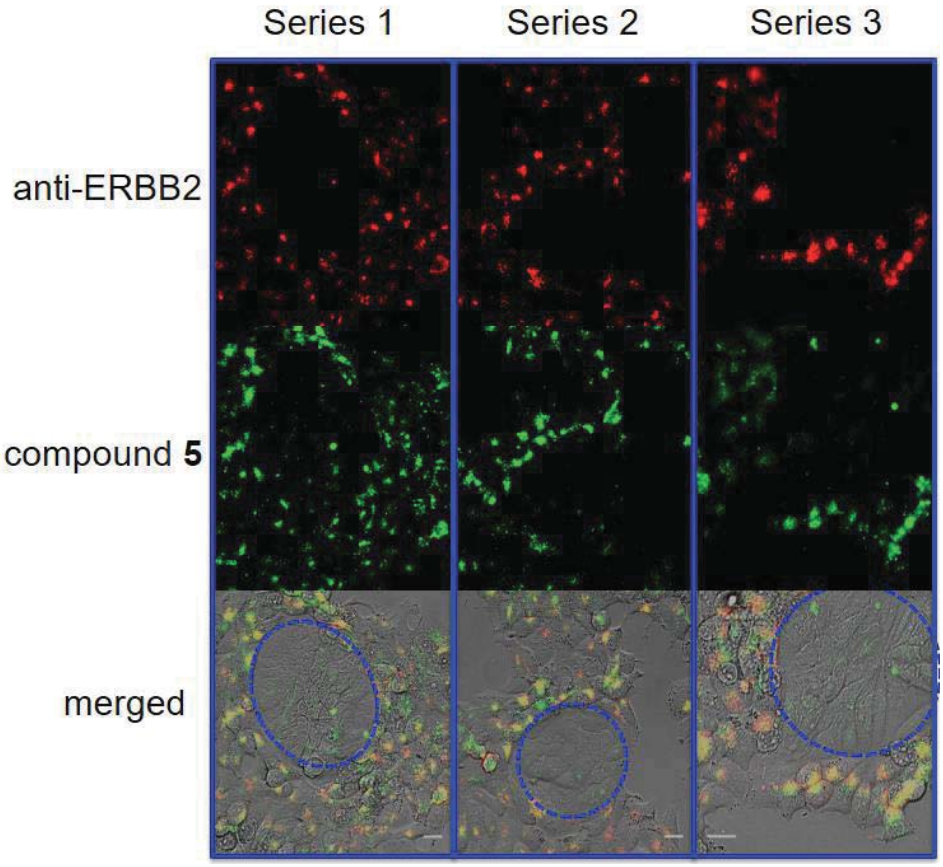

Figure 1.15. Dual staining of BT474 and MCF7 (encircled in merged image) cells with probe **5**.

The specimens were imaged under similar conditions as the BT474 cells in Figure 1.13. Significant overlap is seen between the fluorophore-tagged antibody and kinase probe **5** emission in the BT474 cell, HER2(+). On the other hand, HER2(-), MCF7 cells,

encircled in third row in Figure 1.15, can readily be discerned both by their morphology, as well as the near absence of anti-ERBB2 staining, compared to the BT474 cells. Relatively weak and disperse emission from **5** is visible in the MCF7 cells, which is not surprising as they do express ERBB2, albeit at much lower levels, however, the BT474 cells are readily distinguished by their bright emissive patches. Quantitative analysis from 10 experiments with 250 cells each, reveals that BT474 cells exhibit higher emission intensity than MCF7 cells and marked signal heterogeneity. This can be seen qualitatively in Figure 1.15 and 1.16, demonstrating the ability of **5** to identify ERBB2(+) cells.

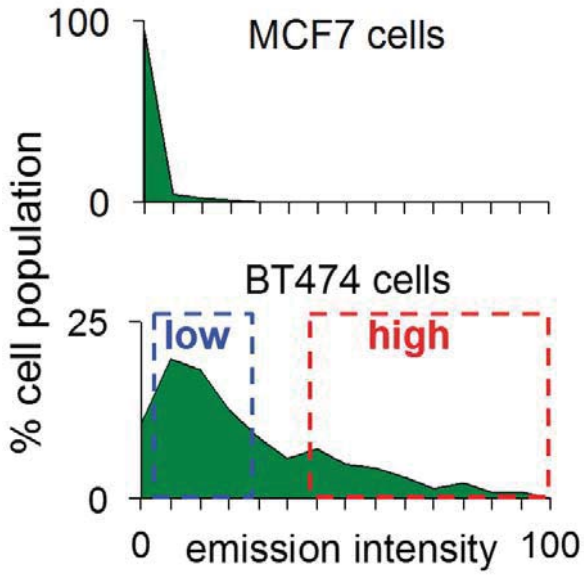

Figure 1.16. The emission histogram of probe **5** for quantitative analysis of the cell population.

Time dependent ligand-probe interaction study

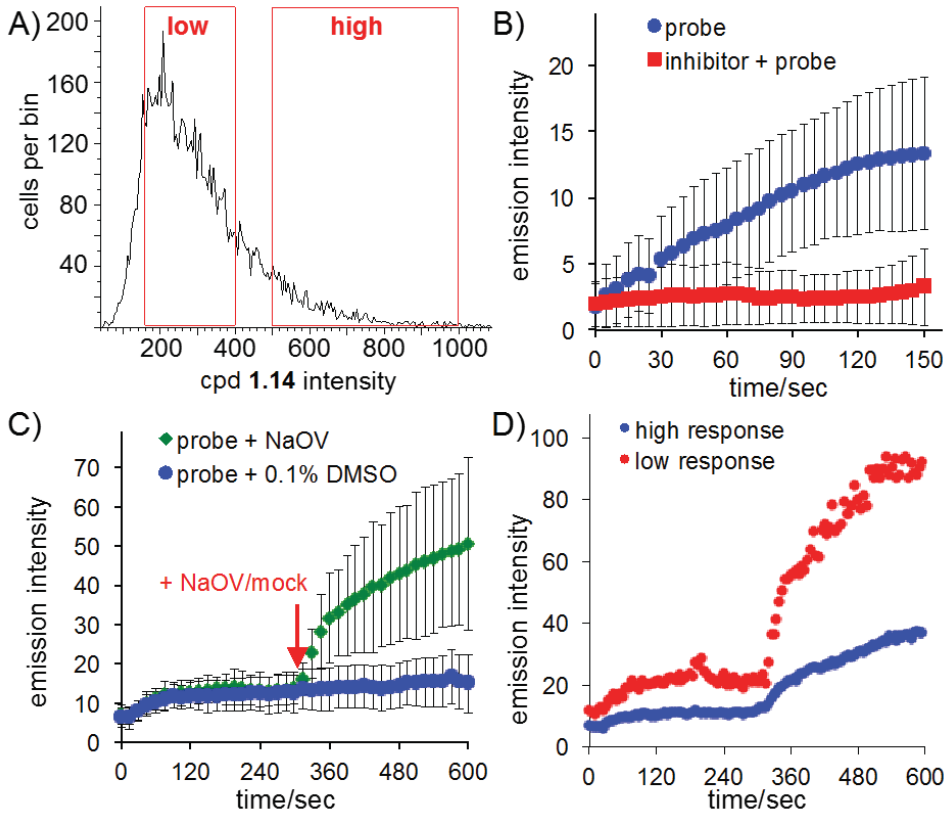

Figure 1.17. Fluorescent kinase inhibitor **5** responses. A) The FACS histogram of BT474 cells treated with **5**. B) Pretreatment with an ERBB2 inhibitor, CI-1033, significantly lowers the binding induced fluorescent signal. C) Tyrosine-phosphatase inhibitor, NaOV, increases ERBB2 activation state population inducing rapid increase in emission intensity of BT474 cells treated with 5. D) The error bars, showing S.D., in panel C reflect the population heterogeneity, which can be clearly seen in single cell analysis of high and low responding cells.

The higher level of ERBB2 expression in BT474 cells clearly allows for increased binding of **5**, which is reflected in higher emission intensity from BT474 cells compared to MCF7 cells. The emission histogram (Figure 1.16) reveals considerable

heterogeneity in the kinase probe signal within the BT474 population. This may simple reflect receptor levels or could report cell-to-cell variability in the number of receptors in an activated state. Thus, fluorescence activated cell sorting (FACS) experiment on BT474 cells treated with **5**, was followed as its capable of analyzing a much larger number of cells, the data would be more reliable. Cells were sorted into two populations displaying high and low probe signal, followed by a 24 hours recovery prior to western blot analysis of ERBB2 receptor levels and phosphor-tyrosine state.

Even after the 24 hours recovery period, cells with high probe emission intensity showed a relative receptor phosphorylation that was 25 % higher than the cells classified as low intensity, suggesting that besides receptor levels, the basal activation state reflected a stable and cell specific feature. Thus, in addition to being able to discriminate ERBB2 overexpressing cells from cells from cells expressing normal levels, fluorescent kinase probes can also report cell to cell variation on the receptor activation state within a population. The readout provides a unique and versatile complement to traditional, static immune-histochemical labeling.

The FACS data combined with western blot assay indicate that differences in activation states can be detected on a subpopulation level. Based on this, probe 5 was examined further for its ability to track rapid perturbations of the activation states at the level of individual cells.

Firstly, the fluorescence intensity of **5** in BT474 cells rapidly reaches a maximum within several minutes of probe addition (Figure 1.17). This increment in fluorescence does not occur in cells pretreated with the ERBB2-directed, irreversible Type I kinase inhibitor, CI-1033 (Canertinib), validating probe specificity in a complex cellular

setting. Although BT474 cells possesses a large population of auto-activated ERBB2 receptors, the fraction of activated receptors is kept low by competing actions of tyrosine-phosphatases. Blocking of tyrosine phosphatases is known to rapidly shift the equilibrium towards a predominance of activated states, conventionally measured by endpoint measurements of tyrosine phosphorylation.[49-51]

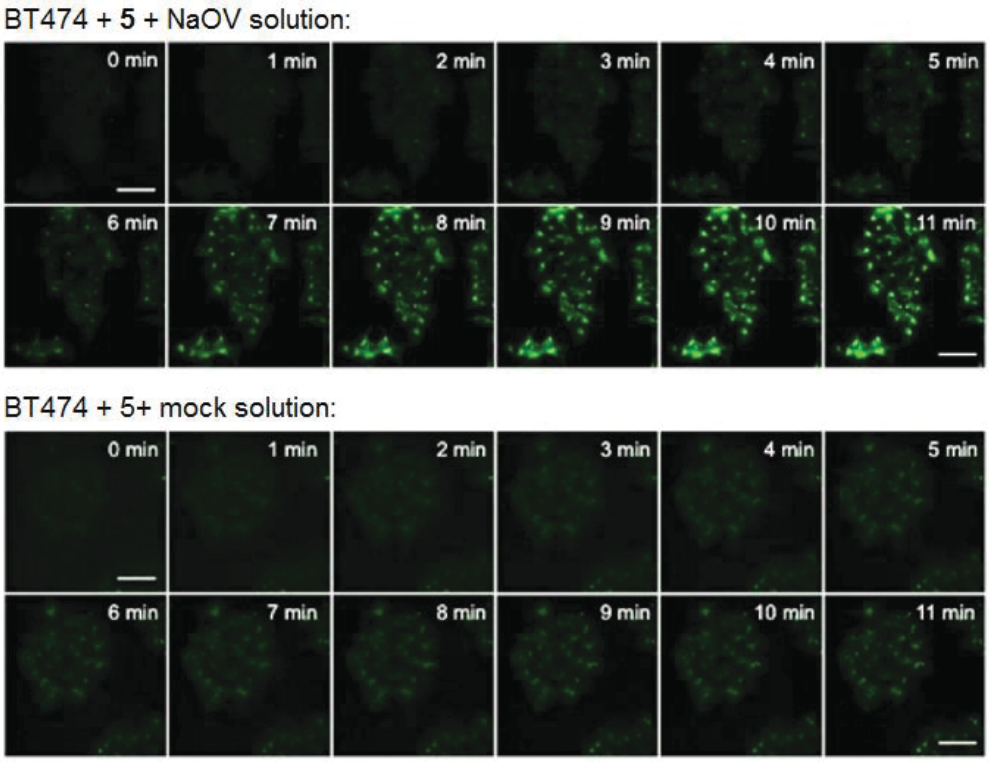

Figure 1.18. Time course images of BT474 cells treated with **5** (2 μM at t = 0) then 0.1 % NaOV solution (top) or DMSO mock solution (bottom).

When BT474 cells were pre-incubated with probe **5** for 5 minutes, the addition of a tyrosine phosphatase inhibitor, sodium orthovanadate (NaOV), results in a rapid increase in probe signal (Figure 1.17C). One key interpretation of this NaOV-induced activation is that the fluorescent kinase probe, although inhibitory at saturating

concentrations, does not block the activation response. The variability of the signal is not a reflection of the signal to noise ratio of individual measurements, rather it reveals cell-to-cell variability in activation states, information that is typically lost in bulk analyses. Figure 1.17D showing traces of two individual cells that represent high and low responders that are consistent with FACS histogram. This data represents a novel route towards the analysis of cellular factors that control actual activation states of an oncogenic receptor on a single cell level.

1.3 Conclusion

In this research, we have generated live cell compatible, high affinity kinase probes that identify ERBB2 overexpressing cells, HER2(+) through a binding induced emission response. The combined observations utilizing the optimized active state probe **5**, demonstrate that kinase-targeted molecular reporters are capable of stratifying individual live cells by their dynamic response to activation. With the increasing emphasis on cancer heterogeneity and single cell signaling studies, this work adds a powerful tool to the available toolset. This capability can be merged with rapidly developing single cell expression and genetic analysis to probe dynamic responses in receptor kinase signaling and perturbation of this signaling by agonists and antagonists.

Chapter 2

A NOVEL CORE SCAFFOLD FOR DEVELOPMENT OF FLUORESCENT ERBB INHIBITORS: SYNTHESIS AND PHOTOPHYSICAL CHARACTERIZATION OF A BENZOFUSED QUINAZOLINE

2.1 Overview

Our efforts on developing ERBB2 probes introduced several examples of fluorogenic molecular probes targeted at the ATP binding fold of this kinase family based on the N-phenyl-4-amino-quinazoline pharmacophore.[25] Their binding affinity toward ERBB2 allows probes to identify ERBB2 overexpression through a binding induced fluorescence response. The significance of quinazoline class probes that we developed can provide efficient detection methodology of HER2 dynamics for live breast cancer cells.[26]

To improve optical properties of quinazoline class probes, we investigate a novel fluorescent scaffold for kinase probes having bathochromic shifted emission. Possessing the red-shifted, lower energy excitation is desired for fluorescent probe used in live cells to reduce oxidative stress from UV irradiation. In addition, bathochromic shifted, long wavelength emission allows to minimize the detection of auto-fluorescence in cells as well as increase the tissue penetration depth.[52,53]

2.2 Results and discussion

2.2.1 Design and synthesis

The N-phenyl-4-amino quinazoline derivatives are well-established adenosine analogs that display relatively high affinity and selectivity ($K_i \approx 10^{-7}$-10^{-8} M) for the ERBB family.[43,61]

By extending the aromatic framework of this core, previously generated several fluorogenic analogs exhibit emission enhancements upon binding to the ERBB2 kinase domain.[25,26,29] Two of the most promising examples of reported family of substituted quinazolines, **1** and **18** shown in Figure 2.1, display excellent overall brightness, high turn-on ratios and are compatible with commercially available filter sets (e.g. DAPI/Hoechst) or excitation sources. Though they are structurally similar, **18** possesses a vinylene bridge between the electron-donating anilino group and the electron withdrawing quinazoline core. While this extension of the p-system does bathochromically shift $\lambda_{max,\ abs}$ by 56 nm, compared with **1**, there is only a minor shift of 10 nm in the emission spectrum.[29] For multiplexed analysis utilizing these probes, a further red shift in the fluorescent spectrum would be desirable, in order to avoid spectral overlap. Substrate specificity can be fine-tuned through the N-phenyl arm, specifically at the R_3 and R_4 positions, while improvements to the optical properties can be engineered into the quinazoline core and via the R_1 and R_2 positions. We therefore embarked on studies aimed at designing an improved chromophore scaffold that retains basic components of the quinazoline pharmacophore but would be compatible with further modifications to the N-phenyl pharmacophore arm. The attractive optical properties of benzofused analogs of nucleobases reported by Kool and others,[55-58] motivated our investigation of **19**. Their absorption and emission maxima can be red-shifted by up to 70 nm, with quantum yields increased by several orders of magnitude compared with the parent nucleobases. Thus, a benzofused derivative of **1**, or etheno-bridged derivative of **18**, to produce **19**, is one possible route for achieving further red shifts in the excitation and emission spectra of fluorescent EGFR/ERBB

inhibitors. In this contribution, we achieved the synthesis and optical studies on a benzofused quinazoline, **19**. Beginning with commercially available 3-amino-2-naphthoic acid, we generated 6-bromo-3-amino-2-naphthoic acid in two steps according to reference 56.

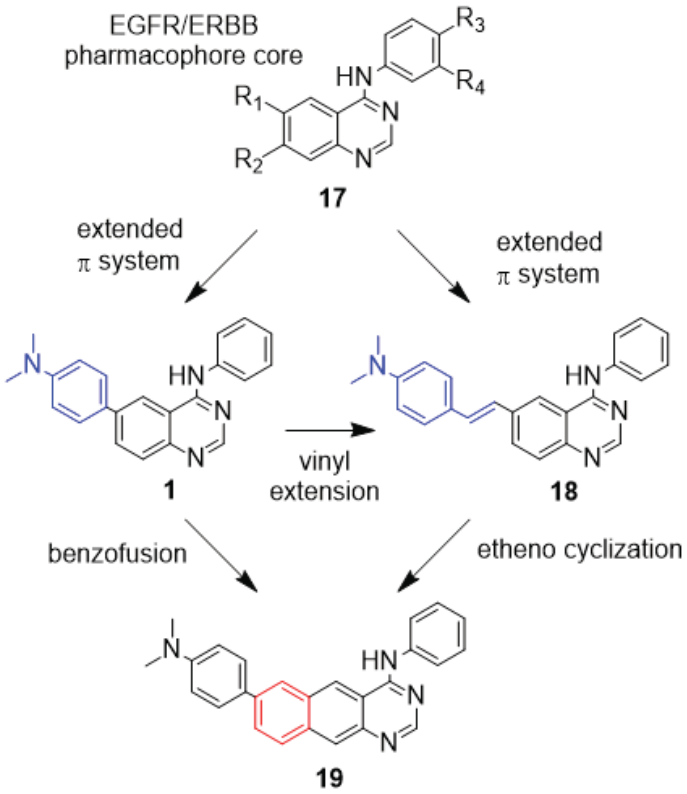

Figure 2.1. EGFR/ERBB-targeted inhibitors, such as erlotinib, gefitinib and lapatinib, are built upon a tunable N-phenyl-4-aminoquinazoline core **17**. By expending the π system of this pharmacophore, our research group have previously generated fluorescent ERBB2 inhibitors such as **1** and **18**.[29] Compound **19** can be viewed as the benzo-fused derivative of **1** or the etheno-cyclized derivative of **18**.

Condensation with formamide afforded the key intermediate, **23** (Scheme 2.1), which, upon chlorination with $POCl_3$, allows for the incorporation of different N-aryl pharmacophore units through nucleophilic aromatic substitution. As we were primarily interested in exploring the optical properties of the chromophore core, we utilized aniline to generate a simple N-phenyl derivative, **24**. The use of a substituted aniline would generate a pharmacophore analogous to gefitinib, neratinib or lapatinib with improved binding and selectivity for the ERBB family. The donor-acceptor p-system was completed through a Suzuki coupling of **24** with 4-(dimethylamino)phenyl boronic acid, producing **19** as an orange powder.

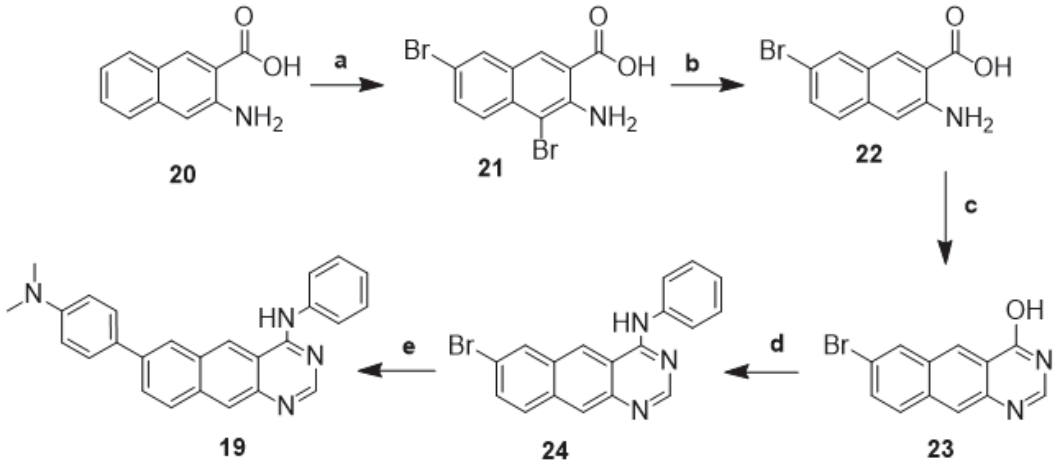

Scheme 2.1. Synthetic route to **19**: (a) Br_2, HOAc (58%); (b) Sn, HCl, HOAc (88%); (c) formamide (96%); (d) i. $POCl_3$, ii. aniline, 2-propanol (6%); (e) 4-(dimethylamino) phenylboronic acid hydrochloride, PPh_3, Et_3N, DMF, $Pd(OAc)_2$ (14%).

The physicochemical characterization of compounds was achieved through melting point measurement, IR spectra, high resolution mass spectra, ^{1}H NMR and ^{13}C NMR spectra recorded on 500 MHz spectrometer.

*Synthesis of 7-bromo-benzo[g]quinazolin-4(1H)-one (**23**)*

7.75 grams (29.0 mmol) of 3-amino-7-bromo-naphthalene-2-carboxylic acid and 4.0 mL (100 mmol) of formamide were placed in a 200 mL pressure vessel with a stir bar. The reaction was vigorously stirred and heated at 160 ºC overnight, cooled to room temperature, then poured into 250 mL of H_2O. This mixture was stirred for 20 min, then the brown precipitate was collected by suction filtration, dried in a 220 ºC oven for 2 hours, then under vacuum overnight to afford 7-bromo-benzo[g]quinazolin-4(1H)-one (7.7 g, 96.2%). Characterization data: mp: 302-304℃ (dec); IR $\nu_{max}(cm^{-1})$: 3243.9, 3115.7, 2895.4, 1866.3, 1688.3, 1652.7, 1621.4, 1591.6, 1491.6, 1412.7, 1352.3, 1309.0, 1283.6, 1259.5, 1238.7, 1208.8, 1149.16, 1065.0, 862.2, 677.8; ^{1}H NMR(500 MHz, DMSO-d_6): δ: 7.68 (d, 1H, J = 8.5 Hz), 7.98 (d, 1H, , J = 8.5 Hz), 8.07 (s, 1H), 8.19 (s, 1H), 8.43 (s, 1H), 8.75 (s, 1H), 12.1 (s, 1H); ^{13}C NMR (125 MHz, DMSO-d_6), δ: 119.97, 122.92, 125.50, 127.09, 130.48, 131.33, 131.83, 132.27, 134.86, 145.05, 145.45, 161.47; HR-ESI (Q-TOF) m/z: calculated for $C_{12}H_8BrN_2O^+$ ($M+H^+$): 274.9820, found: 274.9823.

*Synthesis of 7-bromo-N-(phenyl)-benzo[g]quinazolin-4-amine (**24**):*

1.5 grams (5.5 mmol) of **23**, 10.0 mL of $POCl_3$, and 10.0 mL of toluene were placed in a 100 mL round bottom flask with a stirrer bar and heated at 90 ºC for 16 h. $POCl_3$ and

toluene were distilled off of the reaction mixture under reduced pressure leaving a dark brown solid that was used without further purification. 1.0 g (10.7 mmol) of aniline, and 2-propanol, sufficient to allow the mixture to stir, were added directly to the flask containing the crude chlorinated product. The reaction mixture was vigorously stirred and heated at 80 ºC for 24 hours. The reaction mixture was cooled to room temperature, concentrated under reduced pressure, then 20 mL of 1M KOH solution was added and allowed to stir for 20 min. 200 mL of EtOAc was added to this mixture then organic layer was separated and concentrated. The concentrate was purified over silica (100% CH_2Cl_2 to 100% EtOAc) followed by crystallization from methanol to 7-bromo-N-(phenyl)-benzo[g]quinazolin-4-amine as a yellow powder (110.0 mg, 5.7 %). Characterization data: mp: 254-255 ºC; IR ν_{max}(cm^{-1}): 3260.2, 3061.6, 2799.1, 1927.2, 1607.3, 1524.8, 1515.4, 1498.2, 1447.0, 1404.2, 1367.9, 1306.4, 1247.7, 1198.6, 1131.2, 1058.3, 887.2, 689.4, 669.9; ^{1}H NMR(500 MHz, DMSO-d_6), δ: 7.19 (t, 1H, J = 7.0 Hz), 7.43 (t, 2H, J = 7.5 Hz), 7.76 (d, 1H, J = 8.5 Hz), 7.93 (d, 2H, J = 7.5 Hz), 8.14 (d, 1H, J = 9.0 Hz), 8.30 (s, 1H), 8.45 (s, 1H), 8.61 (s, 1H), 9.22 (s, 1H), 10.17 (s, 1H); ^{13}C NMR (125 MHz, DMSO-d_6 with TFA), δ: 113.60, 117.38, 121.59, 125.36, 125.84, 127.72, 129.35, 130.47, 131.09, 132.64, 133.69, 133.93, 134.70, 136.77, 152.57, 160.86; HR-ESI (Q-TOF) m/z: calculated for $C_{18}H_{13}BrN_3^+$ ($M+H^+$): 350.0293, found: 350.0289.

*Synthesis of 7-(4-(dimethyl-amino)phenyl)-N-(phenyl)-benzo[g]quinazolin-4-amine (**19**).*

100 milligrams (0.28 mmol) of **9**, 115 mg (0.57 mmol) of 4-(dimethylamino)phenylboronic acid hydrochloride, 10 mg of PPh_3, 2.0 mL of Et_3N, and 1.0 mL of DMF were placed in a 25 mL Schlenk flask with a stirrer bar under nitrogen purge. The reaction mixture was degassed for a 30 min under a slow stream of nitrogen, at which point 10 mg of $Pd(OAc)_2$ was added. The reaction was heated at 80 ºC for 24 h, cooled and filtered to remove solid material. The eluate was poured into 50 mL of H_2O, with ethyl acetate used to rinse the collection flask and capture the remaining residue. The filtered solid impurity was discarded and eluted solution was extracted three times with 200 mL of ethyl acetate. The organic layer was dried with $MgSO_4$, filtered, and then concentrated under reduced pressure. The solid was dissolved in the minimum volume of CH_2Cl_2 required and this solution was added to 100 mL of hexane dropwise, producing a precipitate, which was collected by suction filtration. This dark orange material was then crystallized from methanol, producing 7-(4-(dimethyl-amino)phenyl)-N-(phenyl)-benzo[g]quinazolin-4-amine as a dark orange powder (14.3 mg, 14.3 %). Characterization data: mp: 256-258 ℃ (dec); IR ν_{max}(cm^{-1}): 3260.6, 3062.1, 3012.9, 1943.0, 1606.2, 1592.9, 1562.8, 1551.9, 1495.5, 1445.8, 1402.7, 1304.0, 1282.4, 1241.0, 1193.9, 1124.3, 1057.5, 1029.8, 963.3, 878.0, 709.8, 689.9; ^{1}H NMR(500 MHz, DMSO-d_6), δ: 2.98 (s, 6H), 6.87 (d, 2H, J = 8.0 Hz), 7.16 (d, 1H, , J = 7.0 Hz), 7.42 (t, 2H, J = 7.5 Hz), 7.72-7.74 (m, 2H), 7.97 (broad s, 3H), 8.17 (d, 1H, J = 8.5 Hz), 8.21 (s, 1H), 8.37 (s, 1H), 8.57 (s, 1H), 9.26 (s, 1H), 10.09 (s, 1H); ^{13}C NMR (125 MHz, DMSO-d_6), δ: 40.45, 113.26, 115.89, 122.82, 123.30,

123.53, 124.31, 125.11, 127.07, 127.77, 127.91, 128.83, 128.96, 131.98, 134.55, 138.15, 139.67, 145.31, 150.63, 154.26, 158.56; HR-ESI (Q-TOF) m/z: calculated for $C_{26}H_{23}N_4^+$ ($M+H^+$): 391.1923, found: 391.1936.

2.2.2 Optical spectroscopy and quantum calculation

Inspection of $CHCl_3$ solutions of **1**, **18** and **19** provided a rapid, qualitative assessment of their emission properties. Under UV illumination (354 nm), **19** fluoresces bright yellow-green, demonstrating that benzo-fusion has significantly red-shifted emission relative to **1** and **18**, which appear blue-green (Figure 2.2).

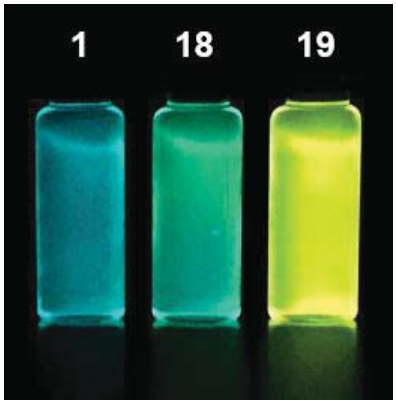

Figure 2.2. Visible comparison of UV-illuminated (354 nm) $CHCl_3$ solutions demonstrate the significant red shift in emission of **19** achieved through benzo fusion.

To quantitatively compare the optical properties of these three fluorophores, we next performed UV-vis and fluorescence spectroscopy. The absorption spectrum of **19** in $CHCl_3$ exhibits two distinct maxima at 329 and 418 nm (Fig. 2.3). TD-DFT calculations allow us to assign the longer wavelength peak as the $S_0 \rightarrow S_1$ transition.[59-61] The S_1 state

should exhibit significant charge transfer (CT) character as a result of the one electron transfer from the HOMO, localized on the electron-donating 4-(dimethylamino)phenyl arm, to the LUMO localized largely on the quinazoline core.

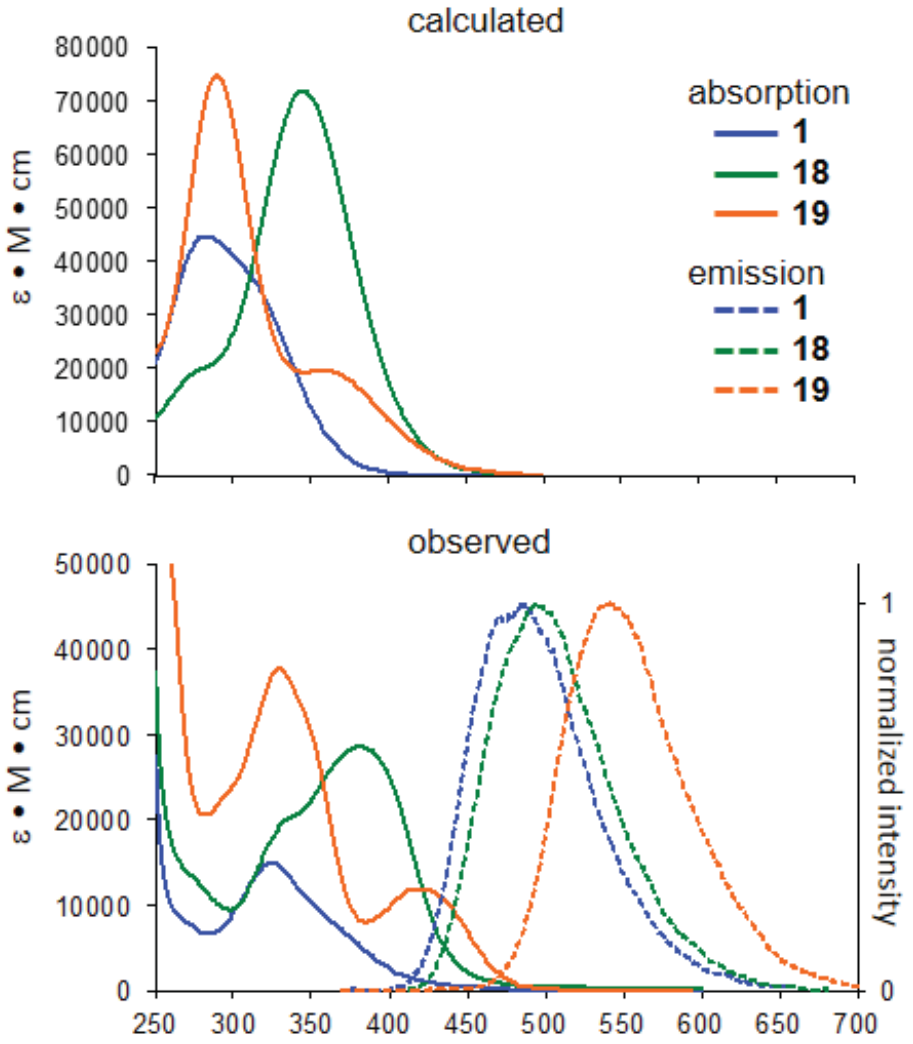

Figure 2.3. A) Calculated and B) observed solution UV-vis and emission spectra of **19** in comparison with previously reported **1** and **18**; [dyes] = 10 μM and 1 μM in $CHCl_3$ for absorption and emission spectra, respectively. The SMD solvent model[59] was utilized for TD-DFT calculations.[60,61]

The more prominent, and shorter wavelength, peak is the result of overlapping $S_0 \rightarrow S_2$ and $S_0 \rightarrow S_3$ transitions. The emission of **19** is centered at 541 nm, which is significantly red-shifted compared **1** and **18**, which have emission maxima at 485 and 495 nm, respectively. Interestingly, while **18** and **19** are similar in overall length and overlap to a large degree in their absorption spectra, **19** exhibits markedly longer wavelength emission. For imaging purposes, this bathochromic shift is a significant improvement and should minimize spectral overlap and channel cross-talk for the combination of **1** and **19**.

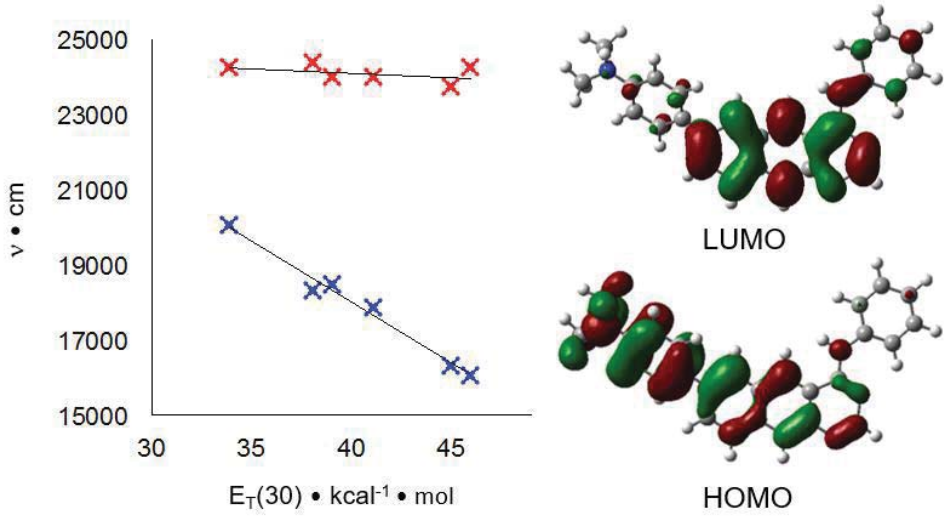

Figure 2.4. Dependence of $\lambda_{max, abs}$ (red) and $\lambda_{max, em}$ (blue) on solvent polarity using Reichardt's $E_T(30)$ scale.[39] The excited state is stabilized in more polar solvents, indicating a polarized charge transfer state, while the ground state is not responsive to changes in solvent polarity.

The absorption maxima of **19** vary little with solvent polarity (Fig 2.4, Table 2.1), demonstrating that the ground state is relatively apolar and not stabilized to an appreciable degree in more polar solvents. By contrast, the emission maxima do exhibit a significant dependence on solvent polarity, with more polar solvents lowering the energy of the S_1 state, supporting the notion that the excited state possesses a significant degree of CT character.

Table 2.1. Photophysical parameters of **19** in solution.

Solvent	$\lambda_{max, abs}$ (nm)	ε (M^{-1} cm^{-1})	$\lambda_{max, FL}$ (nm)	Φ_{FL}[a]	τ_{FL} (ns)
PhMe	413 328	14400 40300	499	0.43	6.5 ± 0.1
CH_2Cl_2	417 328	12900 40500	560	0.29	9.4 ± 0.1
$CHCl_3$	417 329	11900 37800	541	0.33	9.4 ± 0.1
EtOAc	411 325	13800 41600	547	0.22	6.8 ± 0.1
MeCN	413 325	12800 39900	622	0.09	2.2 ± 0.1
DMSO	420 332	13200 38500	613	0.01	2.3 ± 0.1
PBS	435 334	9700 27100	545	10^{-3}	-

[a] ± 10%

The quantum yield of fluorescence, f_{em}, is also highly dependent on solvent polarity. In toluene, a relatively nonpolar solvent with an $E_T(30)$ value of 33.9 kcal/mol on Reichardt's polarity scale, the quantum yield was 0.43.[39] In DMSO, emission is nearly abolished (f_{FL} = 0.01) and in phosphate buffered saline (PBS), **19** is essentially non-emissive.

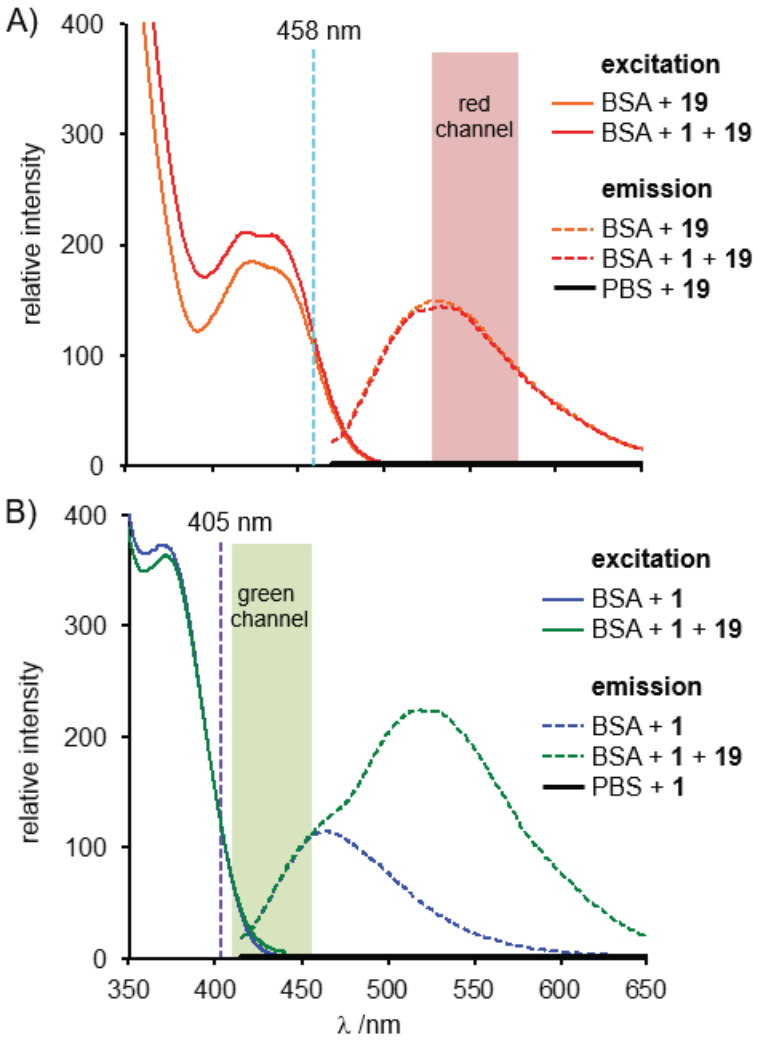

Figure 2.5. Optical spectra and imaging parameters. While both are quenched in PBS alone, the addition of BSA elicits a turn-on emission response. A) Excitation spectra scans (λ_{em} = 550 nm) of BSA + **19** and BSA + **1** + **19** shows virtually no difference at an excitation wavelength of 458 nm. B) While exciting a solution of BSA + **1** + **19** at 405 nm results in emission from both **1** and **19**, the emission between 415 and 450 nm is exclusively from **1** and is captured in the green channel for imaging. [**1**] = [**19**] = 1 μM, [BSA] = 10 μM.

The high sensitivity of **19** to its chemical environment suggests that this fluorophore core is an effective "turn-on" fluorescent probe. Through chemical modification of the N-aryl arm, the binding affinity and specificity towards the ERBB family may be fine-tuned. Although lacking a high-affinity, ERBB-specific pharmacophore arm, we could still examine the binding-induced turn-on fluorescence of **19** in the presence of serum albumin, a carrier protein for a broad range of lipophilic small molecules. While 4 is non-fluorescent in PBS solution, the addition of bovine serum albumin (BSA), produced a dramatic (~65-fold) increase in emission intensity with a peak at 535 nm (Figure 2.5A).

Given the strong correlation between the emission energy and solvent polarity, this wavelength suggests a relatively nonpolar binding pocket, approximated by a solvent such as $CHCl_3$ in which the $\lambda_{max,\ em}$ of **19** is 541 nm. As previously reported, **1** also exhibits a turn-on emission response, with emission at much shorter wavelengths compared to 4 (Figure 2.5B). When excited at 405 nm, corresponding to the shortest wavelength excitation on many confocal microscopes, the emission of **1** could be selectively captured in the range of 415 to 450 nm. Conversely, the fluorescence of **19** could be selectively obtained by exciting at 458 nm, one of the lines of an argon laser, and capturing the emission from 525 to 575 nm.

This spectroscopic data suggests that **1** and **19** are an optically compatible pair of probes, that can be used simultaneously, with each probe assigned a unique emission channel. To evaluate their use in tandem, we next obtained the excitation and emission spectra of **1** + **19** in the presence of BSA for comparison with the spectra of the individual dyes in the presence of BSA.

The emission spectra of **1** + **19** with BSA, excited at 458 nm, is virtually identical to the emission of **19** with BSA (Figure 2.5A). This allow us to resolve the emission of **19** into a red channel (false colored) in subsequent microscopy experiments. When the combination of dyes was excited at 405 nm (Figure 2.5B), both the emission of **1** and **19** could be observed, however, in the 415 to 460 nm range, the emission spectrum of **1** + **19** is indistinguishable from that of **1**. Thus, the emission of **1** can be assigned to a green channel (false colored) in this region for our microscopy experiments.

2.2.3 Confocal microscopy

Firstly, MCF7 cells were cultured in sterile T-75 flasks. Cells were maintained in RPMI containing 10% dialyzed FBS, penicillin (100 units/mL) and streptomycin (0.01%) solution under a humidified 5% CO_2 atmosphere. For imaging, cells were seeded at a density of 10^5 cell/cm^2 in 96 microwell plates. Cells maintained a normal morphology during the course of the experiments (maximum of 30 min) and remained adhered to the imaging plate.

As a demonstration of the dual color imaging capability of **1** and **19**, we exposed MCF7 cells to solutions of **1**, **19** or **1** + **19**. Although the probes are moderately hydrophobic, the cells were cultured in media containing FBS, which has a high content of BSA. The dyes were readily solubilized in the culture media and were found to accumulate intracellularly and fluoresce as previously reported for lapatinib.[62] The confocal microscope was configured according to the optical parameters outlined in Figure 2.5, and all three cell + dye combinations were imaged under identical conditions. Single photon imaging was performed on a Leica SP5 confocal microscope using 405 nm

excitation for **1** and 458 nm excitation for **19**. Emission windows were adjusted for individual PMTs to 415 to 460 nm (green channel, **1**) and 525-575 nm (red channel, **19**). All images were processed in Fiji and no adjustments to image intensity or contrast were made.

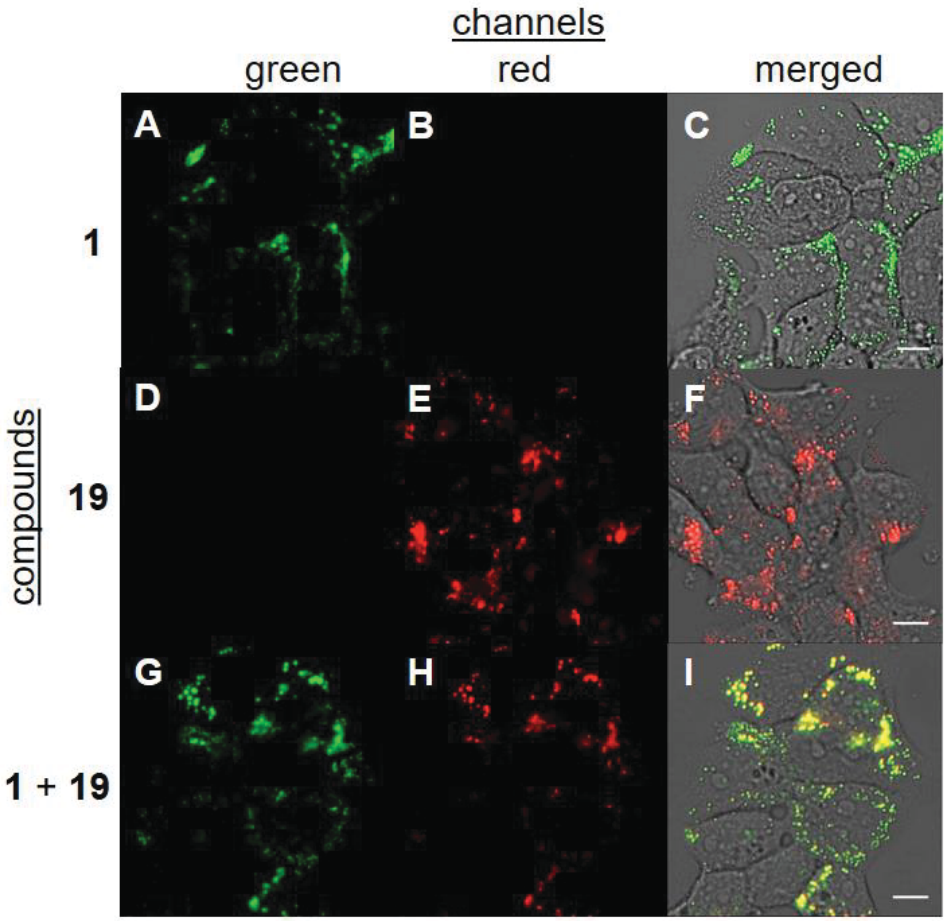

Figure 2.6. Confocal microscopy of MCF7 cells exposed to **1** (A-C) and **19** (D-F) individually, and in tandem (G-H). Each series of images was obtained under the exact same conditions of adjacent wells of a 96-microwell imaging plate. No cross-talk is observed between the green and red channels (see imaging parameters in Figure 2.5); **1** is emissive in the green channel, but not the red, while **19** is emissive only in the red channel. Scale bars are 10 μm.

Conversely, cells treated with **19** showed similar staining patterns that fluoresced in the red channel (Figure 2.6E), but exhibited no emission in the green channel (Figure 2.6D). The results of the individual probe treatments demonstrated that there is no channel cross-talk and that the dyes can be imaged independently. The combination of **1** + **19** proved that when both dyes are present, fluorescence is observed in both channels (Figure 2.6G, H). Not surprisingly, the dyes aggregate in similar regions as shown in the channel overlays (yellow regions, Figure 2.6I). These results validate the two probe, two channel capability of these turn-on fluorescent dyes.

2.3 Conclusion

By extending the aromatic framework of **1**, through benzo-fusion, we have generated a turn-on fluorescent probe, **19**, with significantly red-shifted fluorescence. Optical spectroscopy and confocal microscopy demonstrate that **1** and **19** exhibit sufficiently segregated excitation and emission spectra, allowing for resolution into two distinct channels. While neither probe possesses sufficiently high affinity or selectivity for the EGFR/ERBB family of receptor tyrosine kinases, the modular synthesis enables fine tuning of the pharmacophore arm independently of the chromophore backbone.

Chapter 3

OPTIMIZATON AND EVALUATION OF BENZOFUSED QUINAZOLINE PROBES

3.1 Overview

We have examined that the aromatic extension of quinazoline core can effectively induce bathochromic shifted emission through vinyl extension and benzo-fusion. As an effort to generate biocompatible version of fluorescent kinase probes based on novel scaffold, we focused on optimizing binding affinity by increasing solubility as well as binding specificity by activation states of ERBB2 receptor tyrosine kinase.

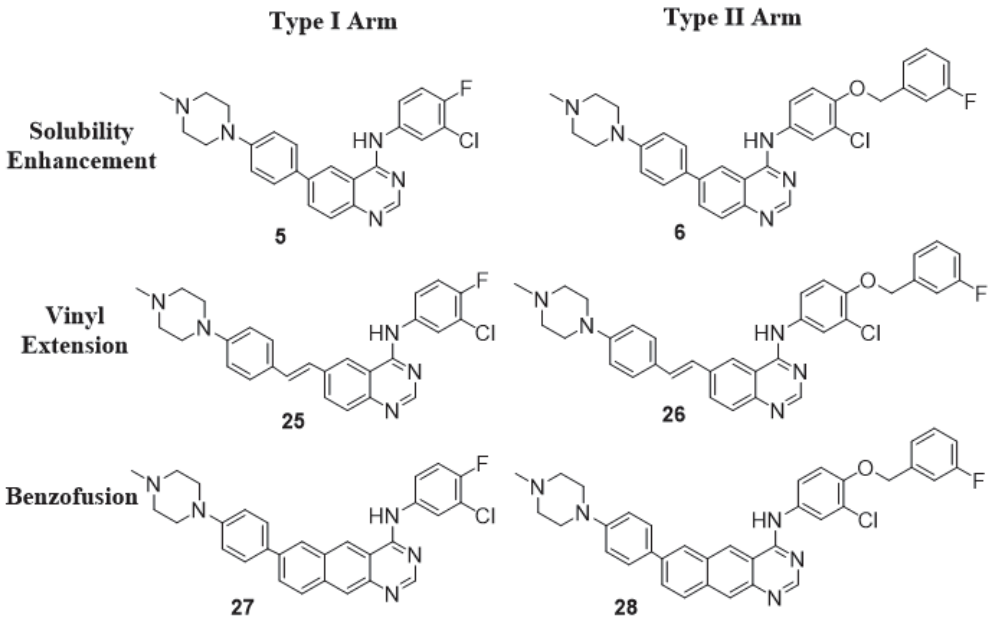

Figure 3.1. Design Strategies. The Type I and Type II pharmacophore arms were adopted at 4-position of core to acquire the binding specificity. The N-methylpiperazine substitution was followed at 6-position of core to increase solubility.

3.2 Results and discussion

3.2.1 Design and synthesis

Firstly, solubility of probes can be optimized by substituting the N-dimethyl-phenyl group to N-methyl-piperazinyl-phenyl group at 6-position of quinazoline and benzo[*g*]quinazoline core. Secondly, the binding affinity and specificity toward activation state can be obtained by adopting Type I and Type II pharmacophore arm structures of EGFR/ERBB2 inhibitors in clinical use, directly to the 4-position of quinazoline and benzo[*g*]quinazoline core (Figure 3.1). Each step of reactions went through appropriate work-up processes, and purified through silica column chromatography, recrystallization and/or distillation. All synthesized compounds were obtained as powder colored in white or yellow. The physicochemical characterization of compounds was achieved through melting point measurement, IR spectra, high resolution mass spectra, ^{1}H NMR and ^{13}C NMR spectra recorded on 500 MHz spectrometer.

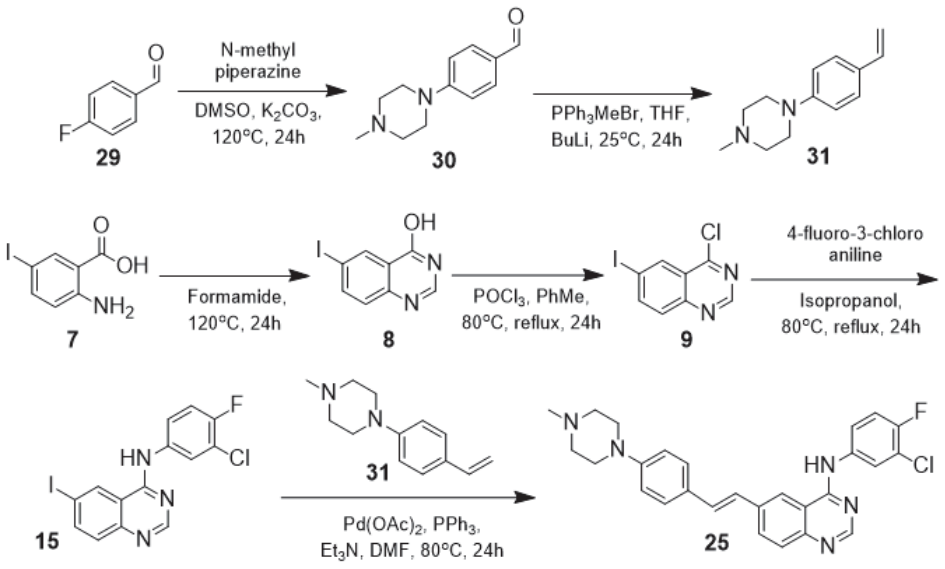

Scheme 3.1. Synthesis of compound **25**.

*Synthesis of (E)-6-(4-(4-Methylpiperazin-1-yl)styryl)-N-(3-chloro-4-fluorophenyl)-quinazolin-4-amine (**25**).*

2.0 grams (5.0 mmol) of N-(3-choloro-4-fluorophenyl)-6-iodo-4-quinazolinamine, 1.0 g (4.94 mmol) of 1-(4-ethenylphenyl)-4-methyl-piperazine, 260 mg of PPh_3, 3.0 mL of Et_3N, and 10.0 mL of DMF were placed in a 50 mL Schlenk flask with a stirrer bar under nitrogen purge. The reaction mixture was degassed for a further 30 min under a slow stream of nitrogen, at which point 200 mg of $Pd(OAc)_2$ was added. The reaction mixture was heated at 80 ºC for 24 h, cooled, poured into 200 mL of H_2O, and extracted with EtOAc (4 × 200 mL). The organic layer was dried with $MgSO_4$, filtered, and then concentrated under reduced pressure. It was purified over silica (100% EtOAc to 100% MeOH) followed by crystallization from 2-propanol and then methanol to afford (*E*)-6-(4-(4-Methylpiperazin-1-yl)styryl)-N-(3-chloro-4-fluorophenyl)-quinazolin-4-amine (100 mg, 4.3 %); mp: 284℃ (dec); IR ν_{max}(cm^{-1}): 3031.69, 2939.58, 2801.54, 1625.48, 1599.21, 1573.11, 1530.11, 1515.72, 1495.09, 1449.37, 1417.03, 1388.92, 1378.44, 1361.96, 1341.11, 1291.71, 1264.83, 1236.6, 1158.73, 1136.3, 1068.98, 883.79, 689.94; ^{1}H NMR(500 MHz, DMSO-d_6): δ: 2.22 (s, 3H) 2.45 (broad s, 4H), 3.20 (broad s, 4H), 6.96 (d, 2H, J = 8.5 Hz), 7.17 (d, 1H, J = 16.5 Hz), 7.38 (d, 1H, J = 16.0 Hz), 7.42 (t, 1H, J = 9.0 Hz), 7.49 (d, 2H, J = 9.0 Hz), 7.71 (d, 1H, J = 8.5 Hz), 7.91 (s, 1H), 8.05 (d, 1H, J = 8.0 Hz), 8.26 (d, 1H, J = 4.5 Hz), 8.55 (s, 1H), 8.76 (s, 1H), 10.49 (s, 1H); ^{13}C NMR (125 MHz, DMSO-d_6), δ: 46.23, 47.908, 54.95, 115.50, 115.76, 117.00-117.17 (d, J_{C-F} = 21.25 Hz), 119.22-119.36 (d, J_{C-F} = 17.5 Hz), 119.67, 122.77-122.83 (d, J_{C-F} = 6.25Hz), 123.95, 124.18, 127.38, 128.02, 128.60, 130.58, 131.75, 136.54, 136.97-136.99 (d, J_{C-F} = 2.5 Hz), 149.35, 151.17, 152.80-154.74 (d, J_{C-}

$_F$ = 242.50 Hz), 154.16, 157.69; HR-ESI (Q-TOF) m/z: calculated for $C_{27}H_{26}ClFN_5^+$ ($M+H^+$): 474.1861, found: 474.1870.

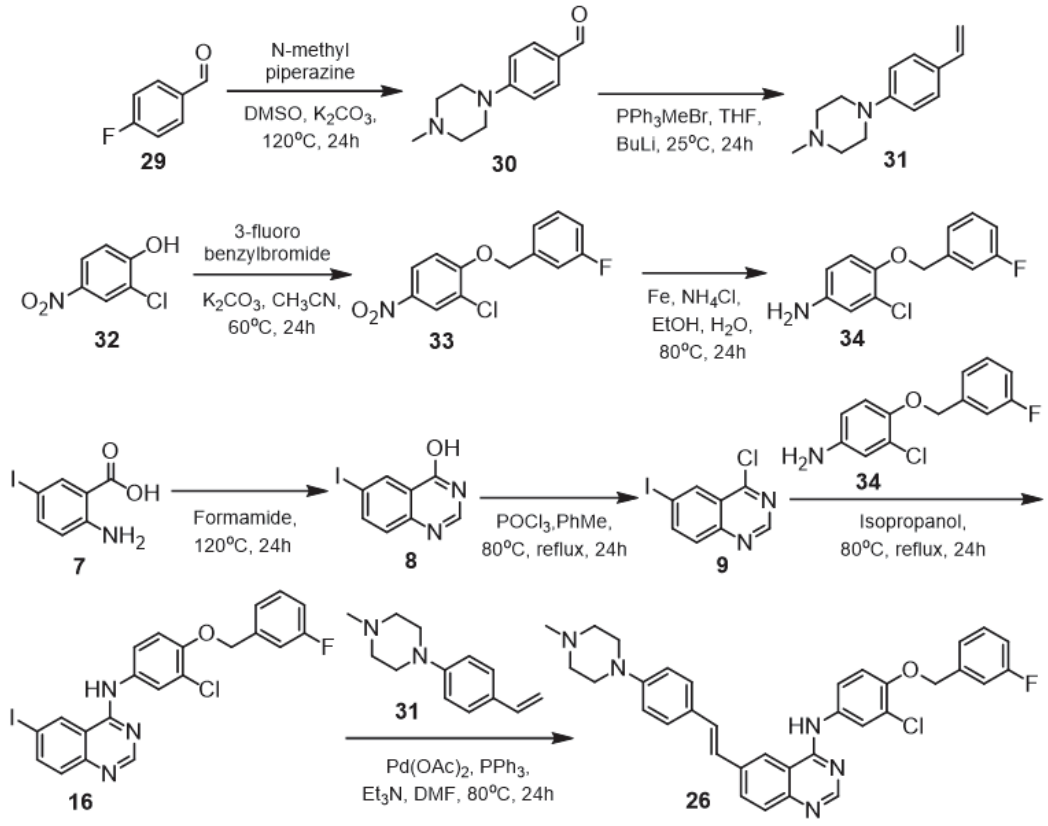

Scheme 3.2. Synthesis of compound **26**.

*Synthesis of (E)-6-(4-(4-Methylpiperazin-1-yl)styryl)-N-(3-chloro-4-((3-fluorophenyl) methoxy)phenyl)-quinazolin-4-amine (**26**).*

1.012 grams (2.0 mmol) of N-(3-chloro-4-((3-fluorophenyl)methoxy)phenyl)-6-iodo-4-quinazolinamine, 0.80 g (3.95 mmol) of 1-(4-ethenylphenyl)-4-methyl-piperazine, 110 mg of PPh_3, 1.5 mL of Et_3N, and 3.5 mL of DMF were placed in a 25 mL Schlenk flask with a stirrer bar under nitrogen purge. The reaction mixture was degassed for a

further 30 min under a slow stream of nitrogen, at which point 100 mg of $Pd(OAc)_2$ was added. The reaction mixture was heated at 80 ºC for 24 h, cooled, poured into 200 mL of H_2O, and extracted with EtOAc (4 × 200 mL). The organic layer was dried with $MgSO_4$, filtered, and concentrated under reduced pressure. It was purified over silica (100% EtOAc to 100% MeOH) followed by crystallization from 2-propanol and then methanol to afford (*E*)-6-(4-(4-Methylpiperazin-1-yl)styryl)-N-(3-chloro-4-((3-fluorophenyl)methoxy)phenyl)-quinazolin-4-amine (130.0 mg, 11.2 %); mp: 248℃ (dec); IR $\nu_{max}(cm^{-1})$: 3081.2, 2941.4, 2799.6, 1930.4, 1603.4, 1593.2, 1567.3, 1517.5, 1500.0, 1454.0, 1418.0, 1381.4, 1357.9, 1334.1, 1286.0, 1239.7, 1201.8, 1138.2, 1036.8, 859.7, 679.6; ^{1}H NMR(500 MHz, DMSO-d_6): δ: 2.22 (s, 3H) 2.45 (broad s, 4H), 3.20 (broad s, 4H), 5.26 (s, 2H), 6.97 (d, 2H, J = 8.5 Hz), 7.15-7.20 (m, 4H), 7.45 (d, 1H, J = 8.0 Hz), 7.49 (d, 2H, J = 8.5 Hz), 7.73 (d, 1H, J = 9.0 Hz), 7.75 (dd, 1H, J = 9.0, 2.0 Hz), 8.05 (s, 1H), 8.06 (d, 1H, J = 9.0 Hz), 8.54 (s, 1H), 8.58 (s, 1H), 9.78 (s, 1H); ^{13}C NMR (125 MHz, DMSO-d_6), δ: 46.24, 47.92, 54.96, 69.77, 114.44-114.62 (d, J_{C-F} = 22.50 Hz), 114.73, 115.11-115.28 (d, J_{C-F} = 21.25 Hz), 115.54, 115.76, 119.65, 121.44, 122.63, 123.82-123.84 (d, J_{C-F} = 2.5 Hz), 124.27, 124.44, 127.44, 128.01, 128.54, 130.43, 131.01-131.10 (d, J_{C-F} = 8.75 Hz), 131.67, 133.65, 136.38, 140.09-140.15 (d, J_{C-F} = 7.50 Hz), 149.30, 150.06, 151.17, 154.39, 157.81, 161.69-163.62 (d, J_{C-F} = 241.25 Hz); HR-ESI (Q-TOF) m/z: calculated for $C_{34}H_{32}ClFN_sO^+$ ($M+H^+$): 580.2279, found: 580.2295.

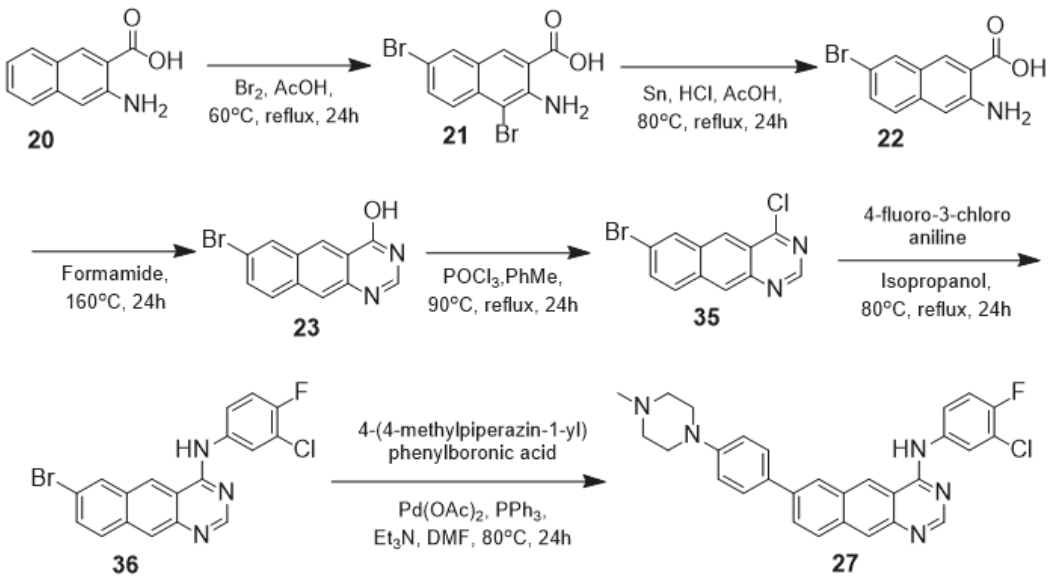

Scheme 3.3. Synthesis of compound **27**.

*Synthesis of 7-bromo-N-(3-chloro-4-fluorophenyl)-benzo[g]quinazolin-4-amine (**36**).*

4.5 g (30.9 mmol) of 3-chloro-4-fluoro-aniline, and 2-propanol were added directly in that same round bottom flask containing dark brown crude solid. Then the mixture was vigorously stirred and heated at 80 ºC, overnight with a condenser. After 24 hours, it was cooled to room temperature, concentrated under reduced pressure, 200 mL of 1M KOH solution was added and stirred for 20 min, then yellow precipitate was isolated by filtering. Dried precipitate was added into 200 mL of EtOAc, stirred for 10 min, filtered to separate solid impurities and eluted solution was concentrated. It was purified over silica (100% EtOAc) followed by crystallization from 2-propanol and then methanol. Resulted solid was added in 2 mL of dichloromethane then sonicated for 10 mins, 20 mL of hexane was added. Precipitate was filtered to afford yellow powder of 7-bromo-N-(3-chloro-4-fluorophenyl)-benzo[g]quinazolin-4-amine (480.0 mg, 5.47%); mp: 256℃ (dec); IR ν_{max}(cm^{-1}): 3434.7, 3027.8, 2970.5, 1923.2, 1682.8,

1605.9, 1592.0, 1569.9, 1557.8, 1528.7, 1492.3, 1459.7, 1403.5, 1358.5, 1304.3, 1289.3, 1279.9, 1253.02, 1228.0, 1201.8, 1147.2, 1054.3, 879.8, 691.3; ^{1}H NMR(500 MHz, DMSO-d_6): δ: 1.68(s, 1H), 7.39 (t, 1H, J = 9.0 Hz), 7.69 (d, 1H, , J = 9.0 Hz), 7.74 (s, 1H), 8.05 (d, 1H, J = 9.0 Hz), 8.14 (s, 1H), 8.27 (s, 1H), 8.32 (s, 1H), 8.44 (s, 1H), 9.18 (s, 1H); ^{13}C NMR (125 MHz, DMSO-d_6 + TFA), δ: 113.45, 117.44, 117.59-117.61 (d, J_{C-F} = 7.5 Hz), 119.88-120.03 (d, J_{C-F} = 18.75 Hz), 121.75, 125.69, 125.81-125.87 (d, J_{C-F} = 7.5 Hz), 127.26, 130.45, 131.06, 132.62, 133.78, 133.85, 133.95-133.97 (d, J_{C-F} = 2.5 Hz), 134.70, 152.65, 155.11-157.08 (d, J_{C-F} = 246.25 Hz), 160.96; HR-ESI (Q-TOF) m/z: calculated for $C_{18}H_{11}BrClFN_3^+$ ($M+H^+$): 401.9809, found: 401.9815.

*Synthesis of 7-(4-(Dimethyl-amino)phenyl)-N-(3-chloro-4-fluorophenyl)-benzo[g]quinazolin-4-amine (**27**).*

730 milligrams (1.8 mmol) of 7-bromo-N-(3-chloro-4-fluorophenyl)-benzo[g]quinazolin-4-amine, 660 mg (3.0 mmol) of 4-(4-methylpiperazin-1-yl)phenylboronic acid, 110 mg of PPh_3, 1.5 mL of Et_3N, and 4.0 mL of DMF were placed in a 25 mL Schlenk flask with a stirrer bar under nitrogen purge. The reaction mixture was degassed for a further 30 min under a slow stream of nitrogen, at which point 100 mg of $Pd(OAc)_2$ was added. The reaction mixture was heated at 80 ºC for 24 h, cooled, poured into 200 mL of H_2O, and extracted with EtOAc (4 × 200 mL). The organic layer was dried with $MgSO_4$, filtered, and then concentrated under reduced pressure. It was purified over silica (100% EtOAc to 100% MeOH) followed by crystallization from 2-propanol and then methanol mixed with ethylacetate. Resulted

solid was added in 2 mL of dichloromethane then sonicated for 10 mins, 20 mL of hexane was added. Precipitate was filtered to afford yellow powder of 7-(4-(Dimethyl-amino)phenyl)-N-(3-chloro-4-fluorophenyl)-benzo[g]quinazolin-4-amine (30 mg, 3.4 %); mp: 262℃ (dec); IR ν_{max}(cm^{-1}): 3043.3, 2939.5, 2814.3, 1923.6, 1605.6, 1572.6, 1541.8, 1521.8, 1496.5, 1412.3, 1293.3, 1236.2, 1202.9, 1139.3, 1058.9, 1008.2, 880.3, 691.0; ^{1}H NMR(500 MHz, DMSO-d_6): δ: 2.23 (s, 1H), 2.46 (t, 4H, J = 4.5 Hz), 3.21 (t, 4H, J = 4.5 Hz), 7.07 (d, 2H, J = 8.5 Hz), 7.45 (t, 1H, , J = 9.0 Hz), 7.72 (d, 2H, J = 8.5 Hz), 7.86 (s, 1H), 7.96 (d, 1H, J = 8.0 Hz), 8.16 (d, 1H, J = 9.0 Hz), 8.23 (s, 1H), 8.26 (s, 1H), 8.34 (s, 1H), 8.54 (s, 1H), 9.20 (s, 1H), 10.35 (broad s, 1H); ^{13}C NMR (125 MHz, DMSO-d_6 + TFA), δ: 42.54, 45.56, 52.57, 113.30, 116.64, 117.45, 117.63, 119.76-119.91 (d, J_{C-F} = 21.25 Hz), 124.68, 125.58-125.63 (d, J_{C-F} = 6.25 Hz), 126.20, 126.97, 128.26, 128.94, 129.97, 130.11, 132.53, 134.20, 134.50, 135.25, 139.06, 149.91, 152.22, 154.84-156.80 (d, J_{C-F} = 245.00 Hz), 160.78; HR-ESI (Q-TOF) m/z: calculated for $C_{29}H_{26}ClFN_5^+$ ($M+H^+$): 498.1861, found: 498.1882.

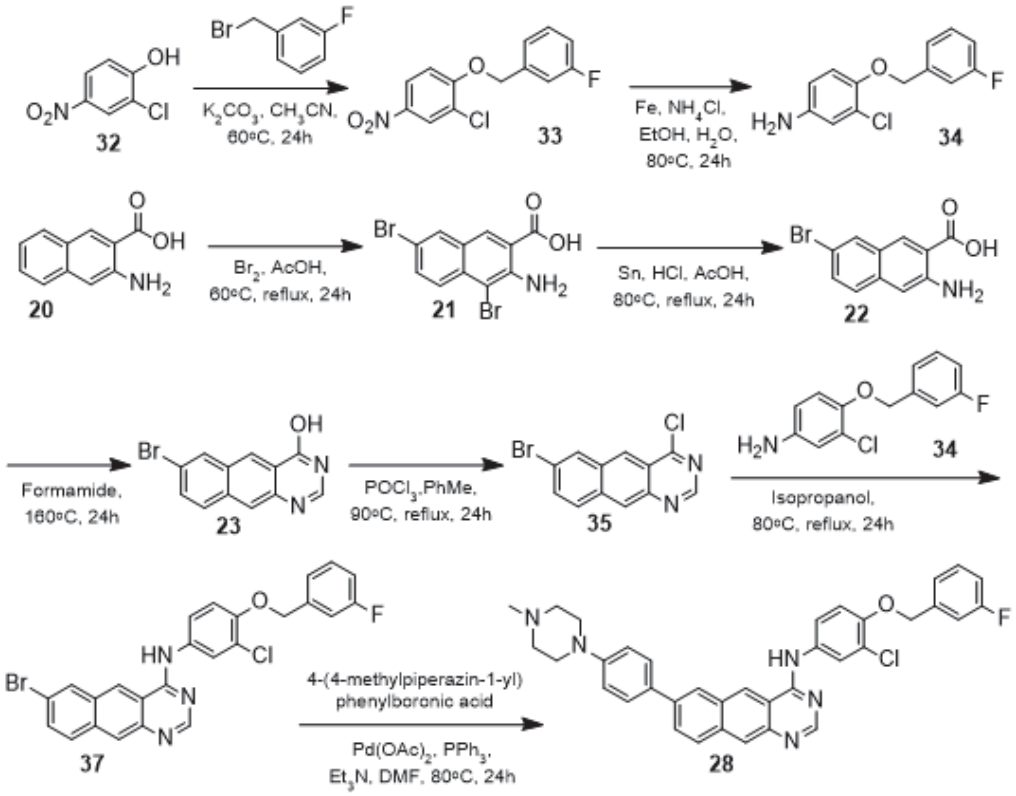

Scheme 3.4. Synthesis of compound **28**.

*Synthesis of 7-bromo-N-(3-chloro-4-((3-fluorophenyl)methoxy)phenyl)-benzo[g]quinazolin-4-amine (**37**).*

11.0 g (43.8 mmol) of 3-chloro-4-[(3-fluorophenyl)methoxy]-benzenamine,, and 2-propanol were added directly in that same round bottom flask containing dark brown crude solid. Then the mixture was vigorously stirred and heated at 80 ^{o}C, overnight with a condenser. After 24 hours, it was cooled to room temperature, concentrated under reduced pressure, 200 mL of 1M KOH solution was added and stirred for 20 min, yellow precipitate was isolated by filtering. Dried precipitate was added into 200 mL of EtOAc, stirred for 10 min, filtered to separate solid impurities and eluted solution was concentrated. It was purified over silica (100% EtOAc) followed by crystallization

from 2-propanol and then methanol/ethylacetate mixed solvents to afford yellow powder of 7-bromo-N-(3-chloro-4-((3-fluorophenyl)methoxy)phenyl)-benzo[g]quinazolin-4-amine (1.50 g, 13.5 %); mp: 230℃ (dec); IR ν_{max}(cm^{-1}):3411.0, 3032.8, 2864.0, 1832.8, 1751.6, 1589.7, 1560.0, 1529.4, 1499.4, 1458.5, 1415.0, 1380.0, 1357.9, 1299.0, 1276.3, 1201.8, 1139.7, 1059.2, 877.6, 692.2; ^{1}H NMR(500 MHz, DMSO-d_6): δ: 5.245 (s, 1H), 7.16 (t, 1H, , J = 8.0 Hz), 7.26 (d, 1H, J = 9.0 Hz), 7.30-7.34 (m, 2H) 7.44 (dd, 1H, J = 14.0, 8.0 Hz), 7.69 (d, 1H, , J = 9.0 Hz), 7.78 (d, 1H, , J = 9.0 Hz), 8.06 (d, 1H, , J = 8.5 Hz), 8.11 (s, 1H), 8.22 (s, 1H), 8.38 (s, 1H), 8.57 (s, 1H), 9.06 (s, 1H), 10.11 (s, 1H); ^{13}C NMR (125 MHz, DMSO-d_6), δ: 69.73, 114.39, 114.58, 115.08-115.24 (d, J_{C-F} = 20.00 Hz), 116.08, 119.83, 121.42, 122.74, 122.87, 123.77, 124.56, 125.78-125.80 (d, J_{C-F} = 2.5 Hz), 130.56, 130.98-131.04 (d, J_{C-F} = 7.5 Hz), 131.30, 131.90, 133.36, 133.99, 140.03-140.08 (d, J_{C-F} = 6.25 Hz), 145.67, 150.23, 154.83, 158.33, 161.67-163.60 (d, J_{C-F} = 241.25 Hz); HR-ESI (Q-TOF) m/z: calculated for $C_{25}H_{17}BrClFN_3O^+$ ($M+H^+$): 508.0228, found: 508.0236.

*Synthesis 7-(4-(4-Methylpiperazin-1-yl)phenyl)-N-(3-chloro-4-((3-fluorophenyl)methoxy) phenyl)-benzo[g]quinazolin-4-amine (**28**).*

800 milligrams (1.5 mmol) of 7-bromo-N-(3-chloro-4-((3-fluorophenyl)methoxy)phenyl)-benzo[g]quinazolin-4-amine, 990 mg (4.0 mmol) of 4-(4-methylpiperazin-1-yl)phenylboronic acid, 110 mg of PPh_3, 1.5 mL of Et_3N, and 5.0 mL of DMF were placed in a 25 mL Schlenk flask with a stirrer bar under nitrogen purge. The reaction mixture was degassed for a further 30 min under a slow stream of nitrogen, at which point 100 mg of $Pd(OAc)_2$ was added. The reaction mixture was

heated at 80 ºC for 24 h, cooled, poured into 200 mL of H_2O, and extracted with EtOAc (4 × 200 mL). The organic layer was dried with $MgSO_4$, filtered, and concentrated under reduced pressure. It was purified over silica (100% EtOAc to 100% MeOH) followed by crystallization from 2-propanol, then methanol with ethylacetate to afford the yellow powder of 7-(4-(4-Methylpiperazin-1-yl)phenyl)-N-(3-chloro-4-((3-fluorophenyl)methoxy)phenyl)-benzo[g]quinazolin-4-amine (75.0 mg, 8.3%); mp: 258℃ (dec); IR ν_{max}(cm^{-1}): 3074.6, 2940.3, 2796.5, 1938.2, 1605.9, 1552,4, 1498.6, 1475.6, 1454.4, 1435.0, 1411.8, 1379.8, 1368.2, 1328.1, 1283.1, 1264.3, 1238.4, 1209.8, 1137.2, 1062.7, 1035.8, 879.6, 679.7; ^{1}H NMR(500 MHz, DMSO-d_6): δ: 2.24 (s, 1H), 2.47 (broad s, 4H), 3.24 (broad s, 4H), 5.27 (s, 2H), 7.09 (d, 1H, J = 7.5 Hz), 7.17 (t, 1H, , J = 8.5 Hz), 7.30-7.35 (m, 3H), 7.46 (dd, 1H, J = 13.5, 6.0 Hz), 7.74 (d, 2H, J = 7.5 Hz), 7.83 (s, 1H), 7.98 (d, 1H, J = 9.0 Hz), 8.18 (d, 2H, J = 9.0 Hz), 8.23 (s, 1H), 8.36 (s, 1H), 8.57 (s, 1H), 9.20 (s, 1H), 10.14 (s, 1H); ^{13}C NMR (125 MHz, DMSO-d_6, TFA), δ: 46.25, 48.07, 54.99, 69.81, 114.43-114.60 (d, J_{C-F} = 21.25 Hz), 114.75, 115.10-115.27 (d, J_{C-F} = 21.25 Hz), 115.77, 116.00, 121.47, 122.61, 123.46, 123.81-123.83 (d, J_{C-F} = 2.5 Hz), 124.15, 124.42, 125.11, 127.79, 127.92, 128.89, 129.63, 131.02-131.09 (d, J_{C-F} = 8.75 Hz), 131.86, 133.70, 134.65, 137.87, 140.09-140.15 (d, J_{C-F} = 7.5 Hz), 145.28, 150.15, 151.13, 154.27, 158.39, 161.70-163.63 (d, J_{C-F} = 241.25 Hz); HR-ESI (Q-TOF) m/z: calculated for $C_{36}H_{32}ClFN_5O^+$ ($M+H^+$): 604.2279, found: 604.2296.

3.2.2 Optical spectroscopy

The optical properties of probes **25-28** were qualitatively observed by sight as in chloroform ($E_T(30)$ = 39.1 kcal/mol)[39] solutions, and compared with quinazoline probes **5** and **6**.

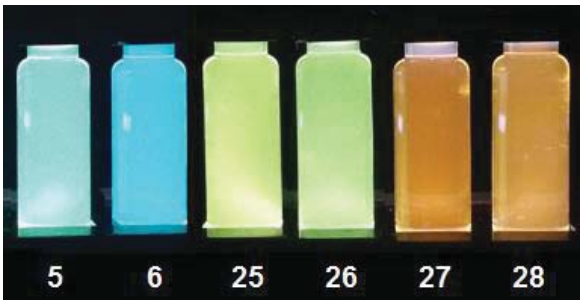

Figure 3.2. Chloroform solutions of compounds in 5 μM under UV illumination at 354 nm.

The quinazoline probes (**5, 6**) appear bright with emissions ranging from greenish blue Figure 3.2, while vinyl extension (**25**, **26**) induced slight bathochromic shift with yellow emission. Moreover, the benzo-fusion of quinazoline core (**27**, **28**) exhibited bright orange emission under UV illumination. To investigate their optical properties quantitatively, UV-Vis and fluorescence spectra of compounds were measured in chloroform (Figure 3.3). UV-Vis absorption spectra were obtained on a Perkin-Elmer Lamda 35 UV-Vis spectrometer using chromophore solutions of 10 μM with 1 cm path length. Fluorescence spectra were measured on a Perkin-Elmer LS55 Fluorometer using probe concentrations of 1 μM. For determination of the Φ_{em}, solutions were prepared to an optical density of less than 0.05 in order to minimized inner filter effects. Perylene in cyclohexane was used as a reference for quantum yields.[40]

Table 3.1. Photophysical parameters of **25-28** in solution.

Solvent / 25	PhMe	$CHCl_3$	MeCN	MeOH	IPA	BuOH	OcOH	PBS
$\lambda_{max, abs}$ (nm)	367	366	362	356	362	360	362	357
ε ($M^{-1}cm^{-1}$)	31800	35000	34600	38100	36700	34400	35500	24200
$\lambda_{max, FL}$ (nm)	450	489	538	511	525	515	507	465
Φ_{FL}[a]	0.52	0.27	0.09	0.05	0.07	0.07	0.22	0.01
Solvent / 26	PhMe	$CHCl_3$	MeCN	MeOH	IPA	BuOH	OcOH	PBS
$\lambda_{max, abs}$ (nm)	370	369	362	357	364	361	365	355
ε ($M^{-1}cm^{-1}$)	32000	36200	34000	37500	36900	34200	37200	25600
$\lambda_{max, FL}$ (nm)	460	497	526	515	518	515	489	505
Φ_{FL}[a]	0.43	0.17	0.12	0.04	0.07	0.08	0.17	0.01
Solvent / 27	PhMe	$CHCl_3$	MeCN	MeOH	IPA	BuOH	OcOH	PBS
$\lambda_{max, abs}$	324	321	317	314	321	321	322	326
(nm)	407	406	404	404	405	406	408	382
ε	31000	32000	34600	35000	33900	31000	33300	22800
($M^{-1}cm^{-1}$)	10400	9900	10200	9700	10000	9100	9900	8400
$\lambda_{max, FL}$ (nm)	504	522	553	595	620	628	545	700
Φ_{FL}[a]	0.56	0.27	0.01	0.02	0.02	0.02	0.07	0.007
Solvent / 28	PhMe	$CHCl_3$	MeCN	MeOH	IPA	BuOH	OcOH	PBS
$\lambda_{max, abs}$	326	326	324	317	323	324	325	327
(nm)	411	410	408	408	409	410	412	430
ε	35900	35800	38000	37500	36200	36100	36100	23100
($M^{-1}cm^{-1}$)	15300	13400	14200	13400	13700	13700	13800	11400
$\lambda_{max, FL}$ (nm)	495	547	650	590	609	544	525	700
Φ_{FL}[a]	0.22	0.11	0.01	0.01	0.02	0.02	0.07	0.007

[a] ± 10%

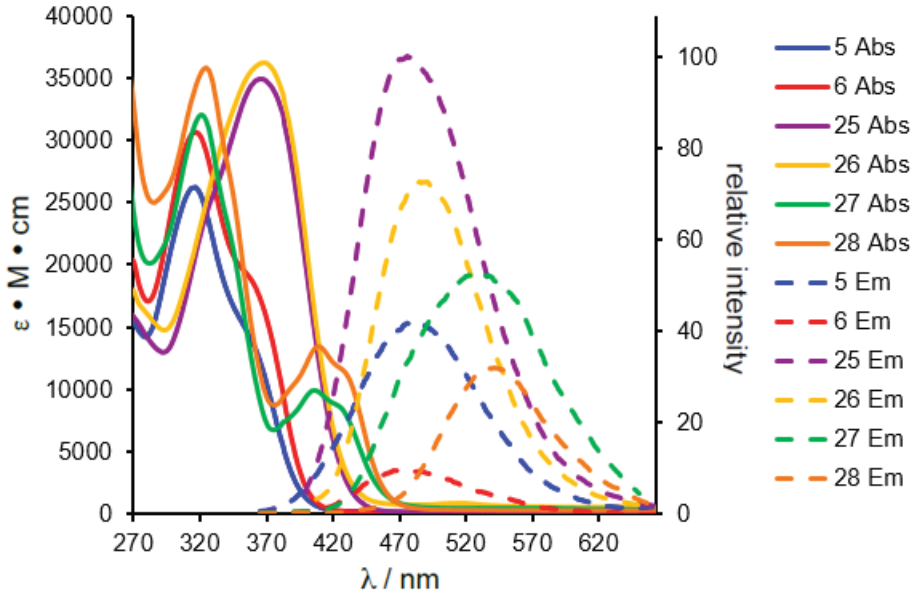

Figure 3.3. Absorption (solid lines) and emission (dashed lines) spectra of compounds in $CHCl_3$. Emission intensities are given relative to **25**, which has the highest quantum yield.

Although the vinyl extension of quinazoline core (**25**, **26**) effectively induced bathochromic from reference compounds (**5**, **6**), the benzo-fusion of quinazoline exhibited remarkable degree of bathochromic shift on emission maximum in chloroform system. The emission spectra of 6 compounds (**5**, **6**, **25**, **26**, **27**, **28**) in various solvent systems are shown in Figure 3.3. All the probes exhibit sensitivity on polarity of environment, which makes them as turn-on probes by turning on at the binding event at hydrophobic binding pocket, and turning off in aqueous surrounding outside of binding fold.

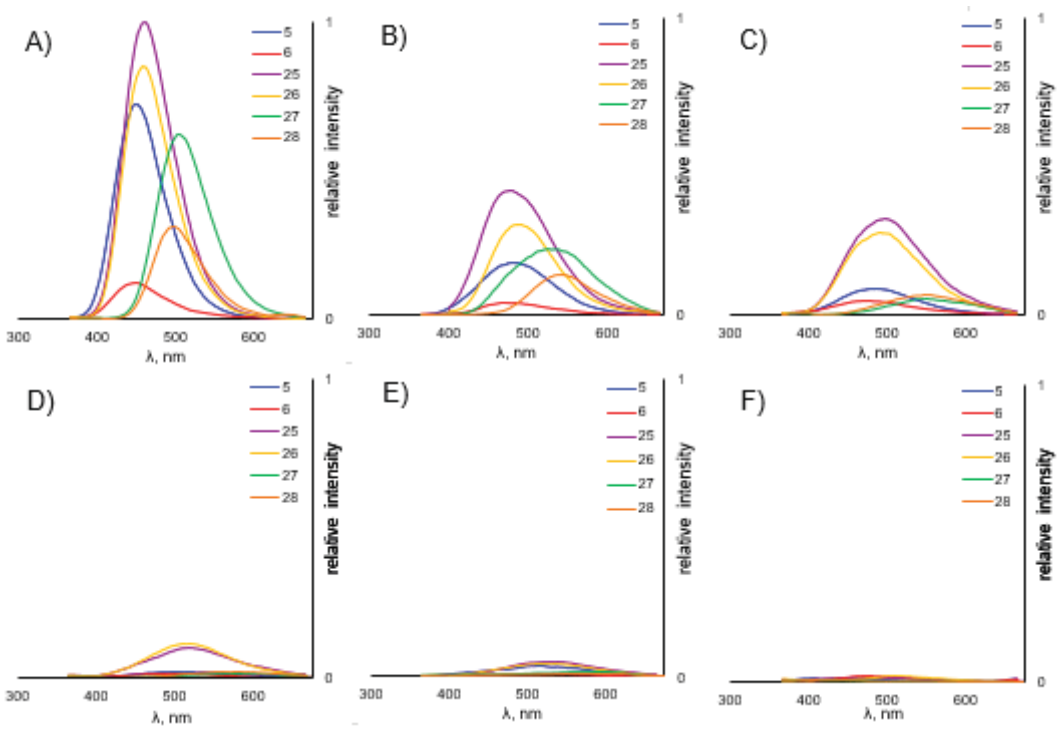

Figure 3.4. Emission spectra of presented compounds in A) toluene, B) chloroform, C) octanol, D) isopropanol, E) methanol, F) PBS.

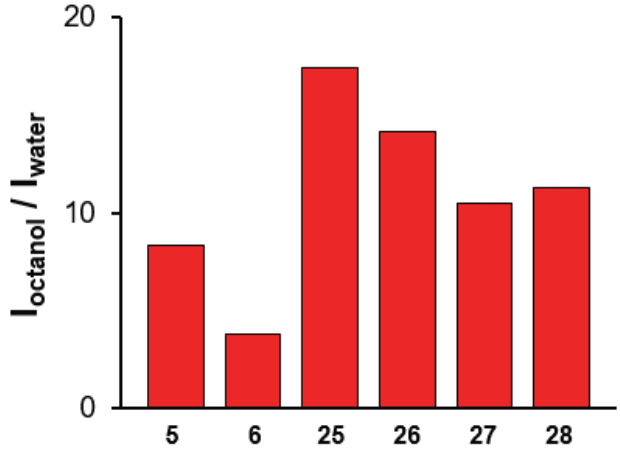

Figure 3.5. Emission intensities of 6 compounds obtained in octanol and water present fluorescence turn ON/OFF ratios.

The chemico-physical properties of **25-28** were calculated through SwissADME to obtain an insight of molecules cellular distribution and pharmacokinetics.[42-44] Turn-on ratio of compounds in between water ($E_T(30)$ = 63.1 kcal/mol, η = 0.89 mPa•s) and octanol ($E_T(30)$ = 48.3 kcal/mol, η = 7.24 mPa•s)[39] are presented by the ratios of emission intensities obtained in octanol and water are shown in Figure 3.4.

Table. 3.2. Chemico-physical properties of **25-28**.

Compounds / Properties	25	26	27	28
Molar refractivity	145.68	176.66	153.25	184.23
Topological polar surface area	44.29 Å	53.52 Å	44.29 Å	53.52 Å
log P $_{o/w}$	4.89	5.44	5.17	5.70
log K $_p$	-4.68 cm/s	-5.44 cm/s	-4.40 cm/s	-4.01 cm/s
BBB Permeant	Yes	No	No	No
GI absorption	High	Low	High	Low

3.2.3 Inhibition study

We evaluated all of 4 probes as inhibitors of ERBB2 phosphorylation in MCF7 cells using 6 probe concentrations, 0, 39, 156, 625, 2500 and 10000 nM. MCF7 cells are a well-established model system for the ligand induced activation of ERBB2-ERBB3 hetero-complexes by ligand of the neuregulin family (NRGβ1 in this case). In evaluation, MCF cells were seeded with equal quantity (200 thousand/well) in six-well plates. After 48 hours, cells were pre-treated with small molecule inhibitors of various

concentrations for 30 minutes before induction by neuregulin (NRGβ1, 30 nM, 30 minutes). Cell lysates were generated immediately by SDS lysis. Equal aliquots were subjected to SDS-PAGE and Western blot analysis. ERBB2 phosphorylation was evaluated for Tyr1139 located close to the extreme cytoplasmic C-terminus of the receptor (validated by pan-TyrP detection (4G10)). The signal obtained for pTyr1139 relative to the ERBB2 receptor levels was determined as the relative receptor phosphorylation.

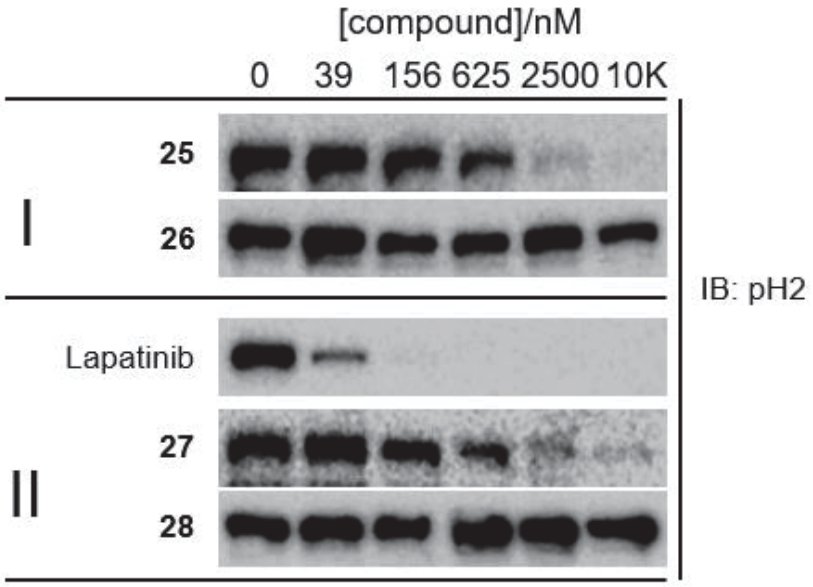

Figure 3.6. Inhibition of NRGβ1-induced ERBB2 tyrosine phosphorylation in MCF7 cells at 6 concentrations by compounds.

The western blot result suggests that elongating the conjugation length at 6-position of quinazoline has negative effect on binding to ATP binding pocket of ERBB2 receptor tyrosine kinase. The compound **25** exhibits Ki around 700 nM, and the comparison of **5**'s Ki of 71 nM suggests that the addition of one vinyl unit at 6-position lowers the binding affinity by 10 folds.

Furthermore, the core expansion through benzo-fusion of quinazoline dramatically reduces binding affinity to no inhibition at the test setting. Those benzo-fusion compounds **26** and **28** were tested again with milder ligand induced activation settings on MCF7 cells at NRG-1β in 0.5 nM, 30 minutes of room temperature incubation.

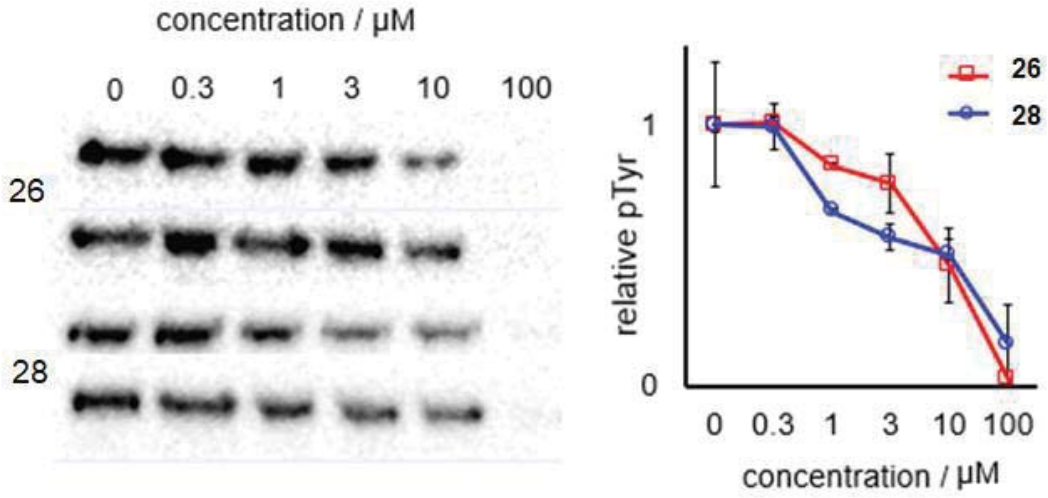

Figure 3.7. ERBB2 phosphorylation inhibition measurement of **26** and **28** via mild ligand stimulation assay at room temperature with MCF7 cells in duplicates experiment.

Although in mild ligand induction condition, compounds **26** and **28** exhibited insignificant inhibition ability for ERBB2 phosphorylation. It may due to the expanded aromatic core size hindering their binding at ATP binding pocket.

3.3 Conclusion

To develop turn-on fluorescent probes having enhanced optical property than quinazoline class probes (5, 6), we have generated probes with vinyl extension as

well as benzo-fusion (25-28) by employing the N-methylpiperazine substituent and pharmacophore arm on extended aromatic framework. Those structural modification strategies resulted in moderate enhancement on binding affinity toward ATP binding pocket of ERBB2 for the vinyl extended compounds (25, 27), while insignificant effects on benzo-fusion compounds (26, 28). It suggests that the aromatic frame extension of quinazoline may introduce unfavored interaction with the portal area of ATP binding pocket resulting in reduced binding affinity. Hence, the core modification within the adenosine-size would be ideal to induce bathochromic shift than extension.

Chapter 4

SYNTHESIS AND PHOTOPHYSICAL PROPERTIES OF A CYANOQUINOLINE ERBB2 PROBE FOR PROFILING KINASE INHIBITOR RESPONSE

4.1 Overview

Development of small molecular kinase inhibitors and monoclonal antibodies have constructed the modern chemotherapy regime for various cancers. However, the heterogeneity of cancer cells obstructs rapid identification. Furthermore, incidence of mutation and drug resistance throughout the treatment period challenges the receptor targeted chemotherapy.[63-65] The prediction of certain drug efficiencies can be achieved through the genomic analysis as well as functional phenotype assays. On the aspect of functional receptor analysis, we developed fluorescent kinase probes, the quinazoline class turn-on probes, targeting the ATP-binding pocket of EGFR/ERBB family of receptor tyrosine kinases. The quinazoline-class Type I probe, QA1 (**5**) and quinazoline-class Type II probe, QA2 (**6**) (Figure 4.1) were capable of selectively staining and differentiating HER2(+) cells from HER2(-) cells.[25] While ERBB2/HER2 receptor activation dynamics could be reported in real time at the single cell level, spectral overlap with the moderate inherent emission of quinazoline-class inhibitors in clinical use[66], such as lapatinib[67] or gefitinib,[68] prevented the use of quinazoline class probes for observing the effect of these drugs. To utilize kinase fluorescent probes in observation of signaling pathways with established inhibitors, the spectral overlap should be minimized. In this context, we developed the cyano-quinoline class kinase probes, which exhibit significantly red-shifted fluorescence compared to quinazoline class probes.

The optical properties of CQ1 (**39**) make it as an attractive candidate for both detecting ERBB2-overexpressing cells as well as monitoring the drug response.

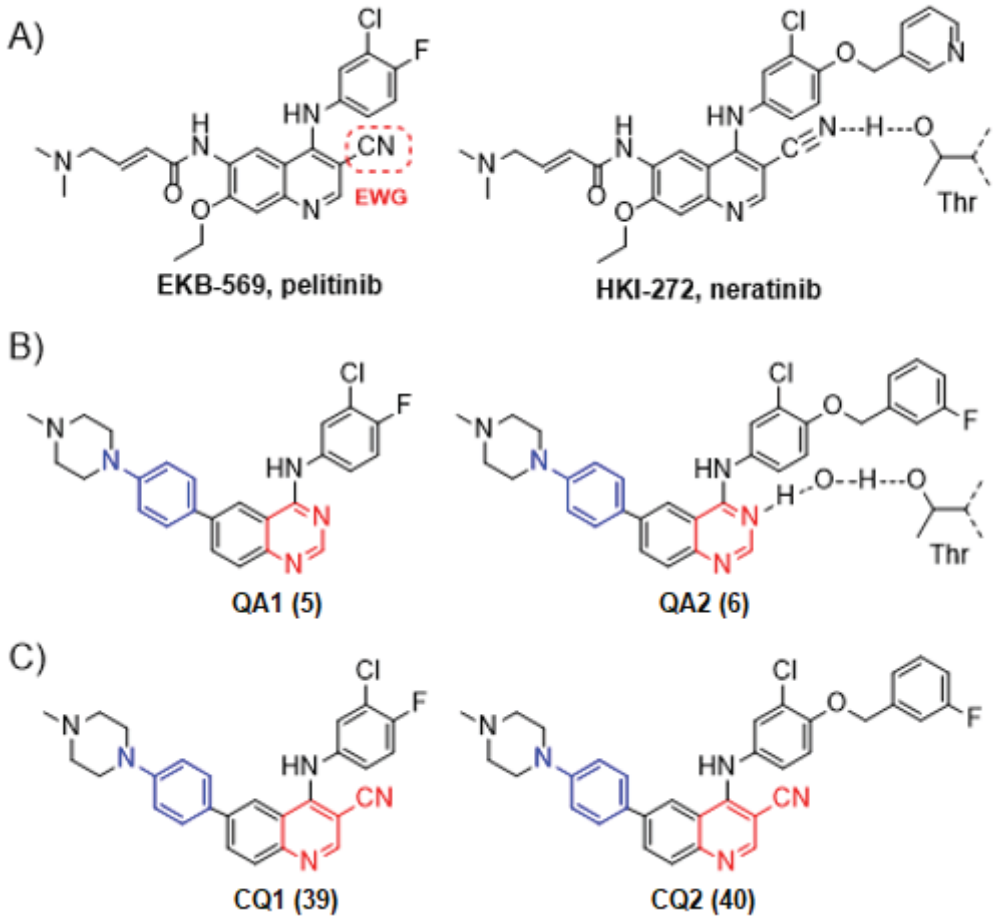

Figure 4.1. A) Examples of Type I, pelitinib, and Type II, neratinib, cyano-quinolines under investigation as EGFR/ERBB inhibitors; the cyano moiety interacts with a threonine residue in the ATP binding pocket, replacing a water bridge found for quinazoline inhibitors.[69,70] B) Fluorescent quinazoline probes developed in our lab. C) Cyano-quinoline probes with modified donor-π-acceptor investigated in this study.

4.2 Results and discussion

4.2.1 Design and synthesis

Quinazoline-based inhibitors (erlotinib, gefitinib, and lapatinib) target the ATP binding pocket of the EGFR/ERBB family.[33,71]

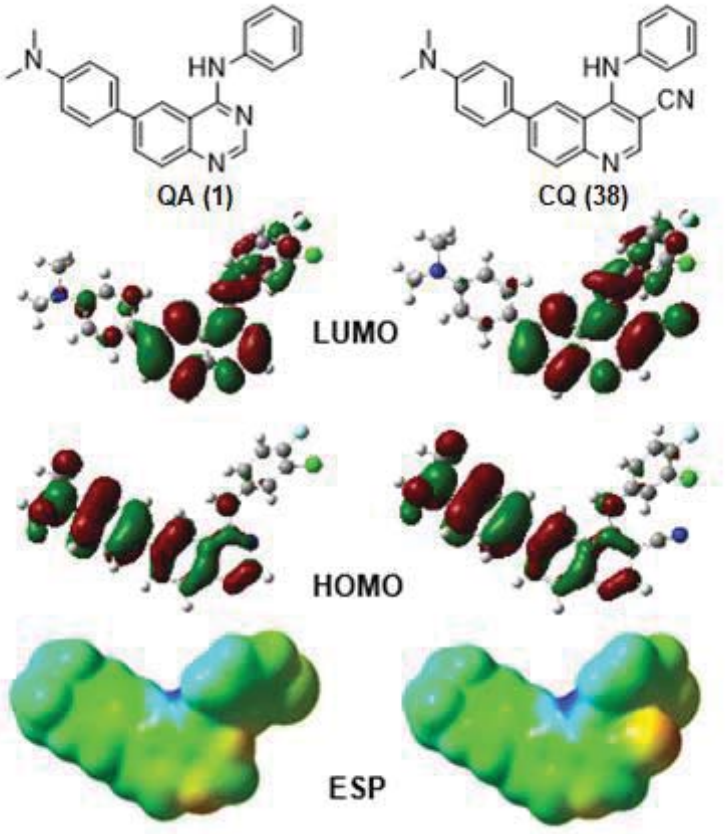

Figure 4.2. Chemical structures, frontier molecular orbitals and electrostatic potential (ESP) maps of model compounds used to compare the electronic properties of kinase probes built on the quinazoline, QA (**1**) and cyano-quinoline, CQ (**38**) heterocyclic cores. While the HOMOs map with nearly identical distributions, the LUMO shows slightly more polarization on CQ (**38**), a result of the electron-withdrawing nature of the cyano group, which also appears electronegative in the ESP surface.

However, their inherent optical properties as fluorescent probes are less than ideal, requiring UV excitation and exhibiting low quantum yields. Especially, their emission spectra overlap with quinazoline probes at clinical relevant concentration (1-10 μM). Thus, next generation probes were needed to be generated with significantly red-shifted emission spectra required to image the dynamics of EGFR/ERBB receptor tyrosine kinase family in response to these quinazoline class inhibitors.

The pelitinib and neratinib with 3-cyanoquinoline pharmacophores have also been developed as inhibitors of EGFR/ERBB receptor tyrosine kinases.[65,66] Their binding mode differs slightly with the quinazoline class inhibitors by the cyano-group replacing a bridging water molecule, which interacts with a threonine residue via a hydrogen bond (Figure 4.1). The cyano-quinoline core with stronger electron withdrawing ability could generate red-shifted excitation and emission spectra than the quinazoline core in donor-acceptor system by lowering the energy of the S_1 state. TD-DFT calculations on truncated model compounds QA (**1**) and CQ (**38**) (Figure 4.2) predicted an S_1 state that was only lowered by 0.3 eV, corresponding to a ~ 20 nm shift in the absorption spectra. However, mapping of the frontier molecular orbitals, as well as the dipoles of the molecules, 11 D for QA (**1**) versus 13 D for CQ (**38**) suggested that the excited state of the cyano-quinoline probes should be more polarized than that of the quinazoline probes. This can be seen in a small, but non-trivial shift in orbital density in the frontier molecular orbitals. While the HOMOs of QA (**1**) and CQ (**38**) are virtually identical, the LUMO of CQ (**38**) showed density shifted away from the dimethyl-amino group and towards the cyano group, which could contribute to thermal relaxation in the excited state and an increased Stoke shift.

The synthesis of CQ1 **(39)** and CQ2 **(40)** proceeded from 6-bromo-4-chloro-3-quinolinecarbonitrile (**44**) which was generated according to reference 79 (Scheme 4.1) and confirmed by ^{1}H and ^{13}C NMR spectroscopy as well as FT-IR and HRMS. The two pharmacophore arms, or phenyl moiety in the case of the model compound, CQ **(38)**, were installed via nucleophilic aromatic substitution of the chlorine at the 4-position, followed by the electron-donating anilino arm, which coupled under Suzuki conditions to the 6-position.

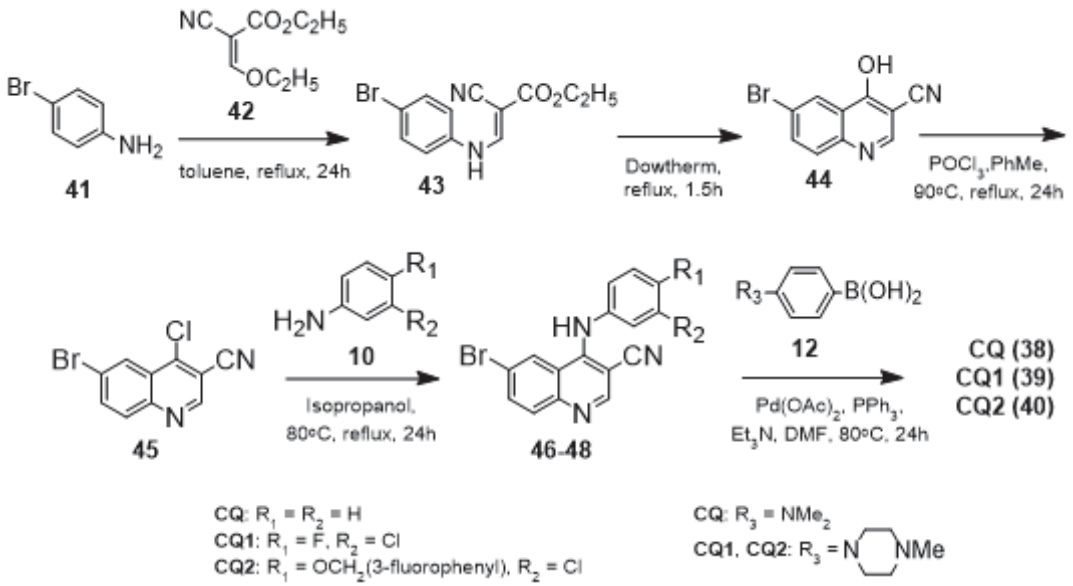

Scheme 4.1. Synthesis of fluorescent cyano-quinoline probes.

*Synthesis of 6-bromo-N-(phenyl)-quinoline-3-carbnitrile-4-amine (**46**).*

2.5 grams of **45** (9.4 mmol), 1.5 g (16.1 mmol) of aniline, and 2-propanol were added, vigorously stirred and heated at 80 ºC, overnight with a condenser. After 24 hours, it was cooled to room temperature, concentrated under reduced pressure, 100 mL of 1M

KOH solution was added and stirred for 20 min, 300 mL of EtOAc was added, then organic solution was extracted through separation funnel and concentrated. It was purified over silica (100% DCM to 100% EtOAc) followed by crystallization from methanol to afford yellow powder of **43** (1.363g, 42.1 %); mp: 216-218℃ ; IR ν_{max}(cm^{-1}): 3279.7, 3202.7, 3123.3, 3053.9, 2226.2, 1865.0, 1739.3, 1608.8, 1582.8, 1557.1, 1495.6, 1447.6, 1353.1, 1318.5, 1274.8, 1232.3, 1117.0, 1077.7, 971.2, 826.9, 769.3, 696.5, 610.5; ^{1}H NMR(500 MHz, DMSO-d_6), δ: 7.26-7.32 (m, 3H), 7.41 (t, 2H, J = 8.0 Hz), 7.86 (d, 1H, J = 8.5 Hz), 7.97 (dd, 1H, J = 8.5, 1.5 Hz), 8.60 (s, 1H), 8.78 (s, 1H), 9.92 (s, 1H); ^{13}C NMR (125 MHz, DMSO-d_6), δ: 88.82, 116.91, 120.01, 121.16, 125.00, 125.86, 126.54, 129.50, 132.03, 135.30, 139.48, 147.88, 150.69, 154.02; HR-ESI (Q-TOF) m/z: calculated for $C_{16}H_{11}BrN_3^+$ ($M+H^+$): 324.0136, found: 324.0135.

Synthesis of 6-bromo-N-(3-chloro-4-fluoro-phenyl)-quinoline-3-carbnitrile-4-amine (47).

2.0 grams of **45** (3.8 mmol), 0.8 g (5.5 mmol) of 3-chloro-4-fluoro-aniline, and 2-propanol were added, vigorously stirred and heated at 80 ºC, overnight with a condenser. After 24 hours, it was cooled to room temperature, concentrated under reduced pressure, 50 mL of 1M KOH solution was added and stirred for 20 min, 100 mL of EtOAc was added, then organic solution was extracted three times through separation funnel and concentrated. It was crystallization from methanol, ethyl acetate to afford yellow powder of **47** (553 mg, 38.8 %); mp: 210-212℃ ; IR ν_{max}(cm^{-1}): 3528.2, 3328.5, 3223.7, 3178.0, 3090.5, 3038.5, 2917.7, 2849.4, 2214.1, 1900.6, 1733.8, 1607.0, 1581.6, 1560.0, 1486.9, 1415.3, 1353.2, 1257.2, 1220.2, 1117.6,

1075.0, 978.2, 821.5, 771.3, 673.2, 650.9; ^{1}H NMR(500 MHz, DMSO-d_6), δ: 7.37 (s, 1H), 7.46 (t, 1H, J = 8.5 Hz), 7.62 (s, 1H), 7.89 (s, 1H), 7.98 (d, 1H, J = 8.0 Hz), 8.63 (s, 1H), 8.74 (s, 1H), 9.97 (s, 1H); ^{13}C NMR (125 MHz, DMSO-d_6), δ: 88.60, 117.01, 117.49-117.66 (d, $J_{C,F}$ = 21.25 Hz), 120.05-120.10 (d, $J_{C,F}$= 6.25 Hz), 120.20, 121.11, 125.81, 126.04-126.08 (d, $J_{C,F}$ = 5.0 Hz), 127.27, 131.76, 135.38, 137.06, 147.52, 150.77, 153.71, 154.83-156.78 (d, $J_{C,F}$ = 243.75 Hz); HR-ESI (Q-TOF) m/z: calculated for $C_{16}H_8BrClFN_3^+$ ($M+H^+$): 377.9632, found: 377.9632.

*Synthesis of 6-bromo-N-(3-chloro-4-((3-fluorophenyl)methoxy)phenyl)-quinoline-3-carbnitrile-4-amine (**48**).*

1.0 grams of **45** (3.8 mmol), 1.38 g (5.5 mmol) of 3-chloro-4-[(3-fluorophenyl) methoxy]-benzenamine, and 2-propanol were added, vigorously stirred and heated at 80 ºC, overnight with a condenser. After 24 hours, it was cooled to room temperature, concentrated under reduced pressure, 50 mL of 1M KOH solution was added and stirred for 20 min, 100 mL of EtOAc was added, then organic solution was extracted three times through separation funnel and concentrated. It was crystallization from methanol, ethyl acetate to afford yellow powder of **48** (647 mg, 35.4 %); mp: 208-210℃ ; IR ν_{max}(cm^{-1}):3366.4, 3074.0, 2923.7, 2205.9, 1870.6, 1739.3, 1606.5, 1582.9, 1559.9, 1500.7, 1447.1, 1353.5, 1311.4, 1288.5, 1268.8, 1221.9, 1117.7, 1059.4, 1027.2, 979.4, 894.3, 805.7, 745.8, 682.6, 610.5; ^{1}H NMR(500 MHz, DMSO-d_6), δ: 5.28 (s, 2H), 7.17 (t, 1H, J = 8.0 Hz), 7.26-7.34 (m, 4H), 7.45-7.50 (m, 2H), 7.85 (d, 1H, J = 9.0 Hz), 7.97 (d, 1H, J = 7.5 Hz), 8.57 (s, 1H), 8.76 (s, 1H), 9.87 (s, 1H); ^{13}C NMR (125 MHz, DMSO-d_6), δ: 69.86, 87.72, 114.42-114.60 (d, $J_{C,F}$= 22.5 Hz),

114.75, 115.10-115.27 (d, $J_{C,F}$= 21.25 Hz), 117.09, 119.94, 120.71, 122.09, 123.79-123.81 (d, $J_{C,F}$= 2.5 Hz), 125.70, 126.22, 127.89, 130.98-131.04 (d, $J_{C,F}$= 7.5 Hz), 132.01, 132.99, 135.27, 139.82-139.88 (d, $J_{C,F}$= 7.5 Hz), 147.72, 151.12, 152.47, 154.09, 161.69-163.63 (d, $J_{C,F}$= 242.5 Hz); HR-ESI (Q-TOF) m/z: calculated for $C_{23}H_{15}BrClFN_3O^+$ ($M+H^+$): 484.0051, found: 484.0051.

*Synthesis of 6-(4-(Dimethyl-amino)phenyl)-N-(phenyl)-quinoline-3-carbonitrile-4-amine (**38**).*

0.8 g (2.5 mmol) of 6-bromo-N-(phenyl)-quinoline-3-carbnitrile-4-amine (**46**), 650 mg (3.2 mmol) of 4-(dimethylamino)phenylboronic acid hydrochloride, 80 mg of PPh_3, 10 mL of Et_3N, and 10 mL of DMF were placed in a 50 mL Schlenk flask with a stirrer bar under nitrogen purge. The reaction mixture was degassed for a further 30 min under a slow stream of nitrogen, at which point 80 mg of $Pd(OAc)_2$ was added. The reaction mixture was heated at 80 ºC for 24 h, cooled, filtered through filter paper and eluted solution was added into 50 mL of H_2O directly, and ethyl acetate was poured onto funnel to wash the residues. Water and ethyl acetate solution mixture went through extraction with three times with 200 mL of ethyl acetate each. The organic layer was dried with $MgSO_4$, filtered, and then concentrated under reduced pressure. The solid was crystalized in methanol, ethylacetate multiple times to afford light yellow powder of CQ (**38**). (165.0 mg, 18.1 %); mp: 275-276℃ (dec); IR $\nu_{max}(cm^{-1})$: 3197.2, 3159.9, 3082.3, 3060.4, 2989.3, 2888.7, 2814.2, 2220.7, 1944.4, 1851.4, 1733.8, 1603.5, 1577.8, 1547.0, 1494.6, 1445.7, 1363.5, 1308.5, 1297.3, 1263.6, 1063.1, 965.9, 898.4, 808.6, 762.3, 691.6, 622.3; ^{1}H NMR(500 MHz, DMSO-d_6), δ: 2.97 (s, 6H), 6.84 (d,

2H, J = 9.0 Hz), 7.25 (t, 1H, , J = 7.5 Hz), 7.32 (d, 2H, J = 8.0 Hz), 7.42 (t, 2H, J = 7.5 Hz), 7.75 (d, 2H, J = 9.0 Hz), 7.93 (d, 1H, J = 9.0 Hz), 8.13 (dd, 1H, J = 9.0, 1.5 Hz), 8.51 (s, 1H), 8.67 (d, 1H, J = 1.5 Hz), 9.90(s, 1H); ^{13}C NMR (125 MHz, DMSO-d_6), δ: 40.44, 88.51, 112.96, 117.44, 118.50, 120.09, 124.99, 126.26, 126.48, 128.09, 129.52, 130.33, 130.46, 138.79, 140.04, 147.76, 150.68, 151.38, 152.49; HR-ESI (Q-TOF) m/z: calculated for $C_{24}H_{21}N_4^+$ ($M+H^+$): 365.1766, found:365.1763.

*Synthesis of 6-(4-(4-Methylpiperazin-1-yl)phenyl)-N-(3-chloro-4-fluoro-phenyl)-quinoline-3-carbonitrile-4-amine (**39**).*

500 milligrams (1.3 mmol) of 6-bromo-N-(3-chloro-4-fluoro-phenyl)-quinoline-3-carbnitrile-4-amine (**47**), 450 mg (2.0 mmol) of 4-(4-Methylpiperazin-1-yl)phenylboronic acid , 50 mg of PPh_3, 10 mL of Et_3N, and 10 mL of DMF were placed in a 50 mL Schlenk flask with a stirrer bar under nitrogen purge. The reaction mixture was degassed for a further 30 min under a slow stream of nitrogen, at which point 50 mg of $Pd(OAc)_2$ was added. The reaction mixture was heated at 80 ^oC for 24 h, cooled, filtered through filter paper and eluted solution was added into 50 mL of H_2O directly, and ethyl acetate was poured onto funnel to wash the residues. Water and ethyl acetate solution mixture went through extraction with three times with 200 mL of ethyl acetate each. The organic layer was dried with $MgSO_4$, filtered, and then concentrated under reduced pressure. It was purified over silica (100 % EtOAc to 100% MeOH), followed by crystallization in methanol, ethyl acetate multiple times to afford light yellow powder of **39** (145.2 mg, 23.7 %); mp: 220-222℃ (dec); IR ν_{max}(cm^{-1}): 3571.1, 3331.2, 3170.1, 2965.5, 2937.8, 2888.0, 2836.3, 2811.5, 2211.6, 1867.8, 1766.6, 1663.0,

1602.4, 1587.4, 1533.9, 1494.3, 1414.9, 1361.1, 1254.5, 1128.5, 1077.6, 1009.2, 973.1, 844.4, 773.8, 655.2; ^{1}H NMR(500 MHz, DMSO-d_6), δ: 2.22 (s, 3H), 2.46 (broad s, 4H), 3.22 (broad s, 4H), 7.05 (d, 2H, J = 7.5 Hz), 7.38 (s, 1H), 7.47 (t, 1H, , J = 9.0 Hz), 7.61 (s, 1H), 7.76 (d, 2H, J = 7.5 Hz), 7.93 (d, 1H, J = 8.5 Hz), 8.13 (d, 1H, J = 8.0 Hz), 8.55 (s, 1H), 8.67 (s, 1H), 10.00 (s, 1H); ^{13}C NMR (125 MHz, DMSO-d_6 + TFA), δ: 42.56, 45.65, 52.59, 88.10, 116.50, 117.15, 117.55-117.72 (d, $J_{C,F}$= 21.25 Hz), 119.38, 119.85, 120.10-120.25 (d, $J_{C,F}$= 18.75 Hz), 126.36-126.42 (d, $J_{C,F}$= 7.5 Hz), 127.62, 128.26, 129.41, 130.17, 131.08, 137.15, 138.48, 146.65, 149.87, 152.02, 152.34, 154.94-156.89 (d, $J_{C,F}$= 243.75 Hz); HR-ESI (Q-TOF) m/z: calculated for $C_{27}H_{24}ClFN_5^+$ ($M+H^+$): 472.1704, found: 472.1673.

*Synthesis of 6-(4-(4-Methylpiperazin-1-yl)phenyl)-N-(3-chloro-4-((3-fluorophenyl)methoxy) phenyl)-quinoline-3-carbonitrile-4-amine (**40**).*

500 milligrams (1.0 mmol) of **48**, 450 mg (2.0 mmol) of 4-(4-Methylpiperazin-1-yl)phenylboronic acid, 50 mg of PPh_3, 10 mL of Et_3N, and 10 mL of DMF were placed in a 50 mL Schlenk flask with a stirrer bar under nitrogen purge. The reaction mixture was degassed for a further 30 min under a slow stream of nitrogen, at which point 50 mg of $Pd(OAc)_2$ was added. The reaction mixture was heated at 80 ºC for 24 h, cooled, filtered through filter paper and eluted solution was added into 50 mL of H_2O directly, and ethyl acetate was poured onto funnel to wash the residues. Water and ethyl acetate solution mixture went through extraction with three times with 200 mL of ethyl acetate each. The organic layer was dried with $MgSO_4$, filtered, and then concentrated under reduced pressure. It was purified over silica (100 % EtOAc to 100% MeOH), followed

by crystallization from methanol, ethyl acetate multiple times to afford yellow powder of **40** (74.0 mg, 12.8 %); mp: 254-256℃ (dec); IR ν_{max}(cm^{-1}): 3353.9, 3071.4, 2970.2, 2937.4, 2847.0, 2804.1, 2199.9, 1870.6, 1605.7, 1583.1, 1514.2, 1443.3, 1359.9, 1299.3, 1264.8, 1215.1, 1161.9, 1060.5, 1030.4, 1009.4, 953.2, 889.5, 784.5, 748.6, 690.0, 657.3; ^{1}H NMR(500 MHz, DMSO-d_6), δ: 2.23 (s, 3H), 2.47 (broad s, 4H), 3.23 (broad s, 4H), 5.29 (s, 2H), 7.06 (d, 2H, J = 9.0 Hz), 7.17 (t, 1H, , J = 8.0 Hz), 7.28-7.35 (m, 4H), 7.45 (q, 1H, J = 8.0 Hz), 7.52 (s, 1H), 7.77 (d, 2H, J = 9.0 Hz), 7.92 (d, 1H, J = 8.5 Hz), 8.14 (d, 1H, J = 7.5 Hz), 8.50 (s, 1H), 8.69 (s, 1H), 9.88 (s, 1H); ^{13}C NMR (125 MHz, DMSO-d_6), δ: 46.26, 48.07, 54.97, 69.86, 87.26, 114.42-114.60 (d, $J_{C,F}$= 22.5 Hz), 114.80, 115.10-115.27 (d, $J_{C,F}$= 21.25 Hz), 115.76, 117.57, 118.82, 119.56, 122.11, 123.79-123-81 (d, $J_{C,F}$= 2.5 Hz), 126.24, 127.94, 128.04, 129.01, 130.33, 130.50, 130.98-131.05 (d, $J_{C,F}$= 8.75 Hz), 133.49, 138.39, 139.85-139.91 (d, $J_{C,F}$= 7.5 Hz), 147.74, 151.25, 151.85, 152.32, 152.82, 161.70-163.64 (d, $J_{C,F}$= 242.5 Hz); HR-ESI (Q-TOF) m/z: calculated for $C_{34}H_{30}ClFN_5O^+$ ($M+H^+$): 578.2123, found: 578.2117.

4.2.2 Optical spectroscopy

The optical properties of CQ (**38**), CQ1 (**39**) and CQ2 (**40**) were examined in organic solvents to evaluate their sensitivity to their chemical environment and polarity-dependent fluorescence.

The moderately polar organic solvents, such as $CHCl_3$, closely match the apparent polarity of the ATP binding pocket of ERBB2 and emission in these solvents indicates imaging parameters for fluorescence microscopy.[29]

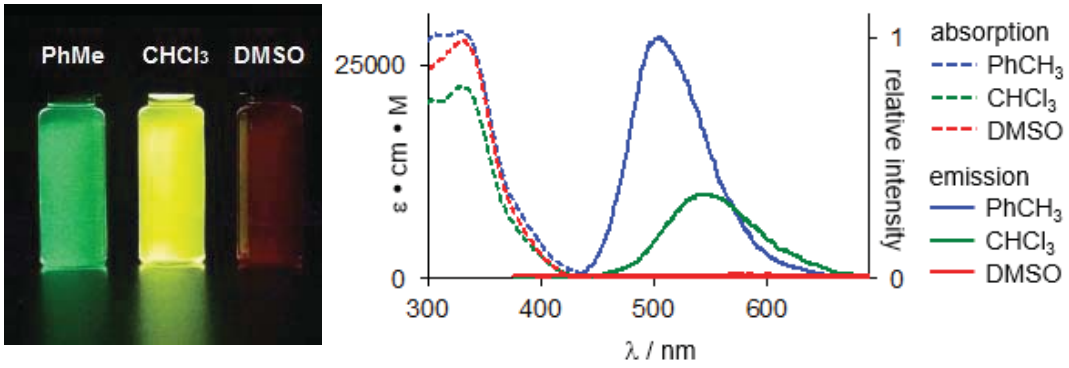

Figure 4.3. Absorption and emission spectra of CQ1 (**39**) in several solvents demonstrating the sensitivity of the excited state to solvent polarity.

UV-vis absorption spectroscopy showed little variation between solvents, with peak absorption at 330 nm for both compounds, however, fluorescence spectroscopy showed probe sensitivity for polarity.

CQ1 (**39**) was emissive in solvents of low polarity, such as toluene, E_T30 = 33.9 kcal/mol on Reichardt's scale, and chloroform (E_T30 = 39.1 kcal/mol), but essentially non-emissive in solvents more polar that DMSO (E_T30 = 45.0 kcal/mol).[39] Emission was completely quenched in water, octanol, methanol and acetonitrile, which have ET30 values ranging from 46.0 to 63.1 kcal/mol. A linear correlation between solvent polarity and emission wavelength was found by examining several other solvents (Figure 4.4A) and the shift in emission wavelength was found to be higher for CQ1 (**39**) compared to QA1 (**5**), demonstrating that the more polar excited state was better stabilized in polar solvents. The marked red-shift in the emission spectra of CQ1 (**39**), relative to QA1 (**5**), is also apparent by eye when comparing the probes in identical solvents, as shown in Figure 4.4B.

Table 4.1. Photophysical parameters of CQ (**38**), CQ1 (**39**), CQ2 (**40**) in solution.

Solvent / **38**	PhMe	$CHCl_3$	MeCN	MeOH	OcOH	PBS	DMSO
$\lambda_{max, abs}$ (nm)	335	338	336	340	341	344	344
ε (M^{-1} cm^{-1})	29300	30000	31400	29000	30600	23800	29600
$\lambda_{max, FL}$ (nm)	487	527	398	399	622	404	397
Φ_{FL}[a]	0.27	0.34	0.005	0.002	0.03	0.003	0.0000001
Solvent / **39**	PhMe	$CHCl_3$	MeCN	MeOH	OcOH	PBS	DMSO
$\lambda_{max, abs}$ (nm)	329	330	330	330	332	300	337
ε (M^{-1} cm^{-1})	28900	22400	27800	25500	27200	22300	28000
$\lambda_{max, FL}$ (nm)	498	525	410	403	404	410	561
Φ_{FL}[a]	0.38	0.22	0.004	0.003	0.03	0.003	0.01
Solvent / **40**	PhMe	$CHCl_3$	MeCN	MeOH	OcOH	PBS	DMSO
$\lambda_{max, abs}$ (nm)	310	331	332	335	335	336	340
ε (M^{-1} cm^{-1})	29900	24900	27200	25400	27700	22700	28200
$\lambda_{max, FL}$ (nm)	570	405	405	413	401	545	402
Φ_{FL}[a]	0.01	0.01	0.003	0.002	0.01	0.01	0.005

[a]± 10%

This shows the effect of the electron-withdrawing nitrile, which lowers the energy of the S_1 state. While CQ1 (**39**) was found to be emissive, CQ2 (**40**) showed no emission in any solvent.

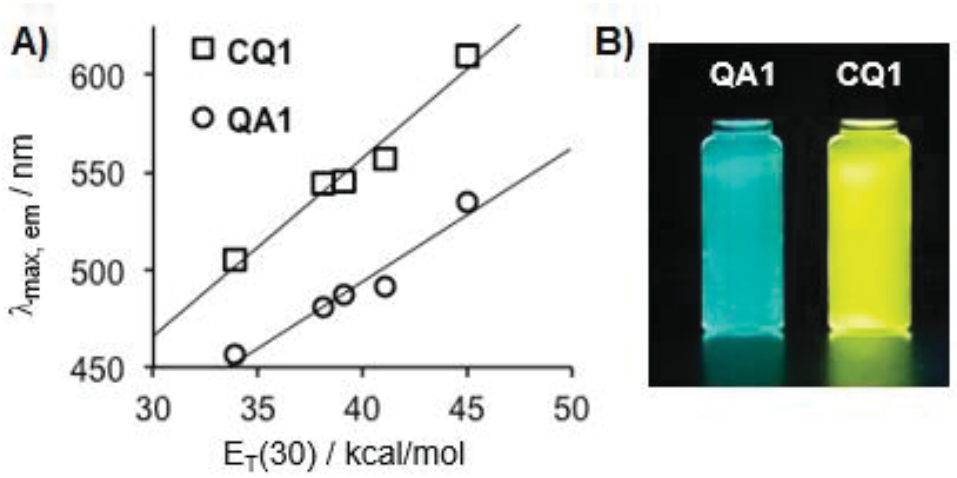

Figure 4.4. A) Comparison of the emission maxima of CQ1 (**39**) and QA1 (**5**) in various solvents reveals that the cyano-quinoline core of CQ1 (**39**) is slightly more responsive to solvent polarity. B) A visual comparison of QA1 (**5**) and CQ1 (**39**) in chloroform shows the red-shifted emission of CQ1 (**39**).

By comparison, the quinazoline analog, QA2 (**6**), was weakly emissive in relation to QA1 (**5**). The addition of the Type II pharmacophore arm appears to have a quenching effect on both the 3-cyanoquinoline and quinazoline fluorophore cores, which is exacerbated by the presence of the electron withdrawing cyano-group. We attribute this quenching to an excited state electron transfer process, from the electron-rich N-phenyl-benzyloxy ether.[73] Thus, while CQ2 (**39**) is cannot be utilized as a fluorescent turn-on probe, CQ1 (**39**) is ideally suited as a red-emissive, Type I inhibitor. In addition, the chemico-physical properties of **38**-**40** were calculated with SwissADME to obtain an insight of molecules cellular distribution and pharmacokinetics.[42-44] Along with the partition coefficient, the turn-on ratio in octanol versus water was measured to

predict the responsiveness of probes.[45] The ratios of **38-40** emission intensities obtained in octanol and water are shown in Figure 4.5.

Table 4.2. Chemico-physical properties of CQ (**38**), CQ1 (**39**), CQ2 (**40**).

Properties / Compounds	Molar refractivity	Topological polar surface area	log P $_{o/w}$	log K $_p$
CQ (**38**)	115.64	51.95 Å	3.19	-4.44 cm/s
CQ1 (**39**)	142.67	55.19 Å	3.81	-4.71 cm/s
CQ2 (**40**)	173.64	64.42 Å	4.36	-3.32 cm/s

Properties / Compounds	Blood brain barrier Permeant	Gastrointestinal absorption
CQ (**38**)	Yes	High
CQ1 (**39**)	No	High
CQ2 (**40**)	No	Low

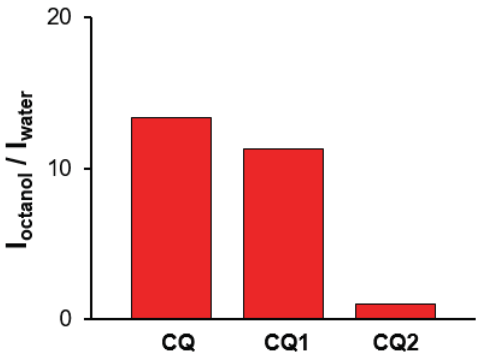

Figure 4.5. Turn-On ratio of CQ (38), CQ1 (39) and CQ2 (40).

4.2.3 Inhibition study

The abilities of CQ1 (**39**) and CQ2 (**40**) on inhibition of ERBB2 phosphorylation were evaluated through immunohistochemistry assay. The probes were treated on MCF7

cells with six concentrations, 0, 39, 156, 625, 2500 and 10000 nM. MCF7 cells are a well-established model system for the ligand induced activation of ERBB2-ERBB3 hetero-complexes by ligand of the neuregulin family (NRGβ1 in this case). The MCF7 cells were seeded with equal quantity (200 thousand/well) in six-well plates. After 48 hours, cells were pre-treated with the small molecule inhibitors of various concentrations for 1 hour before induction by neuregulin (NRGβ1, 30 nM, 30 minutes). Cell lysates were generated immediately by SDS lysis. Equal aliquots were subjected to SDS- PAGE and Western blot analysis.

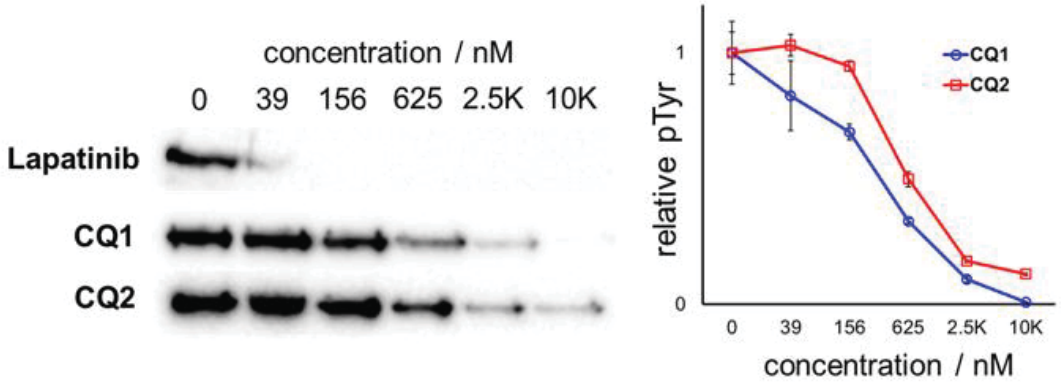

Figure 4.6. Determination of Ki values of CQ1 (**39**) and CQ2 (**40**) via ligand stimulation assay in MCF7 cells; lapatinib included (top row) for comparison.

ERBB2 phosphorylation was evaluated for Tyr1139 located close to the extreme cytoplasmic C-terminus of the receptor (validated by pan-TyrP detection (4G10)). The signal obtained for pTyr1139 relative to the ERBB2 receptor levels was determined as the relative receptor phosphorylation. Ki values of 390 nM and 590 nM were determined for CQ1 (**39**) and CQ2 (**40**), respectively, in receptor stimulation assays.

4.2.4 Binding induced fluorescence study on CQ probes and anti-cancer drugs

We next investigated the binding-induced, turn-on emission of CQ1 (**39**) and its optical compatibility with several commercially available inhibitors in the presence of purified ERBB2 kinase domain. As shown in Figure 4.7, the excitation spectra of ERBB2-bound CQ1 (**39**) is similar to ERBB2-bound QA1 (**5**) and overlaps significantly with quinazoline-based ERBB inhibitors such as gefitinib and lapatinib.

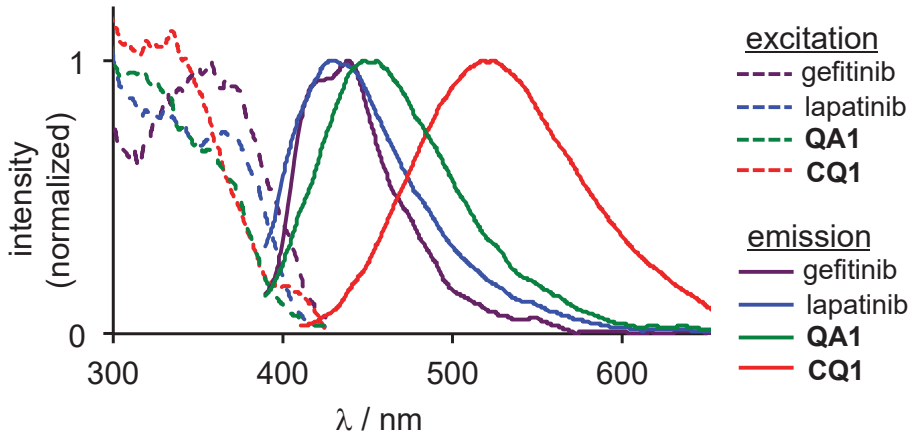

Figure 4.7. Comparison of excitation and emission spectra, in the presence of purified ERBB2 kinase domain, of two quinazoline inhibitors, gefitinib and lapatinib, with quinazoline probe, QA1 (**5**) and cyano-quinoline probe, CQ1 (**39**). While all four compounds share similar excitation spectra, the emission of CQ1 (**39**) is significantly red-shifted, allowing for selective imaging of ERBB2-binding in cells treated with ERBB2-targeted inhibitors.

However, CQ1 (**39**) is distinguishable from QA1 (**5**), gefitinib and lapatinib through a large, 200 nm Stokes shift, which sufficiently segregates the emission of this probe from the kinase inhibitors. The emission maximum of the bound form of CQ1 (**39**) is

520 nm, compared to 440 nm for ERBB2-bound lapatinib and gefitinib, providing a unique optical window that allows for selective monitoring of CQ1 (**39**) emission in the presence of ERBB2-directed inhibitors. Having established the optical compatibility of CQ1 (**39**) with quinazoline-based inhibitors, we next examined the live cell imaging capabilities of this probe.

4.2.5 Confocal microscopy

Specific detection of internalized ERBB2 receptor tyrosine kinase

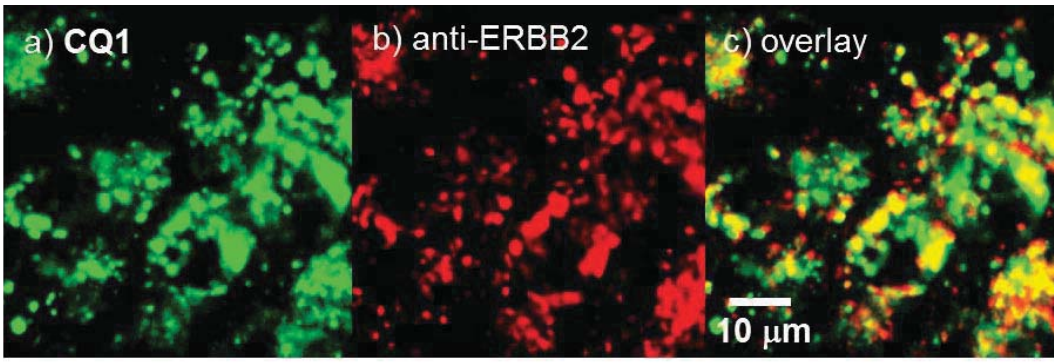

Figure 4.8. CQ1 (**39**) co-localizes with anti-ERBB2 staining: a) the false-colored green channel shows CQ1 (**39**) distribution, l_{ex} = 405 nm, l_{em} = 500 - 600 nm; b) the false-colored red channel shows antibody staining of ERBB2; c) overlay of the two channels shows a high degree of overlap.

Firstly, the ability of CQ1 (**39**) as an ERBB2-targeted probe was evaluated in a live cell setting using BT474 cells, which are classified clinically as HER2(+) and express ~10^6 copies of ERBB2 per a cell. The BT474 cells were first treated with ERBB2-directed antibody, then treated with 2 μM solutions of CQ1 (**39**).

Figure 4.8 presents the two-channel image of the CQ1 (**39**) on green channel and the anti-ERBB2 staining on red channel, which show a high degree of overlap in the merged image. Minimal cell surface staining was observed for CQ1 (**39**), indicative of binding to internalized pool of ERBB2. On the other hand, the small molecule, membrane permeable probe required only 5 minutes of staining to saturate the same population.

Gefitinib induced internalization of ERBB2 receptor tyrosine kinase

The reversible Type I inhibitor, gefitinib affects the dimerization and internalization of ERBB2 as well as inhibiting kinase activity. However, the gefitinib's mechanism of inducing internalization has not been clearly elucidated. Thus, we also evaluated the effect of gefitinib on ERBB2 along with mechanistically well-studied inhibitors: irreversible Type I inhibitor, canertinib and two Type II, i.e. inactive state inhibitors, lapatinib and neratinib (blue and purple traces, Figure 4.9a). Canertinib (green trace, Figure 4.9b) induces a more moderate increase in CQ1 (**39**) emission that can be rationalized on the basis of higher affinity and ability to bind covalently, blocking competition from CQ1 (**39**).[83] By contrast, neither inactive state inhibitor elicited an increase in CQ1 (**39**), supporting the notion and structural features that CQ1 (**39**) binding is to the active state.[84] Gefitinib provides an interesting case-study for ERBB2 dynamics as it is a low-affinity inhibitor of ERBB2, with IC50 values varying widely from 0.24 μM[74] to in excess of 5 μM[75-77] and linked to factors such as expression level,[78,79] tumor type[75] and binding pocket mutations.[77,80]

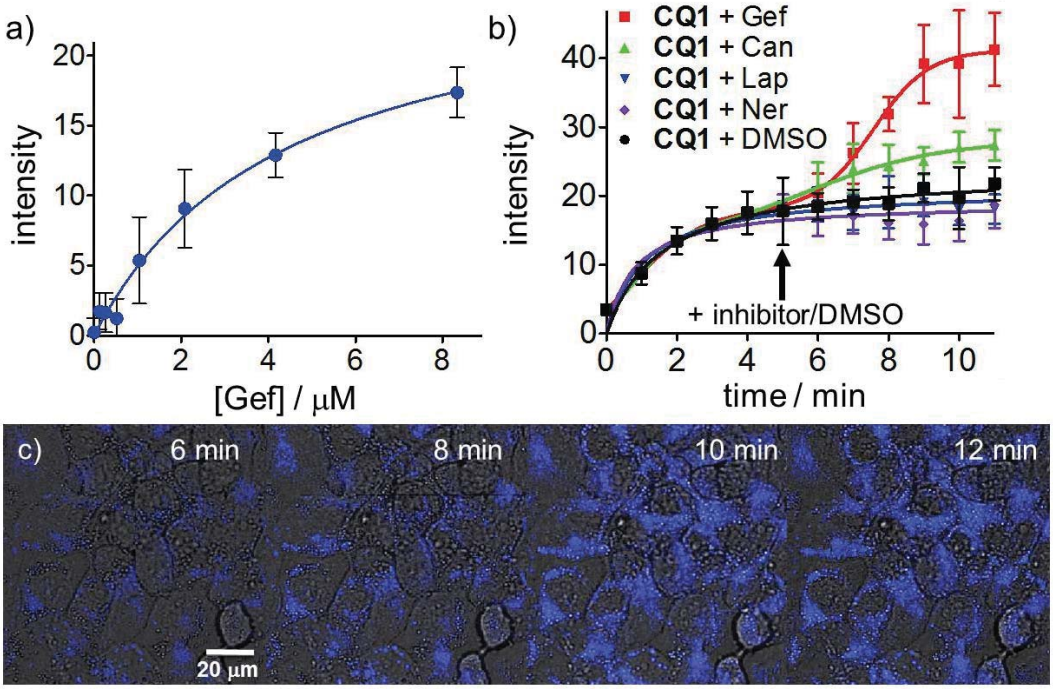

Figure 4.9. Imaging of gefitinib-induced, active conformation ERBB2-internalization: a) following CQ1 (**39**) saturation of ERBB2, the addition of gefitinib, and to a lesser extent canertinib, both active conformer inhibitors, produces an increase in CQ1 (**39**) emission intensity, while the addition of inactive state inhibitors, lapatinib or neratinib, does not; b) the gefitinib-induced emission increase shows a concentration dependence, with and EC50 of 4.4 μM that closes matches the reported IC50 values of 3.7 to 3.9 μM;[75,76] c) images of time dependent increase in emission in BT474 cells.

In terms of receptor dynamics, Gefitinib has been shown to induce heterodimerization[81] and internalization of ERBB2[82] providing an excellent opportunity to track dynamic ERBB2 pools with CQ1 (**39**) as a fluorescent reporter.

This is evident in the time-dependent emission intensity of cells first treated with CQ1 (**39**), followed by gefitinib treatment (red trace, Figure 4.9b). BT474 cells were exposed to 2 μM solutions of CQ1 (**39**) and after 5 min, the signal had plateaued, indicating saturation of the internal ERBB2 population. Subsequent addition of gefitinib (5 μM), induced a second wave of emission increase, which stabilized after 5-6 min. The gefitinib-induced response was found to be concentration dependent, as shown in Figure 4.9b, with an EC50 of 4.4 μM. This value correlates very well with the average IC50 value of 3.9 μM reported across several tumor types.[75] While gefitinib and CQ1 (**39**) target the same binding fold, CQ1 (**39**), with a Ki of 590 nM and used at 2 μM can effectively compete with gefitinib to access the binding pocket and report ERBB2 internalization. These two routes for ERBB2 inhibition are summarized in Figure 7d and although both have been linked to HSP90 displacement,[86] internalization of the active conformation appears to proceed via heterodimer formation, while the inactive conformation does not.[85] CQ1 (**39**) thus provides a route not only to image the internal pool of ERBB2 and dynamics of internalization, but also to differentiate drug binding modes which is linked to their effects on receptor conformation, dimerization and internalization.

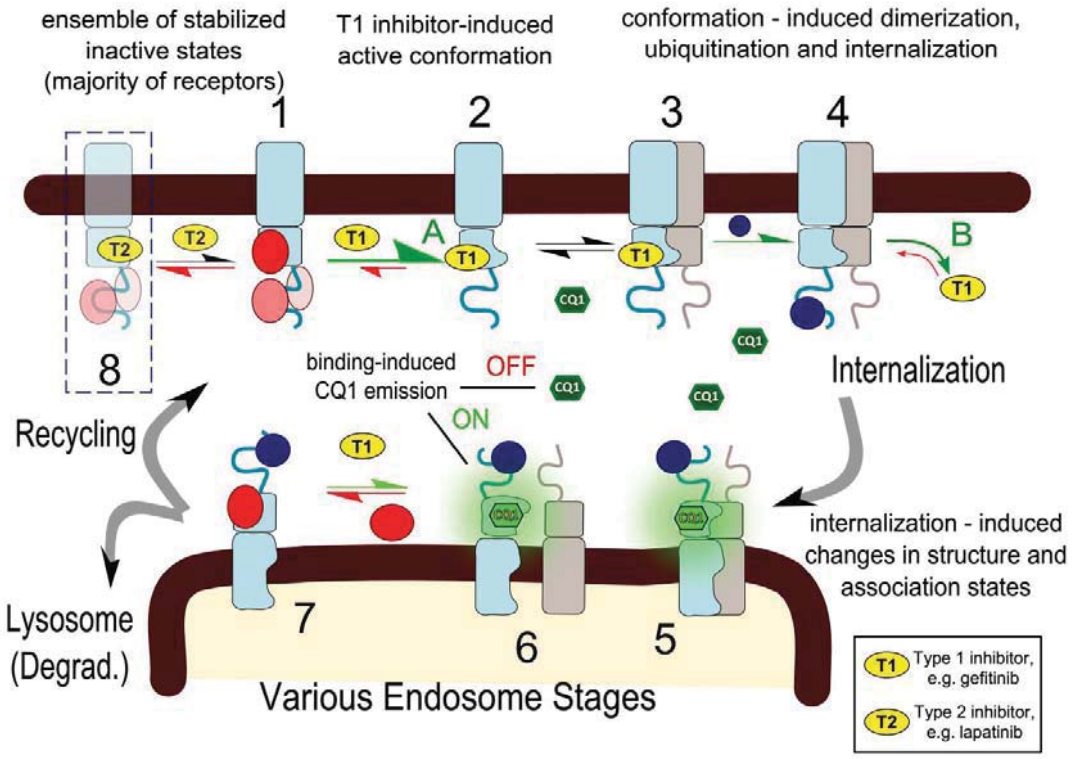

Figure 4.10. Stages in ERBB receptor signaling and model for potential interplay of CQ1 (**39**) and inhibitor binding: The active and inactive kinase conformations on the cell surface (1-4) preferentially associate with, and are stabilized by, distinct interaction partners. Binding of type-I and type-II inhibitors (**T1**, **T2**) shifts the equilibrium of association states and is known to drive both dimerization and internalization.[2,89-93] Internalization results in a change in association states and pH-induced changes in interactions and conformations of the extracellular domains (5-7).[3,54,93] At present, little is known about the relative affinity of established inhibitors and competition with kinase directed probes in these distinct states. Current data on probe CQ1 (**39**) (shown in on- and off-state) suggest that probe binding is favored in the internalized state.

4.3 Conclusion

In summary, we have developed an ERBB2-targeted kinase probe, CQ1 (**39**), utilizing a 3-cyanoquinoline core, studied the optical as well as biochemical properties, and demonstrated its utility in imaging dynamic shifts in receptor populations in response to various ERBB2-targeted inhibitors. The optical properties of CQ1 (**39**) were improved over previous fluorescent reporters, owing to the presence of the nitrile group serves to stabilize the charge transfer excited state and red-shift emission of the probe beyond that observed for early generation probes and clinically relevant EGFR/ERBB inhibitors. CQ1 (**39**) was found to have moderate affinity for ERBB2 and targets the intracellular pool, allowing this probe to function as a reporter of the rapid dynamics of kinase internalization, following inhibitor treatment.

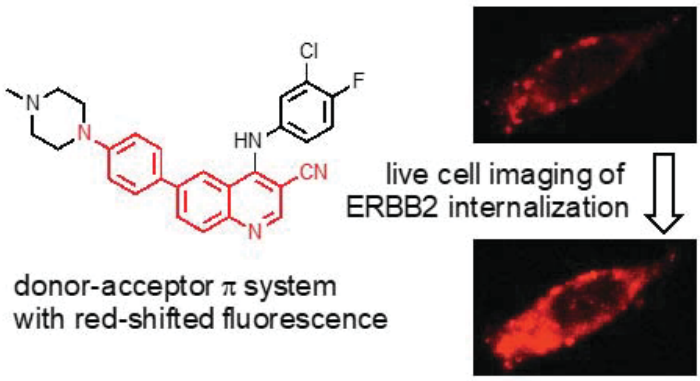

Figure 4.11. Cyanoquinoline-class Turn-On fluorescent probe for live imaging HER2 receptor tyrosine kinase in breast cancer cells.

Finally, CQ1 (**39**) probe was able to differentiate the response of inhibitors targeting the active and inactive conformation. These results serve as a demonstration of the

utility of a small molecule fluorescent reporter that is membrane permeable and can target an intracellular binding pocket. Future development of kinase-specific probes, adapted from existing and clinically available inhibitors, can complement established antibody-labeling strategies, providing information about dynamic shifts in kinase populations in response to specific drug treatments.

Chapter 5

SYNTHESIS AND CHARACTERIZATION OF ADDITIONAL MOLECULES

5.1 Overview

The fluorescent HER2 kinase probes have been developed to achieve dynamic observation on ERBB2 activation states. However, the quinazoline class, Type II probe detecting the inactive conformation of ERBB2 receptor (QA2, **6**) exhibited low quantum yield compared to Type I probe (QA1, **5**). Furthermore, cyano-quinoline class, Type II probe (CQ2, **40**) showed insignificant fluorescence in comparison to Type I probe (CQ1, **39**). In molecular structural aspect, the addition of the Type II pharmacophore arm may contribute to a quenching effect on quinazoline as well as the 3-cyanoquinoline fluorophore cores. Thus, we generated additional molecules to delve into the background of Type II probe design strategy. This quenching effect is attributed to an excited state electron transfer process from the electron-rich N-phenyl-benzyloxy ether. Therefore, we focused on developing potential Type II probes with higher quantum yield by replacing the Type II pharmacophore arm substitution.

Thus, we focused on maintaining the overall length of pharmacophore arm while hindering excited state electron transfer process from the N-phenyl-benzyloxy ether by changing substitution location of benzyloxy ether from para to meta position.

Initially, we examined the effect of translocating benzyloxy ether on optical property with simplified N-phenyl-methoxy pharmacophore arms in mono-substitution at para, meta, and di-substitution at both positions. The optical spectroscopy characterization suggested that the meta substitution of pharmacophore arm is effective for fluorescence enhancement for quinazoline system.

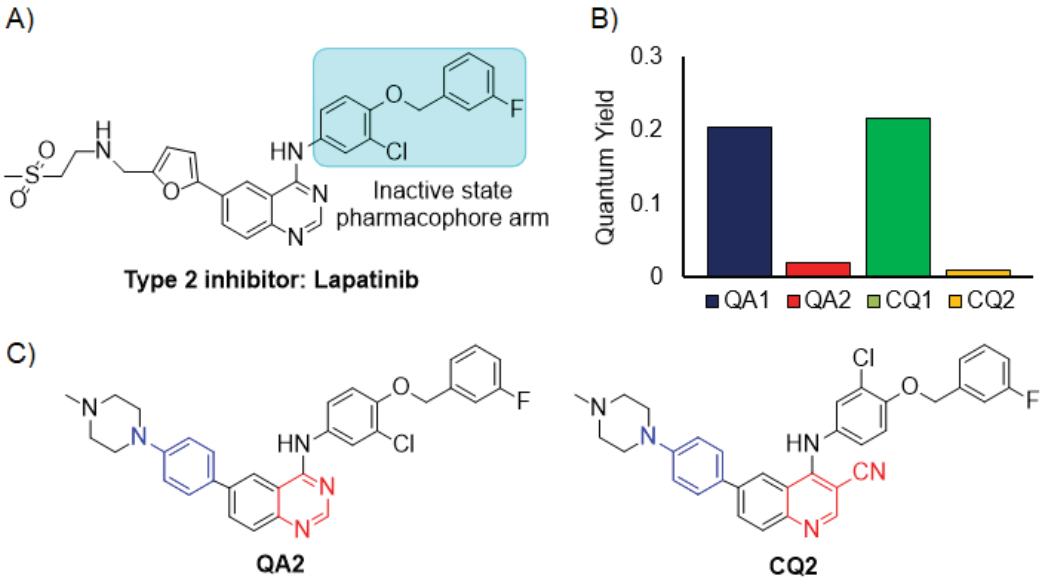

Figure 5.1. A) structure of Type II inhibitor, Lapatinib. B) quantum yields of Type I and 2 kinase probes: quinazoline probes QA1, QA2 and cyano-proline probes CQ1, CQ2. C) structure of Type II quinazoline and cyano-proline probes.

Based on this, we generated solubility optimized mata-QA2 (**52**) and meta-CQ2 (**53**), and conducted the optical spectroscopy characterization of mata-QA2 (**52**) and meta-CQ2 (**53**) in comparison to QA2 (**6**) and CQ2 (**40**). Although the meta-substitution of benzyloxy ether on Type II pharmacophore arm is effective for turn-on fluorescence enhancement, the structural modification was resulted in non-significant inhibition on ERBB2 phosphorylation on both of quinazoline and cyano-proline cores. It suggests the need of alternative strategies to hinder the photo-induced electron transfer from benzyloxy ether pharmacophore arm to acceptor core by maintaining the para-substitution.

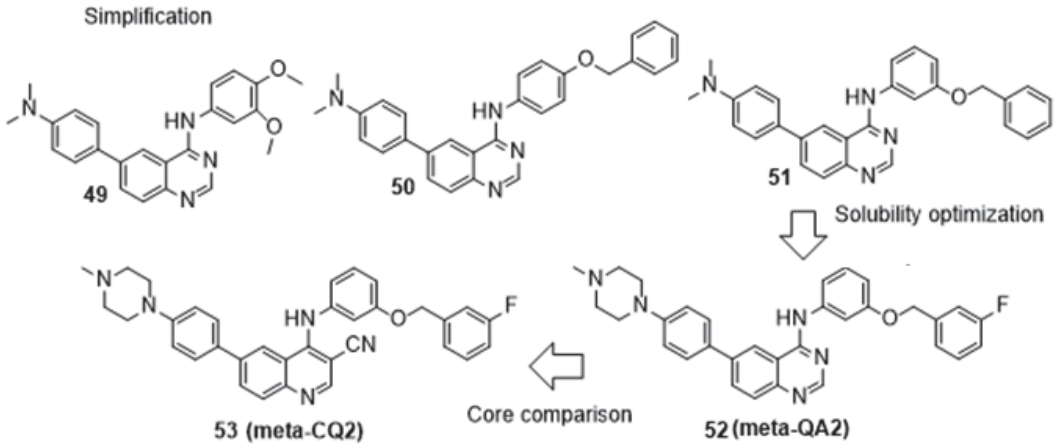

Figure 5.2. Synthesis target molecules.

5.2 Synthesis

Each step of reactions went through appropriate work-up processes, and was purified through silica column chromatography, recrystallization, and/or distillation. All synthesized compounds were obtained as powder colored in white or yellow. The physicochemical characterization of compounds was achieved through melting point measurement, IR spectra, high resolution mass spectra, ^{1}H NMR and ^{13}C NMR spectra recorded on 500 MHz spectrometer.

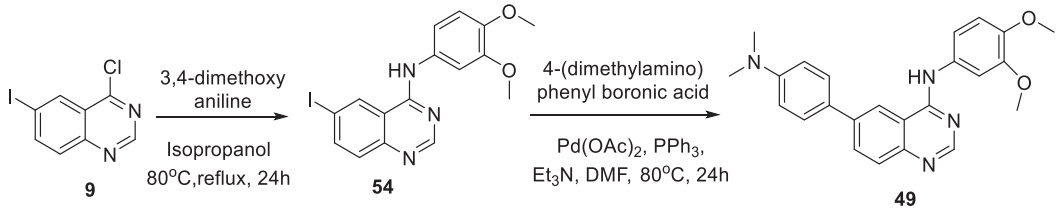

Scheme 5.1. Synthesis of **49**.

*Synthesis of N-(3,4-dimethoxyphenyl)-6-Iodo-quinazolin-4-amine (**54**)*

7.0 grams (24.1 mmol) of 4-choloro-6-iodo-quinazoline, 7.0 grams (45.7 mmol) of 3,4-dimethoxy aniline, and 2-propanol were placed in a 250 mL round bottom flask with

stirrer bar. The reaction was heated at 80 ºC with a condenser for 24 h, cooled to room temperature, concentrated under reduced pressure, 200 mL of 1M KOH solution was added and stirred for 20 min, purplish grey precipitate was isolated by filtering. Dried precipitate was added into 200 mL of EtOAc, stirred for 10 min, filtered to separate solid impurities and eluted solution was concentrated, then it was sonicated in 50 mL of dichloromethane, and filtered. Filtered solid was crystalized from 2-propanol and methanol with ethyl acetate to afford green powder of N-(3,4-dimethoxyphenyl)-6-Iodo-quinazolin-4-amine (2.260 g, 23.0 %).; mp: 192-193 ℃; IR ν_{max}(cm^{-1}): 3358.0, 3001.9, 2942.6, 2907.6, 2831.1, 1833.8, 1620.4, 1599.9, 1567.6, 1508.3, 1443.4, 1404.9, 1380.1, 1269.4, 1142.9, 876.3, 853.1, 766.6, 740.2, 682.5, 607; ^{1}H NMR(500 MHz, DMSO-d_6), δ: 3.77 (s, 3H), 3.78 (s, 3H), 6.97 (d, 1H, J = 8.5 Hz), 7.41-7.44 (m, 2H), 7.52 (d, 1H, J = 8.5 Hz), 8.08 (dd, 1H, J = 8.5, 1.5 Hz), 8.56 (s, 1H), 8.96 (d, 1H, J = 1Hz), 9.73 (s, 1H); ^{13}C NMR (125 MHz, DMSO-d_6), δ: 56.04, 56.23, 91.72, 108.17, 112.22, 115.27, 117.39, 130.24, 131.81, 132.64, 141.64, 146.06, 148.88, 149.21, 155.47, 156.98; HR-ESI (Q-TOF) m/z: calculated for $C_{16}H_{15}IN_3O_2^+$ ($M+H^+$): 408.0209, found: 408.0224.

*Synthesis of 6-(4-(Dimethyl-amino)phenyl)-N-(3,4-dimethoxyphenyl)-quinazolin-4-amine (**49**)*

790 milligrams (1.9 mmol) of N-(3,4-dimethoxyphenyl)-6-Iodo-quinazolin-4-amine, 1.0 g (5.0 mmol) of 4-(dimethylamino)phenyl-boronic acid hydrochloride, 130 mg of PPh_3, 3.0 mL of Et_3N, and 10.0 mL of dried DMF were placed in a 50 mL Schlenk flask with a stirrer bar under nitrogen purge. The reaction mixture was degassed for a further 30 min under a slow stream of nitrogen, at which point 100 mg of $Pd(OAc)_2$

was added. The reaction mixture was heated at 80 ºC for 24 h, cooled, poured into 300 mL of H_2O, and extracted with EtOAc (4 × 200 mL). The organic layer was dried with $MgSO_4$, filtered, and then concentrated under reduced pressure. It was purified over silica (100% CH_2Cl_2 to 100% EtOAc) followed by crystallization from 2-propanol, methanol, ethyl acetate to afford light yellow powder of 6-(4-(Dimethyl-amino)phenyl)-N-(3,4-dimethoxyphenyl)-quinazolin-4-amine (82 mg, 10.8 %); mp: 241 ℃; IR ν_{max}(cm^{-1}): 3210.6, 3005.2, 2918.8, 2837.0, 2796.5, 1933.4, 1601.6, 1568.6, 1503.3, 1440.3, 1396.4, 1332.7, 1262.6, 1136.8, 1003.6, 865.3, 850.3, 765.4, 745.7, 651.7, 611.1; ^{1}H NMR(500 MHz, DMSO-d_6), δ: 2.99 (s, 6H), 3.78 (s, 3H), 3.80 (s, 3H), 6.87 (d, 2H, J = 9.0 Hz), 6.99 (d, 2H, J = 9.0 Hz), 7.45 (s, 1H), 7.76 (d, 3H, J = 9.0 Hz), 8.11 (d, 1H, J = 8.5 Hz), 8.50 (s, 1H), 8.70 (s, 1H), 9.76 (s, 1H); ^{13}C NMR (125 MHz, DMSO-d_6), δ: 40.47, 56.07, 56.25, 108.50, 112.28, 113.01, 115.54, 115.97, 118.56, 126.92, 128.06, 128.60, 131.27, 132.96, 138.62, 145.99, 148.65, 148.92, 150.59, 154.38, 158.22; HR-ESI (Q-TOF) m/z: calculated for $C_{24}H_{25}N_4O_2^+$ ($M+H^+$): 401.1978, found: 401.1971.

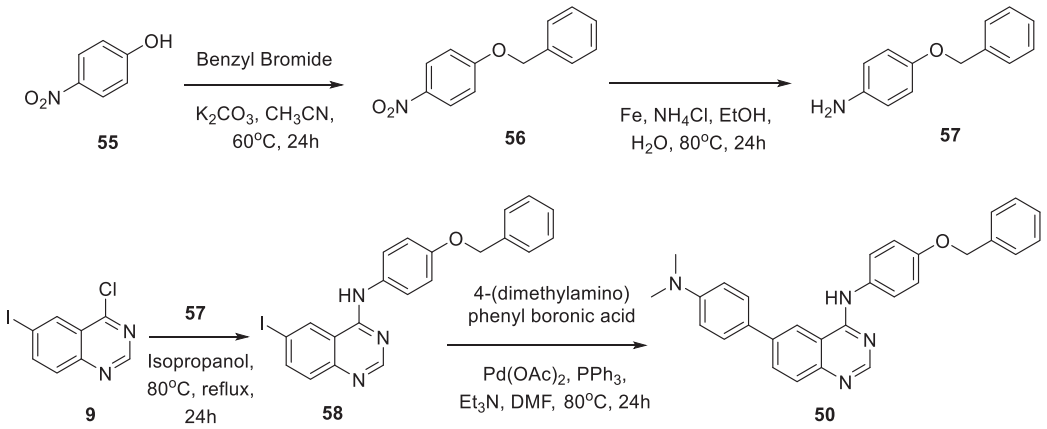

Scheme 5.2. Synthesis of **50**.

*Synthesis of 6-(4-(Dimethyl-amino)phenyl)-N-(4-((phenyl)methoxy)phenyl)-quinazolin-4-amine (**50**).*

1.0 grams (2.2 mmol) of N-(4-[(phenyl)methoxy]-phenyl)-6-iodo-quinazolin-4-amine (**58**), 0.9 g (4.5 mmol) of 4-(dimethylamino)phenyl-boronic acid hydrochloride, 130 mg of PPh_3, 5.0 mL of Et_3N, and 10.0 mL of dried DMF were placed in a 50 mL Schlenk flask with a stirrer bar under nitrogen purge. The reaction mixture was degassed for a further 30 min under a slow stream of nitrogen, at which point 130 mg of $Pd(OAc)_2$ was added. The reaction mixture was heated at 80 ºC for 24 h, cooled, poured into 300 mL of H_2O, and extracted with EtOAc (4 × 200 mL). The organic layer was dried with $MgSO_4$, filtered, and then concentrated under reduced pressure. It was purified over silica (100% DCM to 100% EtOAc) followed by crystallization from 2-propanol and then methanol to afford yellow powder of 6-(4-(Dimethyl-amino)phenyl)-N-(4-[(phenyl)methoxy]-phenyl)-6-iodo-quinazolin-4-amine (39 mg, 3.97 %); mp: 273.5℃ (dec); IR ν_{max}(cm^{-1}): 3237.5, 3038.9, 2910.4, 2815.2, 1947.6, 1606.6, 1563.7, 1535.3, 1498.8, 1467.6, 1418.8, 1400.2, 1361.4, 1321.4, 1297.4, 1211.9, 1129.1, 1064.5, 1006.5, 991.1, 864.1, 795.4, 696.6; ^{1}H NMR(500 MHz, DMSO-d_6), δ: 2.98 (s, 6H), 5.14 (s, 2H), 6.86 (d, 2H, J = 8.5 Hz), 7.07 (d, 2H, J = 9.0 Hz), 7.33 (t, 1H, J = 7.0 Hz), 7.40 (t, 2H, J = 7.5 Hz), 7.48-7.49 (m, 2H), 7.69 (d, 2H, J = 9.0 Hz), 7.76 (d, 3H, J = 8.5 Hz), 8.10 (dd, 1H, J = 9.0, 2.0 Hz), 8.47 (s, 1H), 8.69 (s, 1H), 9.79 (s, 1H); ^{13}C NMR (125 MHz, DMSO-d_6), δ: 40.49, 69.89, 113.03, 115.14, 115.91, 118.58, 124.96, 126.91, 128.04, 128.15, 128.27, 128.58, 128.90, 131.28, 132.69, 137.69, 138.59, 148.65, 150.61, 154.40, 155.39, 158.25; HR-ESI (Q-TOF) m/z: calculated for $C_{29}H_{27}N_4O^+$ ($M+H^+$): 447.2185, found: 447.2177.

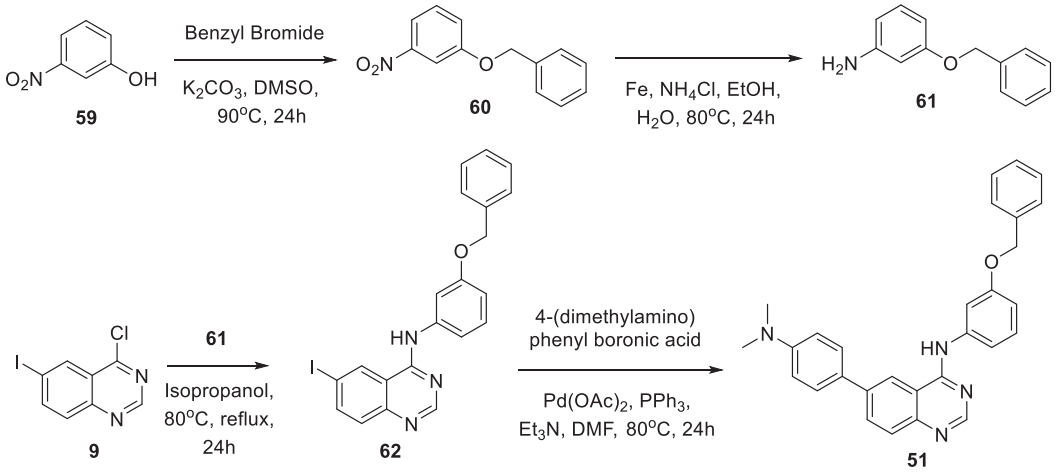

Scheme 5.3. Synthesis of **51**.

*Synthesis of N-((3-(phenyl)methoxy)phenyl)-6-iodo-4-quinazolin-4-amine (**62**).*

13.0 grams (45.0 mmol) of 4-choloro-6-iodo-quinazoline (**9**), 11 g (55.2 mmol) of 3-[(phenyl)ethoxy]-benzenamine (**61**), and 2-propanol were placed in a 500 mL round bottom flask with stirrer bar. The reaction was heated at 80 °C with a condenser for 24 h, cooled to room temperature, concentrated under reduced pressure, 200 mL of 1M KOH solution was added and stirred for 20 min, them grey precipitate was isolated by filtering. Dried precipitate was added into 200 mL of EtOAc, stirred for 10 min, filtered to separate solid impurities and eluted solution was concentrated, then crystalized from 2-propanol and methanol to afford light yellow powder of N-(3-[(phenyl)methoxy]-phenyl)-6-iodo-quinazolin-4-amine (6.5 g, 31.8 %).; mp: 304 ℃; IR ν_{max}(cm^{-1}): 3385.6, 3129.8, 3028.8, 1746.2, 1600.4, 1572.4, 1530.5, 1500.5, 1476.6, 1436.2, 1397.5, 1322.0, 1291.9, 1210.8, 1158.6, 1026.8, 945.7, 876.3, 778.9, 688.0; ^{1}H NMR(500 MHz, DMSO-d_6), δ: 5.15(s, 2H), 6.83 (d, 1H, J = 7.0 Hz), 7.33 (d, 2H, J = 4.0 Hz), 7.41 (broad s, 2H), 7.97 (d, 1H, J = 8.5 Hz), 8.45 (d, 1H, J = 7.5 Hz), 8.66 (s, 1H), 9.00 (s, 1H), 9.96 (s, 1H); ^{13}C NMR (125 MHz, DMSO-d_6), δ: 69.77, 109.78, 110.49, 115.40, 115.94, 121.52, 128.16, 128.30, 128.92, 128.98, 129.72, 132.69, 137.57,

137.59, 140.74, 149.84, 155.20, 158.3, 158.98; HR-ESI (Q-TOF) m/z: calculated for $C_{21}H_{17}IN_3O^+$ ($M+H^+$): 454.0416, found: 454.0422.

*Synthesis of 6-(4-(Dimethyl-amino)phenyl)-N-(3-((phenyl)methoxy)phenyl)-quinazolin-4-amine (**51**).*

2.8 grams (6.2 mmol) of N-(3-[(phenyl)methoxy]-phenyl)-6-iodo-quinazolin-4-amine (**62**), 2.5 g (12.4 mmol) of 4-(dimethylamino)phenyl-boronic acid hydrochloride, 250 mg of PPh_3, 10.0 mL of Et_3N, and 20.0 mL of dried DMF were placed in a 100 mL Schlenk flask with a stirrer bar under nitrogen purge. The reaction mixture was degassed for a further 30 min under a slow stream of nitrogen, at which point 250 mg of $Pd(OAc)_2$ was added. The reaction mixture was heated at 80 ºC for 24 h, cooled, poured into 300 mL of H_2O, and extracted with EtOAc (4 × 200 mL). The organic layer was dried with $MgSO_4$, filtered, and then concentrated under reduced pressure. It was purified over silica (100% CH_2Cl_2 to 100% EtOAc) followed by crystallization from 2-propanol and then methanol to afford light yellow powder of 6-(4-(Dimethyl-amino)phenyl)-N-(3-[(phenyl)methoxy]-phenyl)-quinazolin-4-amine (657 mg, 23.7 %); mp: 263 ℃ (dec); IR ν_{max}(cm^{-1}): 3207.2, 3061.9, 2796.5, 1938.1, 1607.2, 1567.2, 1526.2, 1499.5, 1455.3, 1424.9, 140.8, 1356.4, 1330.9, 1302.6, 1222.4, 1158.6, 1077.7, 1025.9, 970.6. 864.6, 780.1, 670.5; ^{1}H NMR(500 MHz, DMSO-d_6), δ: 2.99 (s, 6H), 5.15 (s, 2H), 6.81 (d, 1H, J = 7.0 Hz), 6.87 (d, 2H, J = 8.0 Hz), 7.30-7.36 (m, 2H), 7.40 (t, 2H, J = 6.5 Hz), 7.49 (broad s, 3H), 7.71 (s, 1H), 7.77-7.81 (m, 3H), 8.13 (d, 1H, J = 8.5 Hz), 8.57 (s, 1H), 8.72 (s, 1H), 9.82 (s, 1H); ^{13}C NMR (125 MHz, DMSO-d_6), δ: 40.48, 69.76, 109.68, 110.24, 113.02, 115.32, 116.04, 118.59, 126.86, 128.16, 128.29, 128.70, 128.91, 129.64, 131.51, 137.62, 138.84, 140.97, 148.76, 150.63, 154.15,

158.02, 158.96; HR-ESI (Q-TOF) m/z: calculated for $C_{29}H_{27}N_4O^+$ ($M+H^+$): 447.2158, found: 447.2176.

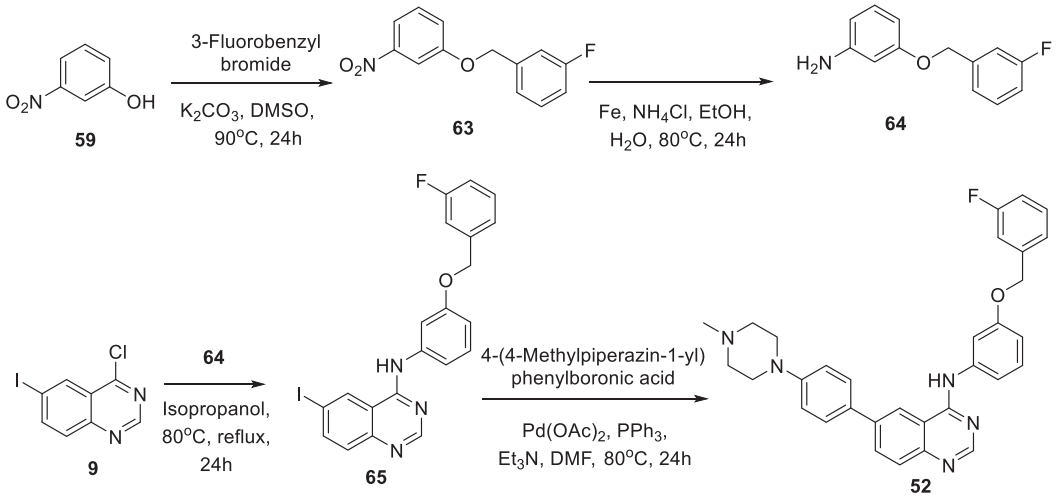

Scheme 5.4. Synthesis of **52**.

*Synthesis of 6-iodo-N-(4-((3-fluorophenyl)methoxy)phenyl)-quinazoline-4-amine (**65**).*

3.0 grams of 4-chloro-6-iodo-quinazoline, 4.2 g (19.3 mmol) of 4-[(3-fluorophenyl) methoxy]-benzenamine, and 2-propanol were added, vigorously stirred and heated at 80 ºC, overnight with a condenser. After 24 hours, it was cooled to room temperature, concentrated under reduced pressure, 50 mL of 1M KOH solution was added and stirred for 20 min, 100 mL of EtOAc was added, then organic solution was extracted three times through separation funnel and concentrated. It was crystallization from methanol, ethyl acetate to afford the off-white color powder of 6-iodo-N-(4-((3-fluorophenyl)methoxy)phenyl)-quinazoline-4-amine (500 mg, 10.6 %); mp: 165-166℃ ; IR ν_{max}(cm^{-1}): 3315.6, 2897.2, 2854.2, 1752.8, 1611.1, 1591.6, 1567.4, 1529.0, 1485.1, 1428.1, 1385.7, 1314.1, 1293.5, 1201.3, 1160.5, 1042.2, 953.6, 869.9, 781.9, 680.0; ^{1}H NMR(500 MHz, DMSO-d_6), δ: 5.16 (s, 1H), 6.80 (d, 1H, J = 8.0 Hz), 7.15 (t, 1H, J = 8.0 Hz), 7.29-7.33 (m, 3H), 7.43-7.48 (m, 2H), 7.55 (d, 1H, J = 9.0 Hz), 7.70

(s, 1H), 8.10 (dd, 1H, J = 8.5, 1.5 Hz), 8.62 (s, 1H), 9.01 (s, 1H), 9.81 (s, 1H); ^{13}C NMR (125 MHz, DMSO-d_6), δ: 68.89, 92.06, 109.49, 110.49, 114.60-114.78 (d, $J_{C,F}$= 22.5 Hz), 115.27, 117.43, 123.97-123.99 (d, $J_{C,F}$= 2.5 Hz), 129.72, 130.30, 130.91-130.98 (d, $J_{C,F}$= 8.75 Hz), 131.88, 140.53-140.59 (d, $J_{C,F}$= 7.5 Hz), 140.68, 141.82, 149.31, 155.24, 156.88, 158.68, 161.71-163.65 (d, $J_{C,F}$= 242.5 Hz); HR-ESI (Q-TOF) m/z: calculated for $C_{21}H_{16}IFN_3O^+$ ($M+H^+$): 472.0322, found: 472.0310.

*Synthesis of 6-(4-(4-Methylpiperazin-1-yl)phenyl)-N-(4-((3-fluorophenyl)methoxy)phenyl)-quinoline-3-carbnitrile-4-amine (**52**).*

267 milligrams (0.57 mmol) of 6-iodo-N-(4-((3-fluorophenyl)methoxy)phenyl)-quinazoline-4-amine (**65**), 225 mg (1.0 mmol) of 4-(4-Methylpiperazin-1-yl)phenylboronic acid, 30 mg of PPh_3, 1 mL of Et_3N, and 3 mL of DMF were placed in a 50 mL Schlenk flask with a stirrer bar under nitrogen purge. The reaction mixture was degassed for a further 30 min under a slow stream of nitrogen, at which point 30 mg of $Pd(OAc)_2$ was added. The reaction mixture was heated at 80 ºC for 24 h, cooled, filtered through filter paper and eluted solution was added into 50 mL of H_2O directly, and ethyl acetate was poured onto funnel to wash the residues. Water and ethyl acetate solution mixture went through extraction with three times with 200 mL of ethyl acetate each. The organic layer was dried with $MgSO_4$, filtered, and then concentrated under reduced pressure. It was purified over silica (100 % EtOAc to 100% MeOH), followed by crystallization from methanol, ethyl acetate multiple times to afford the white powder of 6-(4-(4-Methylpiperazin-1-yl)phenyl)-N-(4-((3-fluorophenyl)methoxy)phenyl)-quinoline-3-carbnitrile-4-amine (87.0 mg, 29.4 %); mp: 284-285℃ (dec); IR ν_{max}(cm^{-1}): 3262.6, 3061.0, 2939.3, 2837.2, 2792.0, 1932.8,

1601.9, 1569.9, 1524.1, 1491.7, 1449.4, 1423.2, 1401.0, 1359.8, 1327.8, 1292.8, 1237.8, 1158.6, 1080.7, 1038.8, 972.7, 865.8, 774.3, 692.6; ^{1}H NMR(500 MHz, DMSO-d_6), δ: 2.23 (s, 3H), 2.47 (broad s, 4H), 3.23 (broad s, 4H), 5.17 (s, 1H), 6.81 (d, 2H, J = 8.0 Hz), 7.07 (d, 2H, J = 7.5 Hz), 7.153 (t, 1H, , J = 7.5 Hz), 7.31-7.34 (m, 3H), 7.435-7.49 (m, 2H), 7.71 (s, 1H), 7.77 (d, 2H, J = 9.0 Hz), 7.80 (d, 1H, J = 8.5 Hz), 8.13 (d, 1H, J = 8.5 Hz), 8.57 (s, 1H), 8.75 (s, 1H), 9.84 (s, 1H); ^{13}C NMR (125 MHz, DMSO-d_6 + TFA), δ: 42.57, 45.60, 52.58, 68.98, 111.18, 112.17, 114.61-114.78 (d, $J_{C,F}$= 21.25 Hz), 115.00-115.16 (d, $J_{C,F}$= 20.0 Hz), 115.09, 116.50, 116.86, 120.07, 123.98-124.00 (d, $J_{C,F}$= 2.5 Hz), 124.12, 128.32, 129.79, 129.97, 130.93-131.00, (d, $J_{C,F}$= 8.75 Hz), 133.37, 139.36, 139.54, 140.37-140.43 (d, $J_{C,F}$= 7.5 Hz), 142.42, 150.02, 152.34, 158.76, 159.51, 161.72-163.66 (d, $J_{C,F}$= 242.5 Hz); HR-ESI (Q-TOF) m/z: calculated for $C_{32}H_{31}FN_5O^+$ ($M+H^+$): 520.2513, found: 520.2509.

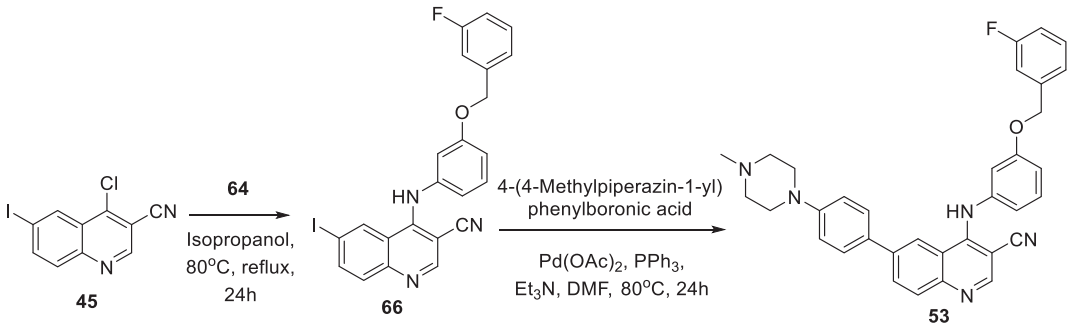

Scheme 5.5. Synthesis of **53**.

*Synthesis of 6-bromo-N-(4-((3-fluorophenyl)methoxy)phenyl)-quinoline-3-carbnitrile-4-amine (**66**).*

1.1 grams of **45**, 1.1 g (5.1 mmol) of 4-[(3-fluorophenyl)methoxy]-benzenamine, and 2-propanol were added, vigorously stirred and heated at 80 °C, overnight with a condenser. After 24 hours, it was cooled to room temperature, concentrated under

reduced pressure, 40 mL of 1M KOH solution was added and stirred for 20 min, 100 mL of EtOAc was added, then organic solution was extracted three times through separation funnel and concentrated. It was purified over silica (100 % DCM to 100% EtOAc), followed by crystallization in methanol, ethyl acetate multiple times to afford yellow powder of 6-bromo-N-(4-((3-fluorophenyl)methoxy)phenyl)-quinoline-3-carbnitrile-4-amine (558 mg, 28.2 %); mp: 74-76℃ ; IR ν_{max}(cm^{-1}): 3292.2, 3066.5, 2937.5, 2212.9, 1723.2, 1584.0, 1557.1, 1524.7, 1487.4, 1406.6, 1385.9, 1255.1, 1203.7, 1178.1, 1079.2, 1036.8, 941.6, 865.1, 827.6, 743.6, 681.2; ^{1}H NMR(500 MHz, DMSO-d_6), δ: 5.15 (s, 1H), 6.91-6.92 (m, 2H), 6.95 (s, 1H), 7.13 (t, 1H, J = 8.0 Hz), 7.26-7.29 (m, 2H), 7.31 (t, 1H, J = 8.5 Hz), 7.41 (m, 1H), 7.86 (d, 1H, J = 8.5 Hz), 7.96 (d, 1H, J = 7.5 Hz), 8.61 (s, 1H), 8.75 (s, 1H), 9.89 (s, 1H); ^{13}C NMR (125 MHz, DMSO-d_6), δ: 68.86, 89.50, 111.08, 112.98, 114.48-114.65 (d, $J_{C,F}$ = 21.25 Hz), 114.93-115.09 (d, $J_{C,F}$= 20.0 Hz), 116.91, 117.28, 120.05, 121.32, 123.84-123.86 (d, $J_{C,F}$= 2.5 Hz), 125.91, 130.36, 130.90-130.96 (d, $J_{C,F}$= 7.5 Hz), 132.04, 135.35, 140.36-140.42 (d, $J_{C,F}$= 7.5 Hz), 140.82, 147.92, 150.56, 153.97, 159.11, 161.70-163.64 (d, $J_{C,F}$ = 242.5 Hz); HR-ESI (Q-TOF) m/z: calculated for $C_{23}H_{16}BrFN_3O^+$ ($M+H^+$): 450.0440, found: 450.0416.

Synthesis of 6-(4-(4-Methylpiperazin-1-yl)phenyl)-N-(4-((3-fluorophenyl) methoxy)phenyl)-quinoline-3-carbnitrile-4-amine (53).

125 milligrams (0.28 mmol) of 6-bromo-N-(4-((3-fluorophenyl)methoxy)phenyl)-quinoline-3-carbnitrile-4-amine, 65 mg (0.29 mmol) of 4-(4-Methylpiperazin-1-yl)phenylboronic acid , 8 mg of PPh_3, 1 mL of Et_3N, and 3 mL of DMF were placed in a 50 mL Schlenk flask with a stirrer bar under nitrogen purge. The reaction mixture

was degassed for a further 30 min under a slow stream of nitrogen, at which point 80 mg of $Pd(OAc)_2$ was added. The reaction mixture was heated at 80 ^oC for 24 h, cooled, filtered through filter paper and eluted solution was added into 50 mL of H_2O directly, and ethyl acetate was poured onto funnel to wash the residues. Water and ethyl acetate solution mixture went through extraction with three times with 100 mL of ethyl acetate each. The organic layer was dried with $MgSO_4$, filtered, and then concentrated under reduced pressure. It was purified over silica (100 % EtOAc to 100% MeOH), followed by crystallization in methanol, ethyl acetate multiple times to afford yellow powder of 6-(4-(4-Methylpiperazin-1-yl)phenyl)-N-(4-((3-fluorophenyl)methoxy)phenyl)-quinoline-3-carbnitrile-4-amine (20.0 mg, 13.1 %); mp: 160-162℃ (dec); IR ν_{max}(cm^{-1}): 3300.2, 3066.5, 2972.4, 2939.5, 2838.1, 2803.4, 2213.3, 1604.2, 1586.8, 1520.4, 1498.4, 1440.7, 1377.9, 1290.8, 1237.1, 1200.6, 1139.4, 1077.6, 1004.2, 944.4, 923.8, 884.1, 770.7, 681.0; ^{1}H NMR(500 MHz, DMSO-d_6), δ: 2.23 (s, 3H), 2.47 (broad s, 4H), 3.23 (broad s, 4H), 5.17 (s, 2H), 6.91 (d, 2H, J = 8.0 Hz), 6.97 (s, 1H), 7.06 (d, 2H, J = 8.0 Hz), 7.14 (t, 1H, , J = 7.5 Hz), 7.26-7.29 (m, 2H), 7.32 (t, 1H, , J = 8.0 Hz), 7.41-7.45 (m, 1H), 7.77 (d, 2H, J = 9.0 Hz), 7.95 (d, 1H, J = 8.5 Hz), 8.15 (d, 1H, J = 8.5 Hz), 8.54 (s, 1H), 8.68 (s, 1H), 9.89 (s, 1H); ^{13}C NMR (125 MHz, DMSO-d_6 + TFA), δ: 42.56, 45.49, 52.57, 68.99, 87.39, 113.27, 114.48-114.66 (d, $J_{C,F}$= 22.5 Hz), 114.86, 115.00-115.17 (d, $J_{C,F}$= 21.25 Hz), 115.22, 116.44, 119.30, 119.39, 119.92, 123.85-123.87 (d, $J_{C,F}$= 2.5 Hz), 124.01, 128.39, 129.16, 130.72, 130.94-131.01 (d, $J_{C,F}$= 8.75 Hz), 133.01, 138.99, 139.49, 139.73, 140.16-140.22 (d, $J_{C,F}$= 7.5 Hz), 150.21, 150.25, 154.38, 159.19, 161.71-163.65 (d, $J_{C,F}$= 242.5 Hz); HR-ESI (Q-TOF) m/z: calculated for $C_{34}H_{31}FN_5O^+$ ($M+H^+$): 544.2513, found: 544.2518.

5.3 Optical spectroscopy

Most of all, UV-Vis and fluorescence spectra of compounds **49-51** were measured in chloroform to investigate their optical properties quantitatively (Figure 5.3). The meta-substitution of benzyloxy ether (**51**) resulted enhancement of fluorescence than para and di-substitution. Also, the compound **51** exhibited the responsiveness on solvent polarity (Figure 5.4, Table 5.1). Based on that results, the solubility optimized meta-substituent probes (**52-53**) were generated. The optical properties of meta-QA2 (**52**) and meta-CQ2 (**53**) were characterized and compared with QA2 (**6**) and CQ2 (**40**). Both of meta-QA2 (**52**) and meta-CQ2 (**53**) exhibited enhanced emissions than QA2 (**6**) and CQ2 (**40**), and responsive on polarity changes.

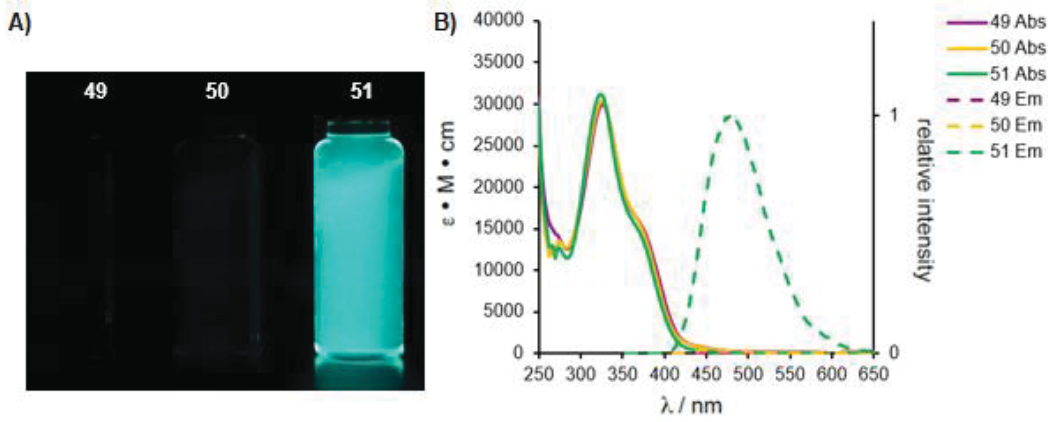

Figure 5.3. A) Chloroform solutions of compounds **49-51** in 5 μM under UV illumination at 354 nm. B) Absorption and emission spectra of **49-51** in chloroform shows that meta-substitution of benzyloxy ether group on Type II pharmacophore arm was resulted in enhancement of fluorescence than para- and di- substitution derivatives (**49**, **50**).

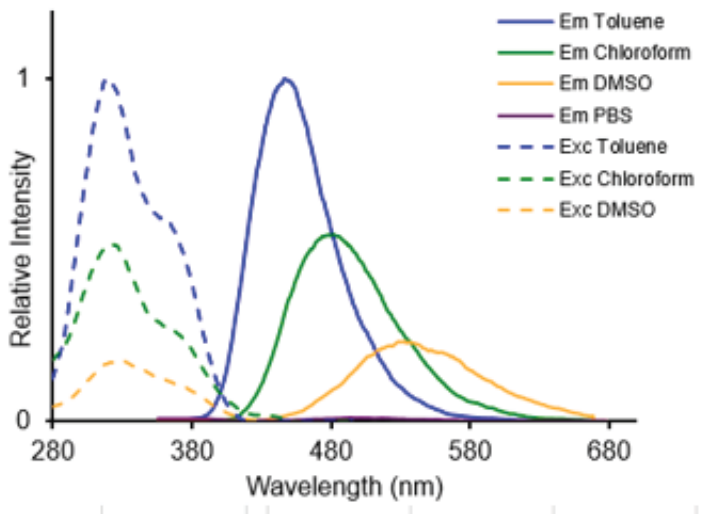

Figure 5.4. Absorption and emission spectra of compound **51** in several solvents demonstrating the sensitivity of the excited state to solvent polarity.

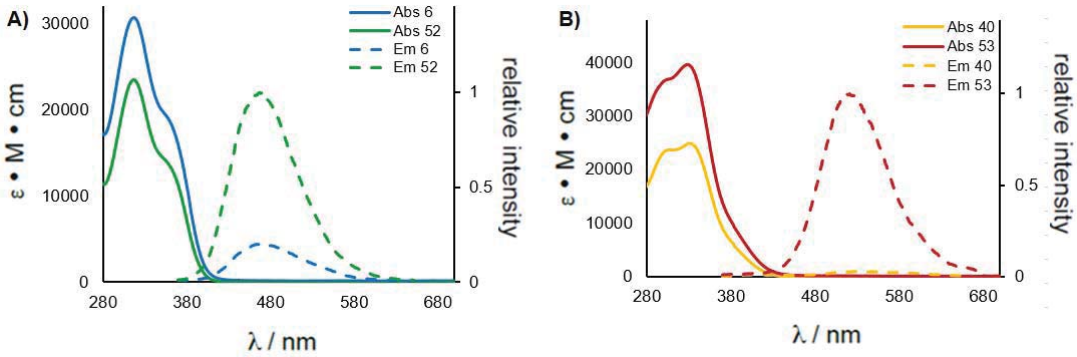

Figure 5.5. A) Absorption and emission spectra of QA2 (**6**) and meta-QA2 (**52**) in chloroform. B) Absorption and emission spectra of CQ2 (**40**) and meta-CQ2 (**53**) in chloroform.

Table 5.1. Photophysical parameters of **49**, **50**, **51** in solution.

Solvent / **49**	PhMe	$CHCl_3$	MeCN	MeOH	IPA	DMSO	PBS
$\lambda_{max,\ abs}$ (nm)	324	327	325	326	324	330	326
ε ($M^{-1}\ cm^{-1}$)	29300	30000	32200	32500	33300	32100	24200
$\lambda_{max,\ FL}$ (nm)	380	452	599	378	380	379	403
Φ_{FL}[a]	0.002	0.001	0.003	0.002	0.001	0.003	0.02
Solvent / **50**	PhMe	$CHCl_3$	MeCN	MeOH	IPA	DMSO	PBS
$\lambda_{max,\ abs}$ (nm)	323	325	324	325	324	330	332
ε ($M^{-1}\ cm^{-1}$)	30700	30300	32800	30500	30500	33400	25900
$\lambda_{max,\ FL}$ (nm)	477	445	500	380	544	540	489
Φ_{FL}[a]	0.01	0.001	0.0003	0.003	0.002	0.003	0.009
Solvent / **51**	PhMe	$CHCl_3$	MeCN	MeOH	IPA	DMSO	PBS
$\lambda_{max,\ abs}$ (nm)	322	324	322	323	322	327	330
ε ($M^{-1}\ cm^{-1}$)	31100	31100	33500	31800	30700	32300	26200
$\lambda_{max,\ FL}$ (nm)	450	474	506	381	610	525	525
Φ_{FL}[a]	0.56	0.36	0.07	0.003	0.02	0.16	0.008

[a] ± 10%

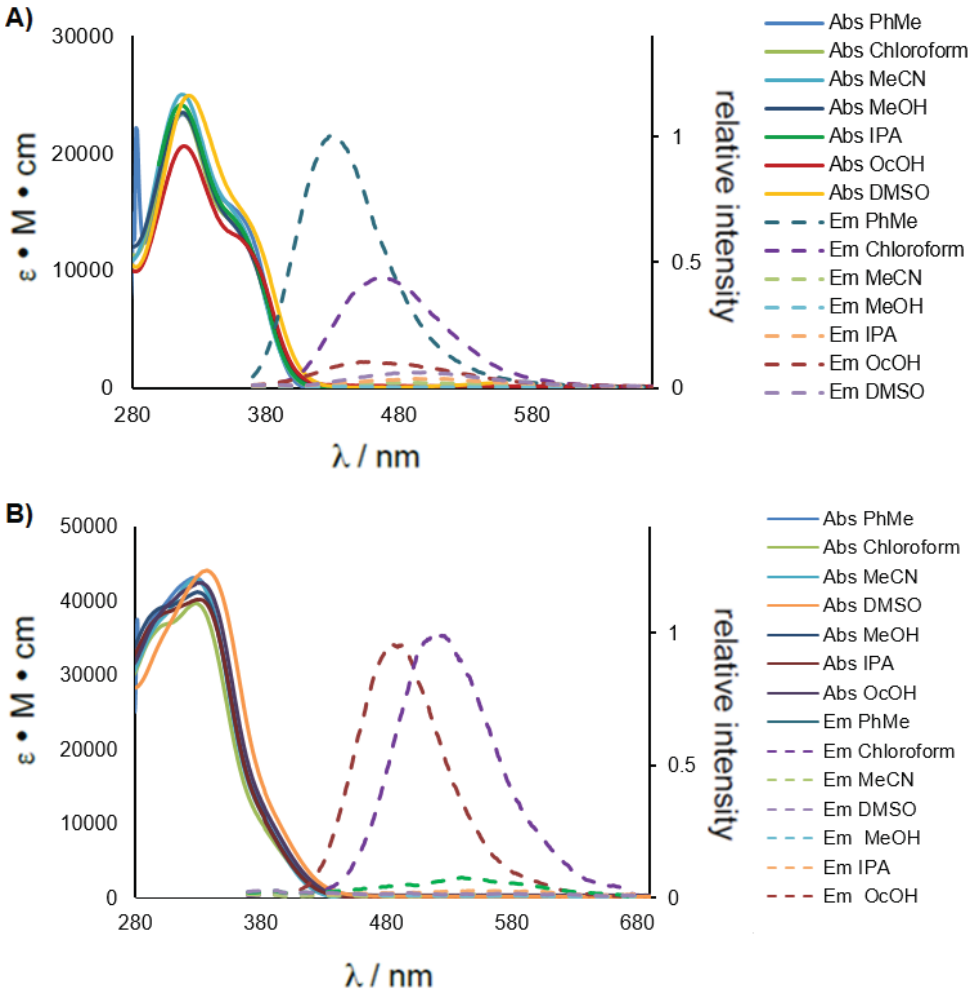

Figure 5.6. A) Absorption and emission spectra of meta-QA2 (**52**) in various solvents. B) Absorption and emission spectra of meta-CQ2 (**53**) in various solvents. Both compounds exhibited the sensitivity of the excited state to solvent polarity.

Table 5.2. Photophysical parameters of **52**, **53** in solution.

Solvent / **52**	PhMe	$CHCl_3$	MeCN	MeOH	IPA	DMSO	PBS
$\lambda_{max, abs}$ (nm)	317	317	316	317	317	322	320
ε (M^{-1} cm^{-1})	23300	23400	25000	23400	24100	24900	21100
$\lambda_{max, FL}$ (nm)	460.5	471	522	402	577	508.5	404.5
Φ_{FL}[a]	0.44	0.25	0.01	0.006	0.03	0.04	0.04
Solvent / **53**	PhMe	$CHCl_3$	MeCN	MeOH	IPA	DMSO	PBS
$\lambda_{max, abs}$ (nm)	327	328	329	330	330	338	334
ε (M^{-1} cm^{-1})	43100	39700	42800	41200	40200	44100	34600
$\lambda_{max, FL}$ (nm)	502	537.5	560.5	465	394.5	394	534.5
Φ_{FL}[a]	0.09	0.11	0.002	0.003	0.006	0.004	0.01

[a] ± 10%

References

1. Wieduwilt, M. J.; Moasser, M. M., The epidermal growth factor receptor family: Biology driving targeted therapeutics. *Cell. Mol. Life Sci*. **2008**, *65*, 1566-1584.

2. Bertelsen, V.; Stang, E., The mysterious ways of ERBB2/HER2 trafficking. *Membranes*. **2014**, *4*, 424-446.

3. Warren, C. M.; Landgraf, R., Signaling through ERBB receptors: multiple layers of diversity and control. *Cell. Signal*., **2006**, *18*, 923-933.

4. Burgess, A. W.; Cho, HS.; Elgenbrot, C.; Ferguson, K. M.; Garrett, T. P.; Leahy, D. J.; Lemmon, M. A.; Sliwkowski, M. X.; Ward, C. W.; Yokoyama, S., An open-and-shut case? Recent insights into the activation of EGF/ErbB receptors. *Mol. Cell*. **2003**, *12*, 541-552.

5. Kumar, A.; Petri, E. T.; Halmos, B.; Boggon, T. J., Structure and clinical relevance of the epidermal growth factor receptor in human cancer. *J. Clin. Oncol*. **2008**, *26*, 1742-1751.

6. Alroy, I.; Yarden, Y., The ErbB signaling network in embryogenesis and oncogenesis: signal diversification through combinatorial ligand-receptor interaction. *FEBS Letters*. **1997**, *410*, 83-86.

7. Lemmon, M. A., Ligand-induced ERBB receptor dimerization. *Exp. Cell Res.* **2009**, *315*, 638-648.

8. Brossier, N. M.; Byer, S. J.; Peavler, L. T.; Carroll, S. L., ERBB membrane tyrosine kinase receptors: analyzing migration in a high complex signaling system. *Protein Kinase Technologies, Neuromethods*. **2012**, *68*, 105-131.

9. Wiley, H. S., Trafficking of the ERBB receptors and its influence on signaling. *Exp. Cell Res.* **2003**, *284*, 78-88.

10. Ma, X.; Ma, C. X., Wang, J. Endometrial carcinogenesis and molecular signaling pathways. *Am. J. Mol. Biol*. **2014**, *4*, 134-149.

11. Graus-Porta, D.; Beerli, R. R.; Hynes, N. E., Single-chain antibody-mediated intercellular retention of ERBB-2 impairs neu differentiation factor and epidermal growth factor signaling. *Cell. Biol*. **1995**, *15*, 1182-1191.

12. Gollamudi, J.; Parvani, J. G.; Vinayak, S., Neoadjuvant therapy for early-stage breast cancer: the clinical utility of pertuzumab. *Cancer Manag Res*. **2016**, *8*, 21-31.

13. Moasser, M. M., The oncogene HER2; Its signaling and transforming functions and its role in human cancer pathogenesis. *Oncogene*. **2007**, *26*, 6469-6487.

14. Sui, W.; Ou, M,; Chen, J.; Wan, Y.; Peng, H.; Qi, M.; Huang, H.; Dai, Y., Comparison of immunohistochemistry (IHC) and fluorescence in situ hybridization (FISH) assessment for Her-2 status in breast cancer. *World J Surg Oncol*. **2009**, *7*:83.

15. Qian, X.; Wen, H. Y.; Yang, Y.; Gu, F.; Guo, X.; Liu, F.; Zhang, L.; Zhang, X., Assessment of dual-probe HER-2 fluorescent in situ hybridization in breast cancer by the 2013 ASCO/CAP guidelines produces more equivocal results than that by the 2007 ASCO/CAP guidelines. *Breast Cancer Res Treat*. **2016**, *159*, 31-39.

16. Portier, B. P.; Wang, Z.; Downs-Kelly, E.; Rowe, J.; Patil, D.; Lanigan, C.; Budd, G. T.; Hicks, D. G.; Rimm, D. L.; Tubbs, R., Delay to formalin fixation 'cold ischemia time': effect on ERBB2 detection by in-situ hybridization and immunohistochemistry. *Modern Pathology*. **2013**, *26*, 1-9.

17. Perez, E. A.; Cortes, J.; Gonzalez-Angulo, A. M.; Bartlett, J. M. S., HER2 testing: Current status and future directions. *Cancer Treatment Reviews*. **2014**, *40*, 276-284.

18. Mukohara, T., Mechanisms of resistance to anti-human epidermal growth factor receptor 2 agents in breast cancer. *Cancer Sci*. **2011**, *102*, 1-8.

19. O'Brien, N. A.; Canonici, A.; Howe, K.; McDermott, M. S. J.; Colline, D. M.; Browne, B. C.; Crown, J.; O'Donovan, N., HER2 targeted monoclonal antibodies and tyrosine kinase Inhibitors. *Frontiers in Anti-Cancer Drug Discovery*, **2014**, *4*, 293-382.

20. Redfern, A.; Burslem, K.; Woodward, N.; Beith, J.; McCarthy, N.; De Boer, R.; Bell, R., Hormone receptor positive, HER2 negative metastatic breast cancer: Future treatment landscape. *Asia. Pac. J. Clin. Oncol*. **2016**, *12(S1)*, 19-31.

21. Fedele, P.; Orlando, L.; Schiavone, P.; Calvani, N.; Caliolo, C.; Quaranta, A.; Nacci, A.; Cinieri, S., Recent advances in the treatment of hormone receptor positive HER2 negative metastatic breast cancer. *Crit Rev Oncol Hematol*. **2015**, *94*, 291-301.

22. Dressler, L. G.; Thor, A. D., HER2 testing: laboratory, technical and clinical consideration. *Breast Disease*. **2000**, *11*, 78-87.

23. Wolff, A. C.; Hammond, E. H.; Schwartz, J. N.; Hagerty, K. L.; Allred, D. C.; Cote, R. J.; Dowsett, M.; Fitzgibbons, P. L.; Hanna, W. M.; Langer, A.; McShane, L. M.; Paik, S.; Pegram, M. D.; Perez, E. A.; Press, M. F.; Rhodes, A.; Sturgeon, C.; Taube, S. E.; Tubbs, R.; Vance, G. H.; Van De Vijver, M.; Wheeler, T. M.; Hayes, D. F., American society of clinical oncology/college of american pathologists guideline recommendations for human epidermal growth factor receptor 2 testing in breast cancer. *Arch. Pathol. Lab. Med*. **2007**, *131*, 18-43.

24. Wolff, A. C.; Hammond, E. H.; Hicks, D. G.; Dowsett, M.; McShane, L. M.; Allison, K. H.; Allred, D. C.; Barlett, J. M. S.; Bilous, M.; Fizgibbons, P.; Hanna, W.; Jenkin, R. B.; Mangu, P. B.; Paik, S.; Perez, E. A.; Press, M. F.; Spears, P. A.; Vance, G. H.; Viale, G.; Hayes, D. F., Recommendations for human epidermal growth factor receptor 2 testing in breast cancer: american society of clinical oncology/college of american pathologists clinical practice guideline update. *J. Clin. Oncol*. **2013**, *31*, 3997-4014.

25. Lee, H.; Liu, W.; Brown, A. S.; Landgraf, R.; Wilson, J. N., Fluorescent kinase probes enabling identification and dynamic imaging of HER2(+) Cells. *Anal. Chem*. **2016**, *88*, 11310-11313.

26. Sicard, R.; Dhuguru, J.; Liu, W.; Patel, N.; Landgraf, R.; Wilson, J. N., A fluorescent reporter of ATP binding-competent receptor kinases. *Bioorg. Med. Chem. Lett*. **2012**, *22*, 5532-5535.

27. Yun, C. Boggon, T. J.; Li, Y.; Woo, M. S.; Greulich, H.; Meyerson, M.; Eck, M. J., Structures of lung cancer-derived EGFR mutants and inhibitor complexes: mechanism of activation and insights into differential inhibitor sensitivity. *Cancer Cell*. **2007**, *11*, 217-227.

28. Wood, E. R.; Truesdale, A. T.; McDonald, O. B.; Yuan, D.; Hassell, A.; Dickerson, S. H.; Ellis, B.; Pennisi, C.; Horne, E.; Lackey, K.; Alligood, K. J.; Rusnak, D. W.; Glimer, T. M. Schewchuk, L., A unique structure for epidermal growth factor receptor bound to GW572016 (Lapatinib): relationships among protein conformation, inhibitor off-rate, and receptor activity in tumor cells. *Cancer Res*. **2004**, *64*, 6652-6659.

29. Dhuguru, J.; Liu, W.; Gonalez, W. G.; Babinchak, M.; Miksovska, J.; Landgraf, R.; Wilson, J. N., Emission tuning of fluorescent kinase inhibitors: conjugation length and substituent effects. *J. Org. Chem*. **2014**, *79*, 4940-4947.

30. Huang, D.; Zhou, T.; Lafleur, K.; Nevado, C.; Caflisch, A., Kinase selectivity potential for inhibitors targeting the ATP binding site: a network analysis. *Bioinformatics*, **2010**, *26*, 198-204.

31. Grabowski, Z. R.; Rotkiewicz, K., Structural changes accompanying intramolecular electron transfer: focus on twisted intramolecular charge-transfer states and structures. *Chem. Rev*. **2003**, *103*, 3899-4032.

32. Sasaki, S.; Drummen, G. P. C.; Konishi, G., Recent advances in twisted intramolecular charge transfer (TICT) fluorescence and related phenomena in materials chemistry. *J. Mater. Chem. C*. **2016**, *4*, 2731-2743.

33. Rewcastle, G. W.; Denny, W. A.; Bridges, A. J.; Zhou, H.; Cody, D. R.; McMichael, A.; Fry, D. W., Tyrosine kinase inhibitors. 5. Synthesis and structure-activity relationships for 4-[(phenylmethyl)amino]-and 4-(phenylamino)quinazolines as potent adenosine 5'-triphosphate binding site inhibitors of the tyrosine kinase domain of the epidermal growth factor receptor. *J. Med. Chem*. **1995**, *38*, 3482-3487.

34. Liu, Y.; Gray, N. S., Rational design of inhibitors that bind to inactive kinase conformation. *Nat. Chem. Biol*. **2006**, *2*, 358-364.

35. Sardon, T.; Cottin, T.; Xu, J.; Giannis, A.; Vernos, I., Development and biological evaluation of a novel aurora A kinase inhibitor. *ChemBioChem*. **2009**, *10*, 464-478.

36. Gaul, M. D.; Guo, Y.; Affleck, K.; Cockerill, G. S.; Gilmer, T.M.; Griffin, R. J.; Guntrip, S.; Keith, B. R.; Knight, W. B.; Mullin, R. J.; Murray, D. M.; Rusnak, D. W.; Smith, K; Tadepalli, S.; Wood, E. R.; Lackey, K., Discovery and biological evaluation of potent dual ErbB-2/EGFR tyrosine kinase inhibitors: 6-thiazolylquinazolines. *Bioorg. Med. Chem. Lett*. **2003**, *13*, 637-640.

37. Mahboobi, S.; Sellmer, A.; Winkler, M.; Eichhorn, E.; Pongratz, H.; Ciossek, T.; Baer, T.; Maier, T.; Beckers, T. J., Novel chimeric histone deacylase inhibitors: A series of lapatinib hybrides as potent inhibitors of epidermal growth factor receptor (EGFR), human epidermal growth factor receptor 2 (HER2), and histone deacylase activity. *J. Med. Chem*. **2010**, *53*, 8546-8555.

38. Lieber, S.; Scheer, F.; Meissner, W.; Naruhn, S.; Adhikary, T.; Müller-Brüsselbach, S; Diederich, W. E.; Müller, R., (Z)-2-(2-bromophenyl)-3-{[4-(1-methyl-piperazine)amino]phenyl}acrylonitrile (DG172): an orally bioavailable PPARβ/δ-selective ligand with inverse agonistic properties. *J. Med. Chem*. **2012**, *55*, 2858-2868.

39. Reichardt, C., Solvatochromic dyes as solvent polarity indicator. *Chem. Rev*. **1994**, *94*, 2319-2358.

40. Berlman, I., Handbook of fluorescence spectra of aromatic molecules. 2nd ed.; Academic Press: New York, 1971

41. Leo, A.; Hansch, C.; Elkins, D., Partition coefficients and their uses. *Chem. Rev*. **1971**, *71*, 525-616.

42. Lipinski, C. A.; Lombardo, F.; Dominy, B. W.; Feeney, P. J., Experimental and computational approaches to estimate solubility and permeability in drug discovery and development settings. *Adv. Drug. Deliv. Rev*. **2001**, *46*, 3-26.

43. Ertl, P.; Rohde, B.; Selzer, P., Fast calculation of molecular polar surface area as a sum of fragment-based contributions and its application to the prediction of drug transport properties. *J. Med. Chem*. **2000**, *43*, 3714-3717.

44. Potts, R. O.; Guy, R. H., Predicting skin permeability. *Pharm Res*. **1992**, *5*, 633-669.

45. Yang, Z.; Cao, J.; He, Y.; Yang, J.; Kim, T.; Peng, X.; Kim, J., Macro-/micro-environment-sensitive chemo-sensing and biological imaging. *Chem. Soc. Rev*. **2014**, *43*, 4563-4601.

46. Park, E.; Baron R.; Landgraf, R., Higher-order association states of cellular ERBB3 probed with photo-cross-linkable aptamers. *Biochem*. **2008**, *47*, 11992.

47. Schindelin, J; Arganda-Carreras, I.; Frise, E.; Kaynig, V.; Longair, M.; Pietzsch, T.; Preibisch, S.; Rueden, C.; Saalfeld, S.; Schmid, B.; Tinevez, J.; White, D. J.; Hartenstein, V.; Eliceiri, K.; Tomancak, P.; Cardona, A., Fiji: an open-source platform for biological-image analysis. *Nature Meth*. **2012**, *9*, 676-682.

48. Kleiman, L B.; Maiwald, T.; Conzelmann, H.; Lauffenburger, D. A.; Sorger, P. K., Rapid phospho-turnover by receptor tyrosine kinases impacts downstream signaling and drug binding. *Molecular Cell*. **2011**, *43*, 723-737.

49. Gerling, N.; Culmsee, C.; Klumpp, S.; Krieglstein, J., The tyrosine phosphatase inhibitor orthovanadate mimics NGF-induced neuroprotective signaling in rat hippocampal neurons. *Neurochem. Int*. **2004**, *44*, 505-520.

50. Kim, J.H.; Do, H.J.; Wang, W.H.; Macháty, Z.; Han, Y.M.; Day, B.N.; Prather, R.S., A protein tyrosine phosphatase inhibitor, sodium orthovanadate, causes parthenogenetic activation of pig oocytes via an increase in protein tyrosine kinase activity. *Biol. Reprod.* **1999**, *61*, 900-905.

51. Reynolds A. R.; Tischer, C.; Verveer, P. J.; Rocks, O.; Bastiaens P. I., EGFR activation coupled to inhibition of tyrosine phosphatases causes lateral signal propagation. *Nat. Cell Biol.* **2003**, *5*, 447-453.

52. Yuan, L.; Lin, W.; Zheng, K.; He, L.; Huang, W., Far-red to near infrared analyte-responsive fluorescent probes based on organic fluorophore platforms for fluorescence imaging. *Chem. Soc. Rev*. **2013**, *42*, 622-661.

53. Gong, Y.; Zhang, X.; Mao, G.; Su, L.; Meng, H.; Tan, W.; Feng, S.; Zhang, G., A unique approach toward near-infrared fluorescent probes for bioimaging with remarkably enhanced contrast. *Chem. Sci*. **2016**, *7*, 2275-2285.

54. Petrov, K. G.; Zhang, Y. M.; Carter, M.; Cockerill, G. S.; Dickerson, S. Gauthier, C. A.; Guo, Y.; MooK, R. A. Jr.; Rusnak, D. W.; Walker, A. L.; Wood. E. R.; Lackey, K. E., Optimization and SAR for dual ErbB-1/ErbB-2 tyrosine kinase inhibition in the 6-furanylquinazoline series. *Bioorg. Med. Chem. Lett*. **2006**, *16*, 4686-4691.

55. Krueger, A. T.; Kool, E. T., Fluorescence of size-expanded DNA bases: reporting on DNA sequence and structure with an unnatural genetic set. *J. Am. Chem. Soc*. **2008**, *130*, 3989-3999.

56. Lee, A. H. F.; Kool, E. T., Exploring the limits of DNA size: Naphtho-homologated DNA based and pairs. *J. Am. Chem. Soc*. **2006**, *128*, 9219-9230.

57. Okamoto, A.; Tanaka, K.; Fukuta, T.; Saito, I., Cytosine detection by a fluorescein-labeled probe containing base-discriminating fluorescent nucleobase. *ChemBioChem*. **2004**, *5*, 958-963.

58. Godde, F.; Toulme, J.; Moreau, S., Benzoquinazoline derivatives as substitutes for thymine in nucleic acid complexes. Use of fluorescence emission of benzo[*g*]quinazoline-2,4-(1*H*,3*H*)-dione in probing duplex and triplex formation. *Biochemistry*, **1998**, *37*, 13765-13775.

59. Marenich, A. V.; Cramer, C. J.; Truhlar, D. G., Universal solvation model based on solute electron density and on a continuum model of the solvent defined by the bulk dielectric constant and atomic surface tensions. *J. Phys. Chem. B*. **2009**, *113*, 6378-6396.

60. Frisch, M. J.; Trucks, W.; Schlegel, H. B.; Scuseria, G. E.; Robb, M. A.; Cheeseman, J. R.; Scalmani, G.; Barone, V.; Mennucci, B.; Petersson, G. A.; Nakatsuji, H.; Caricato, M.; Li, X.; Hratchian, H. P.; Izmaylov, A. F.; Bloino, J.; Zheng, G.; Sonnenberg, J. L.; Hada, M.; Ehara, M.; Toyota, K.; Fukuda, R.; Hasegawa, J.; Ishida, M.; Nakajima, T.; Honda, Y.; Kitao, O.; Nakai, H.; Vreven, T.; Montgomery, Jr., J. A.; Peralta, J. E.; Ogliaro, F.; Bearpark, M.; Heyd, J. J.; Brothers, E.; Kudin, K. N.; Staroverov, V. N.; Kobayashi, R.; Normand, J.; Raghavachari, K.; Rendell, A.; Burant, J. C.; Iyengar, S. S.; Tomasi, J.; Cossi, M.; Rega, N.; Millam, J. M.; Klene, M.; Knox, J. E.; Cross, J. B.; Bakken, V.; Adamo, C.; Jaramillo, J.; Gomperts, R.; Stratmann, R. E.; Yazyev, O.; Austin, A. J.; Cammi, R.; Pomelli, C.; Ochterski, J. W.; Martin, R. L.; Morokuma, K.; Zakrzewski, V. G.; Voth, G. A.; Salvador, P.; Dannenberg, J. J.; Dapprich, S.; Daniels, A. D.; Farkas, Ö.; Foresman, J. B.; Ortiz, J. V.; Cioslowski, J.; Fox, D. J., *Gaussian 09, Revision A.1*, (**2009**) Gaussian, Inc., Wallingford CT.

61. Yanai, T.; Tew, D. P.; Handy, N. C., A new hybrid exchange-correlation functional using the coulomb-attenuating method (CAM-B3LYP). *Chem. Phys. Lett.* **2004**, *393*, 51-57.

62. Pitter, D. R. G.; Brown, A. S.; Baker, J. D.; Wilson, J. N., One probe, two-channel imaging of nuclear and cytosolic compartments with orange and red emissive dyes. *Org. Biomol. Chem.* **2015**, *36*, 9477-9484.

63. Chabner, B. A.; Robers, T. G., Chemotherapy and the war on cancer. *Nat. Rev. Cancer.* **2005**, *5*, 65-72.

64. Bagnyukova, T.; Serebriiskii, I. G.; Zhou, Y.; Hopper-Borge, E. A.; Golemis, E. A.; Astsaturov, I., Chemotherapy and signaling. *Cancer Biol. Ther*. **2010**, *10*, 839-853.

65. McGranahan, N.; Swanton, C., Biological and therapeutic impact of intratumor heterogeneity in cancer. *Cancer Cell*. **2015**, *27*, 15-26.

66. Levinson, N. M.; Boxer, S. G., Structural and spectroscopic analysis of the kinase inhibitor bosutinib and an isomer of bosutinib binding to the abl tyrosine kinase domain. *PLoS One*. **2012**, *7*, e29828.

67. Wilson, J. N.; Liu, W.; Brown, A. S.; Landgraf, R., Binding-induced, turn-on fluorescence of the EGFR/ERBB kinase inhibitor, lapatinib. *Org. Biomol. Chem.* **2015**, *13*, 5006-5011.

68. Trummer, B. J.; Iyer, V.; Balu-Iyer, S. V.; O'Connor, R.; Straubinger, R. M., Physicochemical properties of epidermal growth factor receptor inhibitors and development of a nanoliposomal formulation of gefitinib. *J. Pharm. Sci*. **2012**, *101*, 2763-2776.

69. Wissner, A.; Berger, D. M.; Boschelli, D. H.; Floyd, M. B.; Greenberger, L. M.; Gruber, B. C.; Johnson, B. D.; Mamuya, N.; Nilakantan, R.; Reich, M. F.; Shen, R.; Tsou, H.; Upeslacis, E.; Wang, Y. F.; Wu, B.; Ye, F.; Zhang, N., 4-Anilino-6,7-dialkoxyquinoline-3-carbonitrile inhibitors of epidermal growth factor receptor kinase and their bioisosteric relationship to the 4-anilino-6,7-dialkoxyquinazoline Inhibitors. *J. Med. Chem*. **2000**, *43*, 3244-3256.

70. Wissner, A.; Mansour, T. S., The Development of HKI-272 and related compounds for the treatment of cancer. *Arch. Pharm. Chem. Life, Sci*. **2008**, *341*, 465-477.

71. Bridges, A. J., Chemical inhibitors of protein kinases. *Chem. Rev*. **2001**, *101*, 2541-2571.

72. Pannala, M.; Kher, S.; Wilson, N.; Gaudettete, J.; Sicar, I.; Zhang, S. H.; Bakhirev, A.; Yang, G.; Yuen, P.; Gorscan, F.; Sakurai, N.; Barbosa, M.; Cheng, J. F., Synthesis and structure-activity relationship of a series of 4-(2-aryl-cyclopropylamino)-quinoline-3-carbonitrile derivatives as EGFR inhibitors. *Bioorg. Med. Chem. Lett*. **2007**, *17*, 5978-5982.

73. Zhao, C.; An, J.; Zhou, L.; Fei, Q.; Wang, F.; Tan, J.; Shi, B.; Wang, R.; Guo, Z.; Zhu, W., Transforming the recognition site of 4-hydroxaniline grafted onto a BODIPY core switches the selective detection of peroxynitrite to hypochlorous acid. *Chem. Commun*. **2016**, *52*, 2075-2078.

74. Zhang, Y-M.; Cockerill, S.; Guntrip, S. B.; Rusnak, D.; Smith, K.; Vanderwall, D.; Wood, E.; Lachey, K., Synthesis and SAR of potent EGFR/erbB2 dual inhibitors. *Bioorg. Med. Chem. Lett*. **2004**, *14*, 111-114.

75. Knight, L. A.; Di Nicolatonio, F.; Whitehouse, P.; Mercer, S.; Sharma, S.; Glaysher, S.; Johnson, P.; Cree, I. A., The in vitro effect of gefitinib ('Iressa') alone and in combination with cytotoxic chemotherapy on human solid tumours. *BMC Cancer*. **2004**, *4*, 83-90.

76. Jain, A.; Tindell, C. A.; Laux, I.; Hunter, J. B.; Curran, J.; Galkin, A.; Afar, D. E.; Aronson, N.; Shak, S. Natale, R. B.; Agus, D. B., Epithelial membrane protein-1 is a biomarker of gefitinib resistance. *Proc. Nat. Acad. Sci. USA*. **2005**, *102*, 11858-11863.

77. Piechocki, M. P.; Yoo, G. H.; Dibbley, S. K.; Lonardo, F., Breast cancer expressing the activated HER2/neu is sensitive to gefinib in vitro and in vivo and acquires resistance through a novel point mutation in the HER2/neu. *Cancer. Res*. **2007**, *67*, 6825-6843.

78. Hendriks, B. S.; Opresko, L. K.; Wiley, H. S.; Lauffenburger, D. J., Quantitative analysis of HER2-mediated effects on HER2 and EGFR endocytosis: distribution of homo- and hetero-dimers depends on relative HER2 levels. *Biol. Chem.* **2003**, *278*, 23343-23351.

79. Hirata, A.; Hosoi, F.; Miyagawa, M.; Ueda, S.; Naito, S.; Fujii, T.; Kuwano, M.; Ono, M., HER2 overexpression increases sensitivity to gefitinib, an epidermal growth factor receptor tyrosine kinase inhibitor, through inhibition of HER2/HER3 heterodimer formation in lung cancer cells. *Cancer. Res*. **2005**, *65*, 4253-4260.

80. Paez, J. G.; Jänne, P. A.; Lee, J. C.; Tracy, S.; Greulich, H.; Gabriel, S.; Herman, P.; Kaye, F. J.; Lindeman, N.; Boggon, T. J.; Naoki, K.; Sakai, H.; Fujii, Y.; Eck, M. J.; Sellers, W. R.; Johnson, B. E.; Meyerson, M., EGFR mutations in lung cancer: correlation with clinical response to gefitinib therapy. *Science*. **2004**, *304*, 1497-1500.

81. Björkelund, H.; Gedda, L.; Barta, P. Malmqvist, M.; Andersson, K., Gefitinib induces epidermal growth factor receptor dimers which alters the interaction characteristic with ^{125}I-EGF. *PLoS One*. **2011**, *6*, e24793.

82. Björkelund, H.; Gedda, L.; Barta, P. Malmqvist, M.; Andersson, K., Resolving the EGF-EGFR interaction characteristics through a multiple-temperature, multiple-inhibitor, real-time interaction analysis approach. *Mol. Clin. Oncol*. **2013**, *1*, 343-352.

83. Citri, A.; Alroy, I.; Lavi, S.; Rubin, C.; Xu, W.; Grammatikakis, N.; Patterson, C.; Neckers, L.; Fry, D. W.; Yarden, Y. Drug-induced ubiquitylation and degradation of ErbB receptor tyrosine kinases: implications for cancer therapy. *EMBO. J.* **2002**, *21*, 2407-2417.

84. Sánchez-Martin, M.; Pandiella, A., Differential action of small molecule HER kinase inhibitors on receptor heterodimerization: Therapeutic implications. *Int. J. Cancer*. **2012**, *131*, 244-252.

85. Citri, A.; Gen, J.; Mosesson, Y.; Vereb, G.; Szollosi, Z.; Yarden, Y., Hsp90 restrains ErbB-2/HER2 signalling by limiting heterodimer formation. *EMBO. Rep*. **2004**, *5*, 1165-1170.

86. Sigismund, S.; Confalonieri, S.; Ciliberto, A.; Polo, S.; Scita, G.; Di Fiore, P. P., Endocytosis and signaling: Cell logistics shape the eukaryotic cell plan. *Physiol Rev*. **2012**, *92*, 273-366.